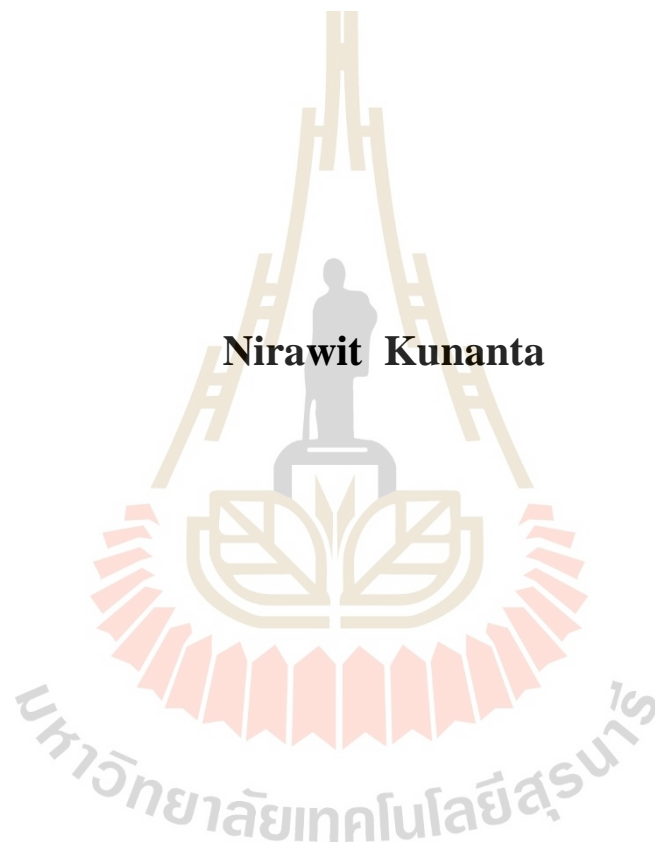


**PERFORMANCE OF REVERBERANT OPTICAL
COHERENCE ELASTOGRAPHY FOR SHEAR
WAVE SPEED MEASUREMENT**



Nirawit Kunanta

**A Thesis Submitted in Partial Fulfilment of the Requirement for the
Degree of Master of Science in Applied Physics**

Suranaree University of Technology

Academic Year 2019

ประสิทธิภาพของรีเวอร์เบอเรนท้อพติคอลโคอีเรนซ์อีลาสโตกราฟี
ในการวัดความเร็วคลื่นเฉือน

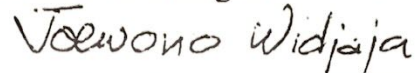


วิทยานิพนธ์นี้เป็นส่วนหนึ่งของการศึกษาตามหลักสูตรปริญญาวิทยาศาสตรมหาบัณฑิต
สาขาวิชาฟิสิกส์ประยุกต์
มหาวิทยาลัยเทคโนโลยีสุรนารี
ปีการศึกษา 2562

PERFORMANCE OF REVERBERANT OPTICAL COHERENCE ELASTOGRAPHY FOR SHEAR WAVE SPEED MEASUREMENT

Suranaree University of Technology has approved this thesis submitted in partial fulfillment of the requirements for a Master's Degree.

Thesis Examining Committee



(Prof. Dr. Joewono Widjaja)

Chairperson



(Assoc. Prof. Dr. Panomsak Meemon)

Member (Thesis Advisor)



(Dr. Wiwat Nuansing)

Member



(Dr. Ittipon Fongkaew)

Member



(Dr. Narong Chanlek)

Member



(Prof. Dr. Santi Maensiri)



(Assoc. Prof. Dr. Chatchai Jothityangkoon)

Vice Rector for Academic Affairs
and Quality Assurance

Dean of Institute of Science

นิพนธ์ ภูนันตา : ประสิทธิภาพของรีเวอร์เบอแรนท์ออฟติคัลโคฮีเรนซ์อีลาสโตกราฟี
ในการวัดความเร็วคลื่นเฉือน (PERFORMANCE OF REVERBERANT OPTICAL
COHERENCE ELASTOGRAPHY FOR SHEAR WAVE SPEED MEASUREMENT).
อาจารย์ที่ปรึกษา : รองศาสตราจารย์ ดร.พนมศักดิ์ มีมนต์, 102 หน้า.

ความเร็วของคลื่นเฉือน/ สนามคลื่นเฉือนสะท้อน/ เทคนิคออฟติคัลโคฮีเรนซ์อีลาสโตกราฟี/
แผนภาพความยืดหยุ่น

ความยืดหยุ่นของตัวอย่างทางชีวภาพเป็นตัวแปรในการทำความเข้าใจคุณสมบัติของ
ตัวอย่าง ซึ่งมีบทบาทสำคัญในการวินิจฉัยและรักษาทางการแพทย์ เทคนิคออฟติคัลโคฮีเรนซ์
อีลาสโตกราฟีได้ถูกพัฒนาขึ้นมาเพื่อที่จะสร้างแผนภาพความยืดหยุ่นของตัวอย่าง หนึ่งในวิธีที่
เป็นที่นิยม คือการติดตามการเคลื่อนที่ของคลื่นเฉือนบนตัวอย่างในขณะที่ให้การกระตุ้นกับตัวอย่าง
ไปพร้อมกัน โดยหลักการของเทคนิคสนามคลื่นเฉือนสะท้อนได้ถูกนำมาประยุกต์ใช้กับเทคนิค
ออฟติคัลโคฮีเรนซ์อีลาสโตกราฟีที่ยังไม่แน่นอน เรียกว่า รีเวอร์เบอแรนท์ออฟติคัลโคฮีเรนซ์อีลาส
โตกราฟี ในงานวิจัยนี้ได้ทดลองเพื่อดูประสิทธิภาพของเทคนิครีเวอร์เบอแรนท์ออฟติคัลโคฮี
เรนซ์อีลาสโตกราฟีนี้ในการแยกความแตกต่างตัวอย่างเจลลาตินที่มีความเข้มข้นต่างกันเล็กน้อย
โดยพบว่า เทคนิคนี้สามารถแยกความแตกต่างของความเร็วเฉือนที่เคลื่อนที่อยู่บนตัวอย่างเจลลาติน
ที่มีความเข้มข้นร้อยละ 3 และ ร้อยละ 4 ได้ ด้วยความเร็ว 1.3 ± 0.1 เมตรต่อวินาที และ 1.5 ± 0.2
เมตรต่อวินาที ตามลำดับ และมีค่าความคลาดเคลื่อนอยู่ที่น้อยกว่าร้อยละ 13 เมื่อเปรียบเทียบกับผล
จากการวัดด้วยเครื่องมือมาตรฐาน และค่าความละเอียดของความยืดหยุ่นของเทคนิครีเวอร์เบอ
แรนท์ออฟติคัลโคฮีเรนซ์อีลาสโตกราฟีนี้ ที่วัดจากรอยต่อของตัวอย่างเจลลาตินที่มีความเข้มข้น
ร้อยละ 3 และ ร้อยละ 4 วัดได้อยู่ที่ 0.3 มิลลิเมตร

สาขาวิชาฟิสิกส์
ปีการศึกษา 2562

ลายมือชื่อนักศึกษา ชวรัตน์ ภูนันตา
ลายมือชื่ออาจารย์ที่ปรึกษา พนมศักดิ์ มีมนต์

NIRAWIT KUNANTA : PERFORMANCE OF REVERBERANT
OPTICAL COHERENCE ELASTOGRAPHY FOR SHEAR WAVE SPEED
MEASUREMENT. THESIS ADVISOR : ASSOC. PROF. PANOMSAK
MEEMON, Ph.D. 102 PP.

SHEAR WAVE SPEED/ REVERBERANT SHEAR WAVE FIELD/ OPTICAL
COHERENCE ELASTOGRAPHY/ ELASTICITY MAPPING


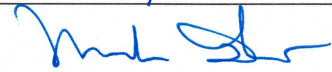
Elasticity of biological tissues is a variable for understanding their properties, which play an important role in medical diagnosis and treatments. Optical Coherence Elastography (OCE) has been intensively developed to map the elastic contrast of various biological tissue. One of the popular methods is tracking shear wave propagation while applied the vibrational force to the surface of the sample. Concept of reverberant shear wave field has been applied to OCE recently, called Rev3D-OCE. In this study, the Rev3D-OCE experimentally was performed to differentiate the slightly different concentrations of gelatin phantom. Rev3D-OCE can differentiate the different shear wave speeds (SWS) that propagated on different 3 wt% and 4 wt% gelatin phantoms with average SWS as $v_{s,3\%} = 1.3 \pm 0.1$ m/s and $v_{s,4\%} = 1.5 \pm 0.2$ m/s, respectively with < 13% of error as compared to standard measurement results. The spatial elastic resolution of Rev3D-OCE determined from edge response at the interface of 3 wt% and 4 wt% phantoms was measured to be 0.3 millimeters.

School of Physics

Student's Signature

Academic Year 2019

Advisor's Signature

ACKNOWLEDGEMENTS

I would like to express my sincere appreciation to my project advisor, Asst. Prof. Panonsak Meemon for the useful recommendation, also about his experiences.

I would like to thank Prof. Dr. Joewono Widjaja, Dr. Wiwat Nuansing, Dr. Ittipon Fongkaew, and Dr. Narong Chanlek for sitting on the thesis committee and giving me various excellent advice that inspired me for deeper study of science in the past three academic years.

I would like to show my gratitude to Prof. Jannick P. Rolland, Prof. Kevin J. Parker, and their research group members, especially Fernando Zvietcovich who help me with doing research and impressive life experiences at the University of Rochester, New York, United States. I am also grateful to all members of Light Applications in Science and Engineering Research group. They help with life problem counseling, photography, including food.

I will not be at this point without support from the scholarship from the Development and Promotion of Science and Technology Talents Project (DPST), Institute of Optics, Hajim School of Engineering and Applied Sciences, University of Rochester, and Suranaree University of Technology (SUT).

Finally, I would like to thank my mom and my brothers who always support me.

Nirawit Kunanta

CONTENTS

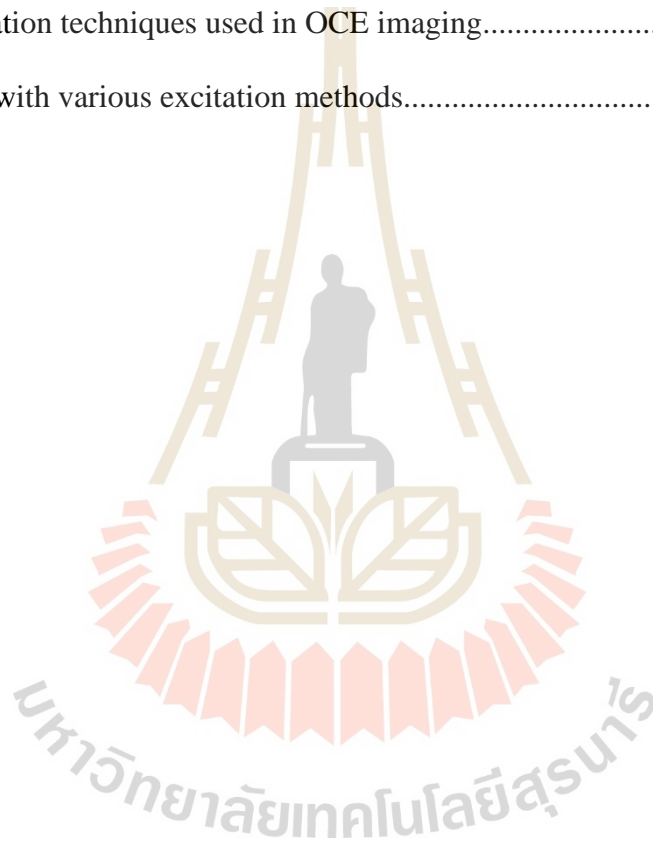
	Page
ABSTRACT IN THAI.....	I
ABSTRACT IN ENGLISH.....	II
ACKNOWLEDGEMENTS.....	III
CONTENTS.....	IV
LIST OF TABLES.....	VI
LIST OF FIGURES.....	VII
LIST OF ABBREVIATIONS.....	XIV
CHAPTER	
I INTRODUCTION.....	1
1.1 Background	1
1.2 Significance of the study.....	4
1.3 Research objectives	5
1.4 Scope of study.....	5
II BACKGROUND AND THEORIES.....	6
2.1 History of elastography.....	6
2.1.1 Manual palpation.....	6
2.1.2 Elastography.....	7
2.2 Optical Coherence Tomography (OCT).....	11
2.2.1 Principle of tomography	11

CONTENTS (Continued)

	Page
2.2.2 Low-coherence interferometry.....	12
2.2.3 Time domain OCT (TD-OCT)	13
2.2.4 Frequency domain OCT (FD-OCT)	15
2.2.5 Signal-to-noise ratio (SNR)	25
2.3 Optical Coherence Elastography (OCE).....	27
2.3.1 Concept of elastic measurement.....	27
2.3.2 Excitation and detection schemes.....	46
2.4 Gelatin phantoms.....	48
2.5 Standard mechanical testing.....	49
III RESEARCH METHODOLOGY.....	51
3.1 Gelatin phantom preparation.....	51
3.2 Experimental setup.....	54
3.4 Data analysis.....	62
IV RESULTS AND DISCUSSIONS.....	69
4.1 Phantom preparation issues.....	69
4.2 Image processing and filtering.....	72
4.3 Window size variations.....	78
4.4 Discussions.....	86
V SUMMARY.....	88
REFERENCES.....	92
CURRICULUM VITAE.....	102

LIST OF TABLES

Table	Page
2.1	Timeline of development of OCE imaging techniques.....10
2.2	Excitation techniques used in OCE imaging.....11
2.3	OCE with various excitation methods.....47



LIST OF FIGURES

Figure	Page
2.1	Manual palpation demonstration.....6
2.2	(a) Elastogram of the layer polyester foam with different porosity using ultrasound imaging (UI) technique. (b) Elastograms of patient with breast cancer by using magnetic resonance elastography (MRE) technique.....8
2.3	The position of OCE compared with other non-destructive imaging techniques in terms of spatial resolution and field of view (FOV).....9
2.4	Images with tomography (S_1 and S_2) and without tomography (P) principle...10
2.5	Basic Michelson interferometer.....14
2.6	Time domain OCT (TD-OCT) setup.....15
2.7	Schematic of Fourier domain OCT (FD-OCT).....16
2.8	(a) Multilayer sample at different OPL of z_1 , z_2 , z_3 . (b) Reflectivity of a sample as a function of OPL. (c) Shape of spectrum from the light source. (d) Interference signal acquired at detector of OCT imaging. (e) Depth profile from interference signal. (f) B-mode or cross-section image from sorting consecutive depth profile along x-axis.....21
2.9	(a) Acquisition process to obtain the 3D depth profile by sorting PSF over x-axis and repeat the process for all y-axis. (b) a 3D volume of multilayers sample.....22

LIST OF FIGURES (Continued)

Figure	Page
2.10	The relative absorption of biological component shows less absorption of water in NIR range (drop of blue curve).....23
2.11	Example of spectra of SLD light source (S840-B-I-20, Superlum, Ireland)....24
2.12	Type of waves.....28
2.13	P-waves propagation.....29
2.14	S-waves propagation.....29
2.15	L-waves propagation30
2.16	R-waves propagation.....31
2.17	Schematic and axis definitions for the reverberant shear wave field concept....35
2.18	The autocorrelation results depend on the direction of the displacement Δr with the axis of detection. The correlation function with respect to the x -direction is shown in thin line (equation 2.59), and thick blue line is the correlation in z -direction (equation 2.66). These spatial sinc functions will be used for estimating local wavenumber k45
2.19	(a) The standard compression testing (MTS, Eden Prairie, Minnesota, United States). (b) Compression area of the compression test, the top plate moves downward and compressed the sample, sensor will record loading information together with the distance that the top plate moved.....50
3.1	(a) Weight gelatin powder and coffee cream for specific concentrations. (b) Gelatin solution with a magnetic stirrer. (c) Air bubble in the liquid gelatin solution (in the middle).....52

LIST OF FIGURES (Continued)

Figure	Page
3.2	(a) Gelatin phantom with coffee cream, and (b) without coffee cream. (c) Gelatin solution on the silicone mold covered with plastic wrap. (d) Cylindrical shapes of gelatin phantom for standard measurements.....53
3.3	The process of gelatin preparation of homogeneous and left-right configurations.....54
3.4	Schematic diagram of an experimental setup of the PhS-OCT, external synchronization (trigger), and external excitation using a 3D printed ring actuator attached to single piezoelectric actuator.....55
3.5	Ring actuator model, (a) side view, (b) bottom view (c) 3D view with piezoelectric actuator. (d) Ring actuator was used in the experiment.....57
3.6	(a) Time axis of all devices to synchronization. (b) Excitation scheme and scanning mirror synchronization by a single trigger.....59
3.7	The zig-zag scanning pattern was operated on OCE imaging to reduce the acquisition time.....60
3.8	Graphical explanation of raw data in the detection scheme. Single detection creates 1 M-mode ($1 \times 2,000$ pixels), continuing to collect until 100 M-mode, then become one spatial position (one .tif file). Repeat the process to gather a hundred spatial positions (one MB-mode), and do the same process for another axis. Total raw data is called “the pool”, which is capable to retrieve any plane and time frame.....61

LIST OF FIGURES (Continued)

Figure	Page
3.9	Flowchart of data analysis to obtain the shear wave speed (SWS) map, all processes were done in MATLAB TM software63
3.10	The flowchart shows the image processing. (a) Spectra frame (2048 pixel by 100 M-mode. (b) Example of an interference signal from a line spectrum in (a). (c) M-mode image from all lines in (a). (d) MB-mode from 1D lateral scanning. (e) B-mode image obtained by resliced MB-mode. (f) Scanning another lateral axis to obtain the 3D volume. (g) The <i>en-face</i> (top view) can be obtained from resliced any depth position.....66
3.11	Analysis process for the local shear wave speed (SWS) map. (a) Example of <i>En-face</i> (Top view) image of the gelatin phantom. (b) the phase shift data collected from Loupas's algorithm and divided into small windows for the 2D-autocorrelation following the concept of reverberant shear wave field. (c) Autocorrelation result and radial averaging (red dash line) for curve fitting. (d) The radial average the autocorrelation (black dot) and the wavenumber was obtained by determining k from curve fitting (blue line). (e) Local shear wave speed (SWS) map is determined from the phase velocity relation (equation 2.67)68
4.1	(a) The silicon mold with gelatin solutions and plastic wrap. (b) Damaged gelatin phantom when trying to remove from the mold.....70
4.2	Small holes were found on the bottom surface of the gelatin phantom when taken out from the silicone mold with lubricant oil.....71

LIST OF FIGURES (Continued)

Figure	Page
4.3	Gelatin phantom of 3 wt% and 4 wt% with plastic wrap inside at the bottom of the Petri dish for easy removal (top surface was used for experiment).....71
4.4	Photograph of the gelatin phantom of (a) homogeneous 4 wt% concentration, (b) homogeneous 3 wt% concentration, and (c) the left-right configuration...72
4.5	(a), (c) B-mode images of 3 wt% and 4 wt% gelatin phantoms, respectively. Bright-line describes the cross-section structure of the air-gelatin interface. (b), (d) <i>En-face</i> images of 3 wt% and 4 wt% gelatin phantoms, respectively. Dark regions represent the instability of the surface's smoothness, darker regions are caused by the end of the ring actuator.....73
4.6	The local phase shift information using Loupas's algorithm of (a) B-mode and (b) <i>en-face</i> images of 3 wt% gelatin phantom.....74
4.7	The process of temporal filtering of the phase shift data. (a) The phase data without temporal filtering. (b) Fourier Transform of (a). (c) Comparison of the filtered data (orange) and unfiltered data (blue).....75
4.8	(a) <i>En-face</i> (top view) image of the phase shift data before spatial filtering. (b) Two-dimensional Fourier Transformation of (a). (c) Band-pass filter (750-1250 Hz bandwidth). (d) cross-section of (b) (orange) and band-pass filter (blue). (e) <i>En-face</i> image of the phase shift data after spatial filtering....76
4.9	<i>En-face</i> images at different time frames show the motion of the shear wave propagating on 3 wt% gelatin phantom.....77

LIST OF FIGURES (Continued)

Figure	Page
4.10	<p><i>En-face</i> images show the different wavelengths of shear wave propagation of (a) 3 wt% and (b) 4 wt% gelatin phantoms, in which the wavelength on the 4 wt% phantom is larger than on the 3 wt% phantom.....78</p>
4.11	<p>(a) The reverberant shear wave field on 3 wt% gelatin phantom with the illustration of different correlation window sizes. (b) The example of the radial average of the autocorrelation curves of 3 wt% gelatin phantom with 30 × 30 pixels of window size.....79</p>
4.12	<p>The shear wave speed (SWS) map of the 3 wt% gelatin phantom with the 1 kHz of excitation, by varying the correlation window sizes of (a) 10 × 10 pixels, (b) 20 × 20 pixels, (c) 30 × 30 pixels, (d) 40 × 40 pixels, (e) 50 × 50 pixels, (f) 60 × 60 pixels, (g) 70 × 70 pixels, (h) 80 × 80 pixels, and (i) 90 × 90 pixels. There are look almost identical for larger window (from (d) to (i)), but less data in curve fitting process causes discrete value of SWS in (a) and (b) as display in dark blue color.....80</p>
4.13	<p>The shear wave speed (SWS) map of 4 wt% gelatin phantom with 1 kHz of excitation, by varying the correlation window sizes of (a) 10 × 10 pixels, (b) 20 × 20 pixels, (c) 30 × 30 pixels, (d) 40 × 40 pixels, (e) 50 × 50 pixels, (f) 60 × 60 pixels, (g) 70 × 70 pixels, (h) 80 × 80 pixels, and (i) 90 × 90 pixels.....81</p>

LIST OF FIGURES (Continued)

Figure	Page
4.14	The average shear wave speed (SWS) of all given correlation windows of 3 wt% (blue) and 4 wt% gelatin phantoms.....82
4.15	(a) B-mode and (b) <i>en-face</i> images of the left-right configuration of gelatin phantom. (c) <i>En-face</i> image of phase shift of the left-right configuration shows the different wavelengths between 4 wt% (left) and 3 wt% (right). (d) The shear wave speed (SWS) map of the L4R3 gelatin phantom shows the shear wave propagates faster on the 4 wt% gelatin phantom.....83
4.16	The average speed profile across the gelatin interface was computed from the SWS data in the red frame of figure 4.15(d).....85
4.17	The experimental shear wave speed (SWS) results: Homogeneous (blue), left-right (orange), and the results from standard measurement (yellow) of the 3 wt% and 4 wt% gelatin phantoms.....86

LIST OF ABBREVIATIONS

AFM	Atomic Force Microscope
ARF	Acoustic Radiation Force
CBM	Confocal Brillouin microscopy
CCD	Charge-coupled device
CMOS	Complementary Metal-Oxide-Silicon
D	diameter of laser beam
dB	Decibel
DBD	Dual band detector
E	Young's modulus
f	Focal length of the objective lens
FT	Fourier Transformation
FFT	Fast Fourier Transformation
FD-OCT	Fourier or Frequency-Domain Optical Coherence Tomography
FWHM	Full Width at Half Maximum
FOV	Field of View
G	Shear modulus
HI	Holographic imaging
k	Wave number
LCI	Low coherence interferometry
L-waves	Love waves

LIST OF ABBREVIATIONS (Continued)

MNPs	Magnetic Nanoparticles
MRE	Magnetic Resonance Elastography
MRI	Magnetic Resonance Imaging
NIR	Near infrared
OCE	Optical Coherence Elastography
OCT	Optical Coherence Tomography
OPD	Optical path difference
P_{signal}	Power of signal
P_{noise}	Power of noise
P-waves	Primary waves
PSF	Point Spread Function
ROI	Region of Interest
R-waves	Rayleigh waves
SAW	Surface Acoustic Wave
sig	Sigmoid function
SLD	Superluminescent diodes
SNR	Signal-to-Noise ratio
S-waves	Secondary waves
t	Time variable
TD-OCT	Time-Domain Optical Coherence Tomography
UE	Ultrasound Elastography
UI	Ultrasound Imaging

LIST OF ABBREVIATIONS (Continued)

λ	wavelength
λ (Bold lambda)	Lamé parameter
ρ	Density
δ	Data transfer time
\bar{u}	Displacement vector
\bar{u}_s	Shear wave displacement vector
\bar{u}_p	Pressure wave displacement vector
v_s	Shear wave speed
v_p	Pressure wave speed
v_R	Rayleigh wave speed
ν	Poisson's ratio
ω	Angular frequency

CHAPTER I

INTRODUCTION

1.1 Background

Observations and characterizations of the mechanical properties of biological tissues can tell us about its disease's existence, and for understanding its healthy and pathophysiology, which can aid medical diagnosis and treatments. The elastic property is one of the mechanical properties that can be acquired and used as a diagnostic parameter of healthy biological tissues.

Medical imaging is one of the advancements in technology, which is the technique and process to create the visual representation of tissue for clinical analysis and treatments. Nowadays, advancements in optical technologies have an important role in medical imaging and diagnostics. Optical imaging provides higher resolution and accuracy as compared with X-ray imaging, magnetic resonance imaging (MRI), and Ultrasound imaging (UI). Optical techniques can also explore and investigate some new regions that are not possible with the other methods. Optical technologies allow for the analysis and diagnosis of the existence of diseases for a better understanding of the mechanics of tissue and human bodies (Rogowska et al., 2004). The medical imaging based on mapping the elastic information of the tissue called "elastography" was developed for ultrasonic imaging in late 1980s and had been proven to be useful technique for cancer diagnostic. MRI also applied the elastography for *in vivo* cancer

detection in the early 2000s. However, the limitations of these techniques cause the elastography still remain in organ-size diagnostic (Wang and Larin, 2015). Optical coherence tomography (OCT) is one kind of optical imaging technique that provides a cross-section image of the living tissue (Huang et al., 1991). OCT is typically built on Michelson interferometer, which works in a similar manner to the ultrasound but uses light instead of the sound wave. Therefore, it can provide a higher resolution than MRI and UI (Schmitt, 1999; Wang and Larin, 2015).

Optical coherence elastography (OCE) is an extension of OCT, which provides information about the elastic property of the sample by using internal or external excitation to create tissue displacement. OCE has the potential for diagnostic and monitoring diseases in the medical field. For example, OCE was used to measure the elastic property of facial skin, which was used as an age factor to indicate healthy facial skin (Cartigliani et al., 2014), which would help the doctor to improve skin diagnostics.

There are main three groups to obtain the elastic information from OCE imaging (Wang and Larin, 2015). Firstly, measuring strain, by applying known input stress and measuring the strain of the tissue. Secondly, measuring the resonance frequency, by applying loading function with driving frequency corresponding to the resonance frequency of the tissue, which causes the maximum tissue displacement and the strain was measured. The last group is tracking wave propagation, the elastic properties can be obtained by measuring the speed of wave propagation caused by the external excitation, which we focused to use this excitation technique. Waves propagation occurred when some position of the medium was disturbed by external stimulation and transmitted to other parts of that medium (Graff, 2012). Typically, the wave travels faster in stiffer/healthy tissue, compared to normal/healthy tissue. The type of waves

that we focused on in our study is shear waves (S-waves). S-wave occurred when the excitation was applied in perpendicular direction to the surface of the tissue, which caused the tissue displacement when the waves passed. The relationship of tissue displacement and phase is analyzed in the process of OCE imaging and related to the elastic information (Crecea et al., 2009; Kennedy et al., 2009; Manapuram et al., 2009; Mulligan et al., 2016).

In 2017, Parker et al. introduces an alternative method for shear wave speed evaluation, called “reverberant shear wave field” (K. J. Parker et al., 2017). According to complexity in real tissue, the multiple reflections of waves from the existence of internal structures occurred when the waves propagate in the tissue, which cannot avoid (Kevin J. Parker and Maye, 1984; K. J. Parker et al., 2017). Thus, the evaluation of the shear wave speed by using the time of flight will be disturbed (Hoyt et al., 2008; Itoh et al., 2006; Li et al., 2012). For shear wave speed measurements, the multiple sources of excitation were used to mimic the multiple reflections. The randomness of wave propagations will be calculated through the analysis process, then the local shear wave speed map is obtained, which is related to the elastic information of the tissue (Ahmad et al., 2014; Doyley and Parker, 2014; Hoyt et al., 2008; Jiasong et al., 2013; Li et al., 2012; Li et al., 2011; Wang and Larin, 2015; Wells and Liang, 2011; Worden, 2001; Zvietcovich, Yao, Chu, et al., 2016).

In our laboratory, we have OCT that is ready to be modified to OCE and used for tissue characterization by using the piezoelectric actuator to generate the vibrational shear wave on the surface of the sample. To show the performance of the reverberant OCE imaging, we have developed techniques to generate the elastogram that determines the speed of the wave propagations on the gelatin phantom, i.e. concentration-based

material, mostly used in elastography experiments (Karimi and Navidbakhsh, 2014; K. J. Parker et al., 2010; Wang and Larin, 2015), which is typically in the range 1-10 meters per second (m/s) (Zvietcovich, Rolland, Yao, et al., 2017). The experiments were controlled and monitored using LabView software (National Instruments, Austin, TX, United States). Our OCT imaging used the near-infrared light source at 1,318 nanometers (nm) of center wavelength and 125 nm of spectral bandwidth, the penetration depth is approximately about 2 millimeters (Itoh et al.), lateral and axial resolutions are 20 and 10 micrometers (μm), respectively. Field of view (FOV) is 8 mm \times 8 mm. All data were analyzed by our algorithms to evaluate the shear wave speed with MATLABTM software (MathWorks, Massachusetts, United States), then compared results with the standard mechanical testing.

1.2 Significance of the Study

In real skin, there is more complexity than a mimicked phantom in our experiment, which cannot access this information by using the universal method, i.e., standard mechanical testing. There is also the difference of elastic region in the vertical plane or axial elastic contrast. Moreover, tissue deformations can occur in any part of our body. Since the concept of “reverberant shear wave field” was presented by K. J. Parker and his colleagues published in 2017, which can be used to estimate the tissue properties (K. J. Parker et al., 2017). However, the performance of the reverberant OCE to differentiate different elastic contrast in both lateral and axial directions have not yet been explored. In this research, we will apply the reverberant technique to our OCE excitation system for determining the elastic contrast in gelatin phantom, to illustrate

the performance of the reverberant shear wave field concept for determining the shear wave speed, which guided us to the elastic information.

1.3 Research Objectives

- 1) To study the performance of reverberant OCE to differentiate different elastic contrasts.
- 2) To study the effect of parameters for shear wave speed determinations in the analysis process for calibration with the standard measurements.

1.4 Scope of Study

- 1) To develop the reverberant OCE imaging based on the measurement of the shear wave speeds in the range of 1-10 meters per second (m/s) on gelatin phantoms using the piezoelectric actuator.
- 2) Develop software to calculate the shear wave speed from data in the acquisition process of reverberant OCE imaging.
- 3) The reverberant OCE imaging system used a broadband near-infrared laser at 1,318 nm of center wavelength and has spectral width of 125 nm, the penetration depth is approximately about 5 mm, lateral and axial resolutions are 20 and 10 μm , respectively. The field of view (FOV) is $8 \times 8 \text{ mm}^2$.
- 4) Use the 3D printed ring actuator attached to the piezoelectric actuator in the excitation scheme of the reverberant OCE imaging.
- 5) Acquired data by LabView (National Instruments, Austin, TX, United States), process data in MATLABTM (MathWorks, Massachusetts, United States).

CHAPTER II

BACKGROUND AND THEORIES

2.1 History of Elastography

2.1.1 Manual palpation

The classical method to access the skin diagnostic and access the information about the patient's tissue was done by manual palpation as shown in figure 2.1. This method has been considered to be a fundamental diagnostic in ancient Egypt, China, or even in western medicine (Wells and Liang, 2011). Nevertheless, manual palpation provides the information of tissue only in large size structure (low resolution), with several limitations for diagnostic. For instance, the sensitivity of the physical technician or doctor, and their work experience. Thus, manual palpation becomes an unreliable method for the smaller and deeper region in the skin diagnostic.



Figure 2.1 Manual palpation demonstration (Muscolino, 2008).

2.1.2 Elastography

Nowadays, modern technology can gather much more useful information of human for tissue diagnostic. Medical imaging is one of the techniques and processes to produce the visual representation of tissue for clinical analysis and treatments. One of the parameters to determine the health of tissue is the mechanical property of the tissue. For example, scleroderma skin cancers are normally stiffer than surrounding healthy tissue (Itoh et al., 2006). The universal standard method to obtain mechanical property is the compression test, which measures the stress and strain of the sample. However, this technique is tissue destructive and cannot be used *in situ* (Wang and Larin, 2015).

In the late 1980s, the concept of elastography was developed to improve ultrasonic imaging (UI) (Doyley and Parker, 2014) as shown in figure 2.2(a). Elastography is one kind of medical imaging based on the mapping of the mechanical properties of the tissue (Ahmad et al., 2014). The main idea of the elastography is that the tissue will be changed when applied distortions/vibrations, which is an indicator to separate unhealthy tissues from surrounding healthy tissues (Ophir et al., 1991). Ultrasound elastography has been proven to be a useful technique for the diagnostic of breast cancer, thyroid, and liver cancers (Li et al., 2012; K. J. Parker et al., 2010).

Afterward, in 2001, Magnetic resonance imaging (MRI) was used to measure the propagating acoustic waves on the tissue as shown in figure 2.2(b). Also, ultrasound elastography (UE) was developed and applied for *in vivo* cancer detection. At the same time, the atomic force microscopy (AFM) was used for elastography by applying nanoscale indentation, which provides the mechanical properties of a single cell, which means AFM technique has a very small limited FOV. Furthermore, AFM

technique is only suitable for nanoscale and flat surface measurement, compared to MRI and UI techniques have resolutions in centimeters level, which is more suitable for the organ-size FOV.

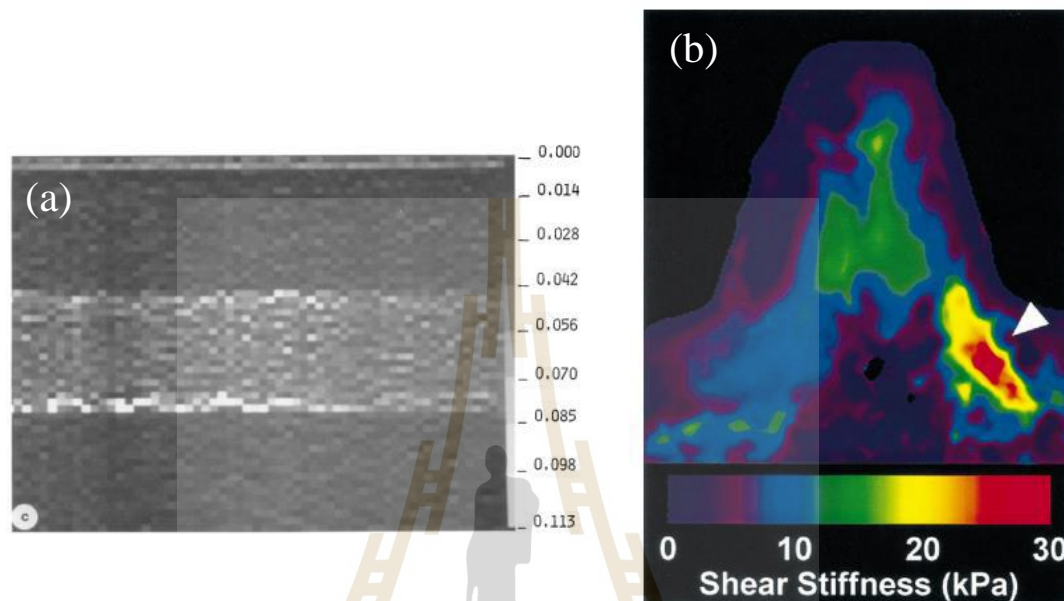


Figure 2.2 (a) Elastogram of the layer polyester foam with different porosity using ultrasound imaging (UI) technique (Ophir et al., 1991). (b) Elastograms of patient with breast cancer by using magnetic resonance elastography (MRE) technique (Manduca et al., 2001).

Although MRI and UI are widely used in many fields, their resolutions are limited in centimeters level, which is only possible for the organ-size. Thus, there is a resolution gap between the cellular level (AFM) and organ level (MRI and UI).

Recently, the resolution gap was filled by the optical imaging technique called “Optical Coherence Elastography” or OCE that was introduced by Schmitt in 1998 (Manapuram et al., 2012). OCE based on optical coherence tomography (OCT), which provided millimeter to micrometer-scale resolution as shown in figure 2.3. In

addition, OCE has a high potential for non-destructive tissue elasticity characterization. OCE has been developed for clinical applications in many fields, e.g., ophthalmology and cardiology.

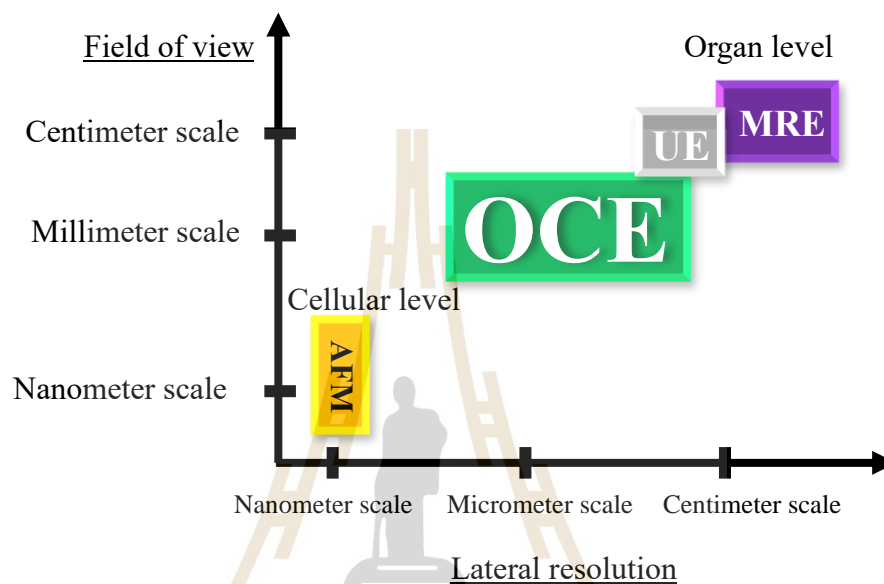


Figure 2.3 The position of OCE compared with other non-destructive imaging techniques in terms of spatial resolution and field of view (FOV).

มหาวิทยาลัยเทคโนโลยีสุรนารี

The timeline of OCE imaging technique is shown in table 2.1 (Crecea et al., 2009; Fercher et al., 2003; Jiasong et al., 2013; Manduca et al., 2001; Ophir et al., 1991; Schmitt, 1999; Wang and Larin, 2015).

Table 2.1 Timeline of development of OCE imaging techniques.

Year	OCE imaging development
1980	Ultrasound elastography was proposed
1991	TD-OCT was presented by D. Huang (1991) Ultrasound elastography
1998	First OCT elastography using the piezoelectric actuator
2001	Magnetic Resonance Elastography (MRE)
2009	OCE using magnetomotive nanoparticle
2013-2014	OCE using air-puff excitation

OCE measures the tissue response when applying the external or internal stimulation. There are several techniques for induced the excitation in OCE imaging as shown in table 2.2, such as the acoustic radiation force (Itoh et al., 2006; Klauser et al., 2014; Song et al., 2015; Zvietcovich et al., 2018), magnetic nanoparticles as the internal transducers (Ahmad et al., 2014; Crecea et al., 2009; Zvietcovich et al., 2018), air-puff indentation for non-contact excitation (Jiasong et al., 2013; Mulligan et al., 2016), and mechanical actuators (Kennedy et al., 2009; Li et al., 2012; Meemon et al., 2016; Schmitt, 1999; F. Zvietcovich et al., 2019; Zvietcovich, Rolland, Yao, et al., 2017).

Table 2.2 Excitation techniques used in OCE imaging.

Excitation techniques	Authors	Contact/ Non-contact	Frequency of excitation
ARF	(Itoh et al., 2006)	Contact	Not found
	(Song et al., 2015)		120 Hz
MNPs	(Crecea et al., 2009)	Non-contact	10 Hz
	(Ahmad et al., 2014)		500 Hz
	(Manduca et al., 2001)		50-1,000 Hz
Laser-induced	(Li et al., 2011)	Non-contact	0.5 Hz
Air-puff	(Jiasong et al., 2013)	Non-contact	125 Hz
Mechanical actuator	(Kennedy et al., 2009)	Contact	820 Hz
	(Li et al., 2012)		20 Hz
	(Zvietcovich, Yao, Rolland, et al., 2016)		400 Hz
	(F. Zvietcovich et al., 2019)		1,000 Hz

2.2 Optical Coherence Tomography (OCT)

2.2.1 Principle of tomography

The term “tomography” means imaging some sections of the sample via penetrating waves (e.g., X-rays, microwave, infrared). Tomography is widely used in various fields. For instance, X-Ray tomography, which operated by moving X-ray source and film with opposite way. Projection of the focal plane will appear sharper on film, but other planes are blurred. If the box was imaged from outside, then the projection image will be like the P-plane in figure 2.4, which is not the real shape like the object inside the box. But the image plane S_1 and S_2 were obtained by using the principle of tomography which consist of real shape are inside the box. Recently, modern tomography involved projection data from many directions to create the

tomographic image from the image reconstruction process. Each plane is called a “virtual slice” sample image, allowing for seeing e inside the sample without cutting.

Tomographic imaging techniques such as X-ray tomography, magnetic resonance imaging (MRI), and ultrasound imaging (UI) have been used for imaging with different properties, resolution, and penetration depth.

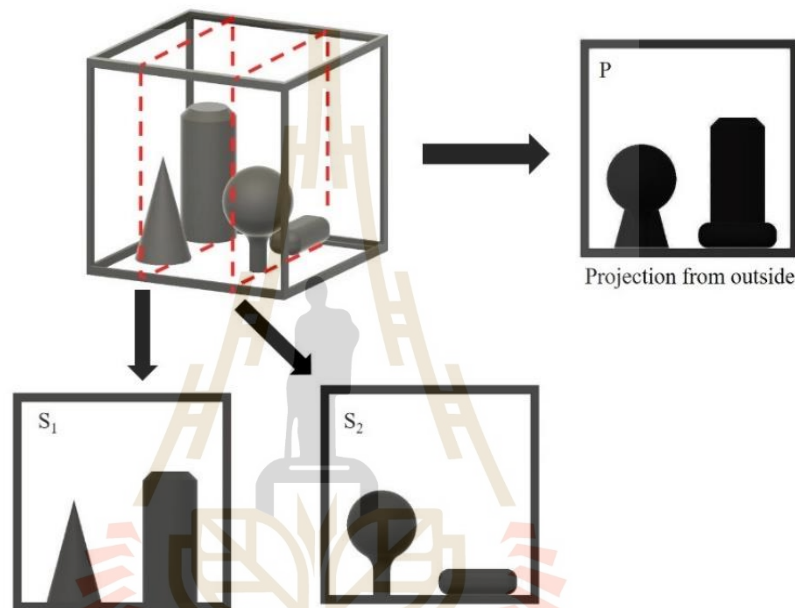


Figure 2.4 Images with tomography (S_1 and S_2) and without tomography (P) principle.

2.2.2 Low-coherence interferometry

The term “coherence” is the property of light (considered as waves) that their frequency and phase difference is constant. However, there is some distance that light waves maintain their coherence property, called “coherence length”, which governed the depth resolution of OCT imaging (Fercher et al., 2003). Some light source that provides several meters of coherence length is the monochromatic laser, i.e., single-mode He-Ne laser ~ 100 meters (m), and some provide some micrometers of coherence

length such as broadband laser (consist of multiple wavelengths). The coherence length l_c can be expressed as follows (Fercher et al., 2003)

$$l_c = \frac{2 \ln 2 \bar{\lambda}^2}{\pi \Delta\lambda}, \quad (2.1)$$

where $\bar{\lambda}$ is center wavelength of the broadband light source, and $\Delta\lambda$ is the spectral bandwidth.

In the two-beam imaging system, the interference pattern will occur only in the range of coherence length. In addition, the coherence length affects the sensitivity of the optics system that the smaller of coherence length, higher sensitivity was obtained in the imaging system (Aumann et al., 2019).

2.2.3 Time domain OCT (TD-OCT)

Optical Coherence Tomography (OCT) has been developed for noninvasive cross-section imaging in the biological tissue (Huang et al., 1991). OCT uses the broadband near-infrared light as a source. Because light travels faster than sound in ultrasound imaging (UI), the calculation of the time delay of the backscattered signal cannot be processed directly. Thus, comparison the signal with reference is used in the measurement, which can be obtained by using an interferometer, such as Michelson interferometer (figure 2.5) (Aumann et al., 2019; Fercher et al., 2003; Schmitt, 1999). The low coherence light source was split into two beams by the beam splitter at the middle, divided light into two arms: sample arm, and the reference arm. The sample arm has the objective lens to focus the beam into the sample, while in the reference arm usually has a mirror. If the reflected light from the reference arm and

backscattered light from the sample arm has nearly the same optical path length (OPL), then the interference pattern will appear on the detector.

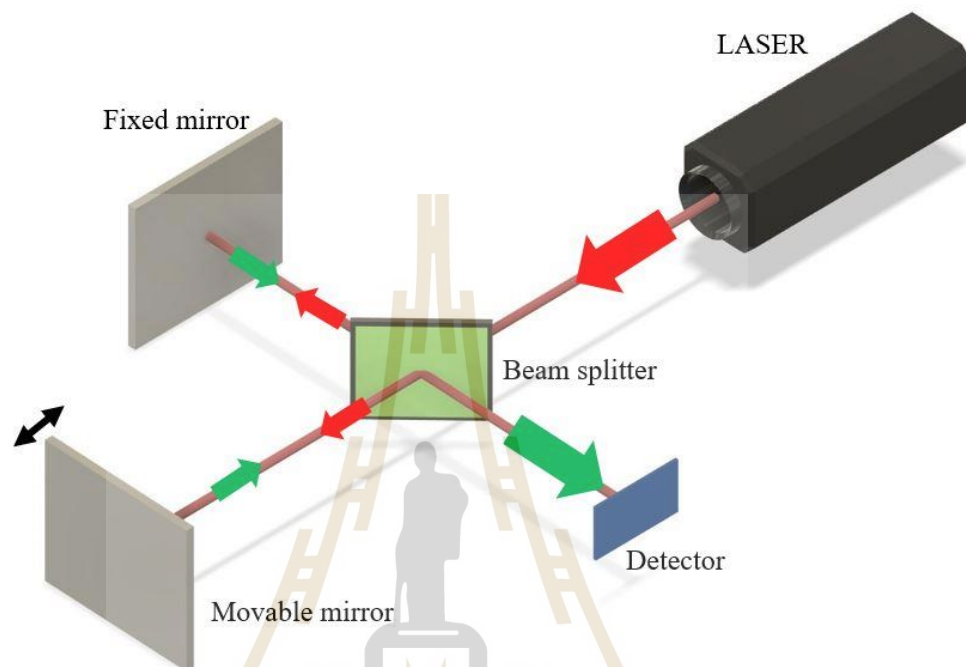


Figure 2.5 Basic Michelson interferometer.

In the time domain OCT (TD-OCT), the setup follows figure 2.6. The interference that occurred at the detector (which is photodiode) comes from the two beams of the reference arm and the sample arm, where the light has nearly the same optical path length. To obtain the deeper region of the sample, the movable mirror in reference arm is used to scan along the beam axis. The light intensity that the photodiode detected is processed and becomes the cross-section image. The acquisition speed of cross-section imaging depends on the speed of the movable mirror.

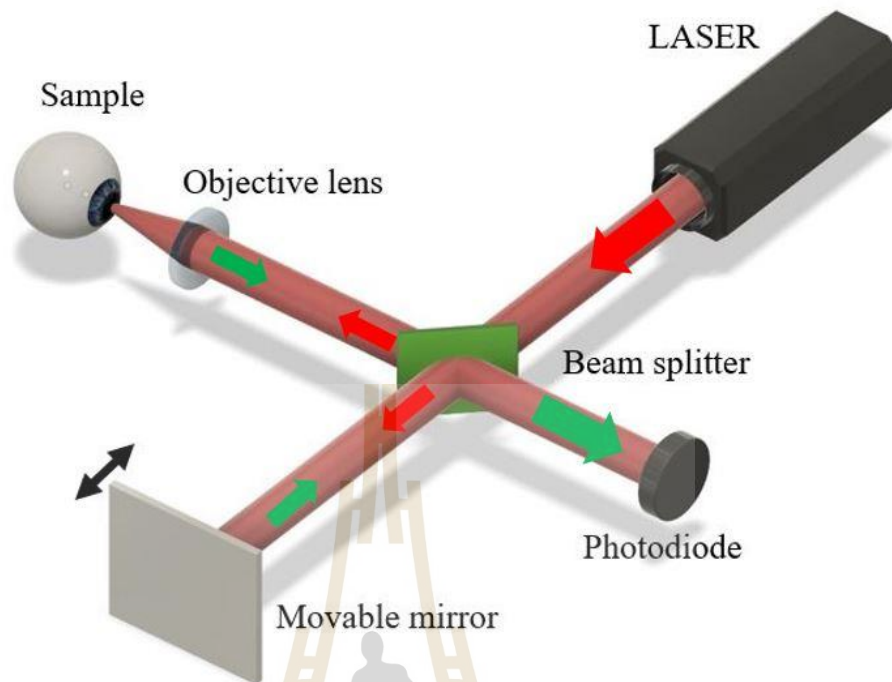


Figure 2.6 Time domain OCT (TD-OCT) setup.

2.2.4 Frequency domain (FD-OCT)

Afterward, a faster imaging technique was introduced called “Frequency-domain OCT (FD-OCT)” or another name “Spectral-domain OCT (SD-OCT)”. The TD-OCT requires two scanning systems, which are scanning the lateral position on the sample arm, and another scanning to obtain a depth profile on the movable mirror, while FD-OCT requires only the lateral scanning. FD-OCT used spectrometer instead of photodiode like TD-OCT. The depth profiles of FD-OCT were received by inverse Fourier transformation of the interference spectrum that acquired from the line sensor of the spectrometer. Moreover, FD-OCT provides the 2D and 3D profile images of the sample by changing the position of lateral scanning in the sample arm (Fercher et al., 2003).

In the fiber-based FD-OCT, light comes out from the superluminescent diode (SLD), which provides multiple wavelengths for low coherence interferometry is split into two beams with 50:50 power ratio by a fiber coupler. The first half goes to the sample arm, and another half goes to the reference arm. In the sample arm, light in fiber is collimated to free-space optics and approach to scanning mirror, which controls the lateral scanning position of the sample. The reflected light redirected to the objective lens and focused on the sample, while light in reference arm goes to the plane mirror in free space, reflected and coupled back through fiber again. The backscattered light in the sample arm is collected by the same objective lens, reflected on the scanning mirrors and coupled back into the fiber. Both lights from the sample arm and reference arm are combined at fiber coupler. The interference pattern occurs and captured by the spectrometer, which consists of a diffraction grating, lens, and line sensor (figure 2.7), where wavelength diffract in a different angle and is captured by individual pixel of the sensor.

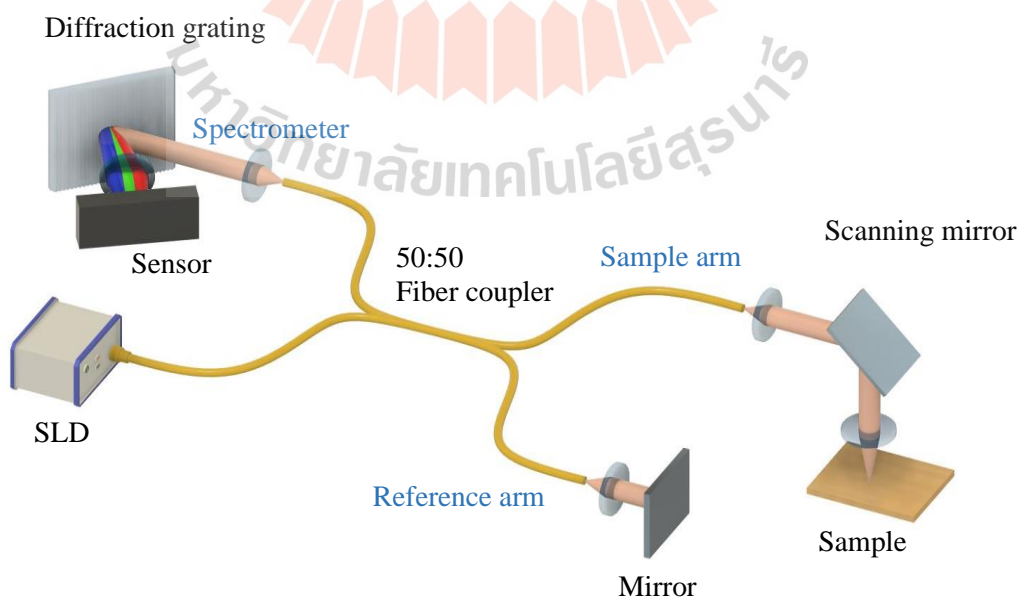


Figure 2.7 Schematic of Fourier domain OCT (FD-OCT).

To perform a cross-section image from the FD-OCT imaging system, the following mathematical expression will be explained step by step.

$$\tilde{I}(k) = |\tilde{E}_R(k) + \tilde{E}_S(k)|^2, \quad (2.2)$$

where $\tilde{I}(k)$ is the intensity that captured at CCDs, $\tilde{E}_R(k)$ and $\tilde{E}_S(k)$ are electric fields in spectral domain of reference and sample arms, respectively. The equation 2.2 can be rewritten as

$$\begin{aligned} \tilde{I}(k) &= (\tilde{E}_R(k) + \tilde{E}_S(k))(\tilde{E}_R(k) + \tilde{E}_S(k))^*, \\ \tilde{I}(k) &= \tilde{E}_R(k)\tilde{E}_R^*(k) + \tilde{E}_R(k)\tilde{E}_S^*(k) + \tilde{E}_S(k)\tilde{E}_R^*(k) + \tilde{E}_S(k)\tilde{E}_S^*(k), \\ \tilde{I}(k) &= |\tilde{E}_R(k)|^2 + |\tilde{E}_S(k)|^2 + \tilde{E}_R(k)\tilde{E}_S^*(k) + \tilde{E}_S(k)\tilde{E}_R^*(k), \\ \tilde{I}(k) &= |\tilde{E}_R(k)|^2 + |\tilde{E}_S(k)|^2 + 2\text{Re}\{\tilde{E}_R(k)\tilde{E}_S^*(k)\}. \end{aligned} \quad (2.3)$$

The expression round-trip propagation of an electric field of the reference arm and sample arm can be expressed as follow

$$\tilde{E}_R(k) = L_R \tilde{E}_{R0}(k) r_R \exp(jkz_R), \quad (2.4)$$

$$\tilde{E}_S(k) = L_S \tilde{E}_{S0}(k) \int_{-\infty}^{\infty} r_S(z_S) \exp(jkz_S) dz_S, \quad (2.5)$$

where L_R is loss-coefficient in the reference arm, L_S is loss-coefficient in the sample arm, $\tilde{E}_{R0}(k)$ is the amplitude of electric field in the reference arm, $\tilde{E}_{S0}(k)$ is the amplitude of electric field in sample arm, r_R is the reflectivity of a mirror in the reference arm, z_R is the round-trip optical path of light traveled in the reference arm.

The electric field of the sample arm consists of many backscattered lights from many

layers of a sample, having different path lengths. Hence, the $\tilde{E}_S(k)$ term is the combination from all possible distance as shown in the integral in equation 2.5. $r_S(z_S)$ is the reflectivity of the sample as a function of optical path length (figure 2.8(b)), which smaller in deeper region caused by light attenuation in depth, and z_S is the round-trip optical path length of light traveled in the sample arm. Substitute $\tilde{E}_R(k)$ and $\tilde{E}_S(k)$ into equation 2.3,

$$\begin{aligned} \tilde{I}(k) = & (L_R^2 \tilde{E}_{R0}^2(k) r_R^2) + \left[L_S^2 \tilde{E}_{S0}^2(k) \left(\int_{-\infty}^{\infty} r_S(z_S) \exp(jkz_S) dz_S \right)^2 \right] \\ & + 2L_R L_S \tilde{E}_{R0}(k) \tilde{E}_{S0}(k) r_R \int_{-\infty}^{\infty} r_S(z_S) \cos(jk(z_R - z_S)) dz_S. \end{aligned} \quad (2.6)$$

Assuming the perfect beam splitter, $\tilde{E}_{R0}(k) = \tilde{E}_{S0}(k) = \tilde{E}_0(k)$, then the equation 2.6 becomes

$$\begin{aligned} \tilde{I}(k) = & (L_R^2 \tilde{E}_0^2(k) r_R^2) + \left[L_S^2 \tilde{E}_0^2(k) \left(\int_{-\infty}^{\infty} r_S(z_S) \exp(jkz_S) dz_S \right)^2 \right] \\ & + 2L_R L_S \tilde{E}_0^2(k) r_R \int_{-\infty}^{\infty} r_S(z_S) \cos(jk(z_R - z_S)) dz_S. \end{aligned} \quad (2.7)$$

By introducing the optical path difference (OPD): $z_d = z_R - z_S$, and rewrite the equation 2.7, we obtain

$$\begin{aligned} \tilde{I}(k) = & (L_R^2 \tilde{E}_0^2(k) r_R^2) + \left[L_S^2 \tilde{E}_0^2(k) \left(\int_{-\infty}^{\infty} r_S(z_d) \exp(jkz_d) dz_d \right)^2 \right] \\ & + 2L_R L_S \tilde{E}_0^2(k) r_R \int_{-\infty}^{\infty} r_S(z_d) \cos(jk(z_d)) dz_d, \end{aligned} \quad (2.8)$$

because z_R is fixed, we can rewrite r_S as a function of z_d .

In equation 2.8, the first term is called “DC”, which is the power of reference arm, this term can be removed by subtraction in the software. The second term is the autocorrelation term, where is the signal from the sample arm interferes with itself, which can be neglectable because of this term is typically smaller than the other two terms. The third term is the interference term between the reference signal and signal from the sample arm. Nevertheless, the interference signal occurred when the OPD less than coherence length due to the low coherence interferometry from the broadband laser, e.g., SLD.

Considering the interference signal term,

$$\tilde{I}_{int}(k) = 2L_R L_S \tilde{E}_0^2(k) r_R \int_{-\infty}^{\infty} r_S(z_d) \cos(jk(z_d)) dz_d, \quad (2.9)$$

using the Euler's identity: $\cos(x) = \frac{1}{2}(e^{jx} + e^{-jx})$, and let the power of spectra $\tilde{S}(k) = \tilde{E}_0^2(k)$. Then equation 2.9 becomes

$$\tilde{I}_{int}(k) = L_R L_S \tilde{S}(k) r_R \left[\int_{-\infty}^{\infty} r_S(z_d) \exp(jkz_d) dz_d + \int_{-\infty}^{\infty} r_S(z_d) \exp(-jkz_d) dz_d \right]. \quad (2.10)$$

Using $\mathcal{F}\{\}$ is Fourier transformation, which has the definition (Bailey and Swartztrauber, 1994) as

$$F(k) = \mathcal{F}\{f(x)\} = \int_{-\infty}^{\infty} f(x) \exp(jkx) dx, \quad (2.11)$$

then, we obtain

$$\tilde{I}_{int}(k) = L_R L_S \tilde{S}(k) r_R [\mathcal{F}\{r_S(z_d)\} + \mathcal{F}\{r_S(-z_d)\}], \quad (2.12)$$

where equation 2.12 obtained from the interference after DC signal subtraction.

Performing the inverse Fourier transform to obtain the depth profile $I_{OCT}(z_d)$ in the spatial domain, then equation 2.12 becomes,

$$I_{OCT}(z_d) = \mathcal{F}^{-1}\{\tilde{I}_{int}(k)\} = L_R L_S r_R [\mathcal{F}^{-1}\{\tilde{S}(k)\} * (r_S(z_d) + r_S(-z_d))]. \quad (2.13)$$

From equation 2.13, the inverse Fourier transform of power spectra $\mathcal{F}^{-1}\{\tilde{S}(k)\}$ is the axial point spread function (PSF). The depth profile can be obtained from the convolution between the PSF and the reflectivity of a sample (figure 2.8(b)) located at z_d and $-z_d$.

In figure 2.8. shows the process of data acquisition in OCT imaging. The laser beam penetrates and reflected to the sample arm. Considering equation 2.13, there is only one surface included in the calculation. When there are multiple layers in real sample (figure 2.8(a)), the imaging system can capture all layers at once, i.e., more terms in equation 2.9 were obtained, and the interference signal that we acquired at the detector was shown in figure 2.8(d). The depth profile was created follow the process from equation 2.9 through equation 2.13 for only one lateral position, many peaks of convolution product were obtained represent many layers as shown in figure 2.8(e). To perform the 2D or 3D profile, the scanning mirror in the sample arm will be relocated (can operate in both x-axis and y-axis) the position of the mirror to other lateral positions, then do the same process to obtain the depth profile at that position. 2D depth profile or cross-section or B-mode can be obtained from sorting the consecutive depth profile along a single plane as shown in figure 2.8(f) and 2.8(g). Further sorting in another plane also obtains the 3D depth profile of the sample as shown in figure 2.9.

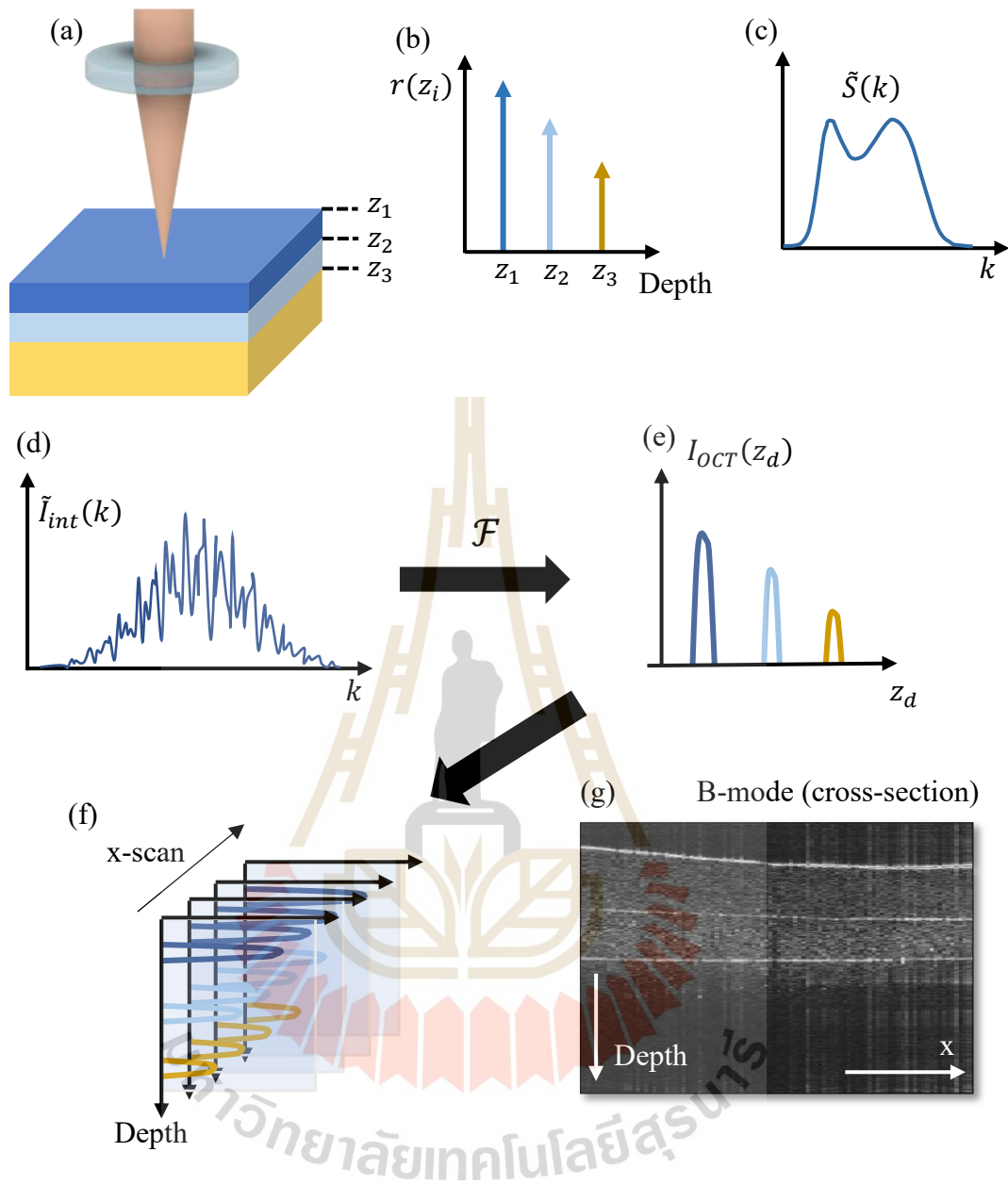


Figure 2.8 (a) Multilayer sample at different OPL of z_1 , z_2 , z_3 . (b) Reflectivity of a sample as a function of OPL. (c) Shape of spectrum from the light source. (d) Interference signal acquired at detector of OCT imaging. (e) Depth profile from interference signal. (f) B-mode or cross-section image from sorting consecutive depth profile along x-axis.

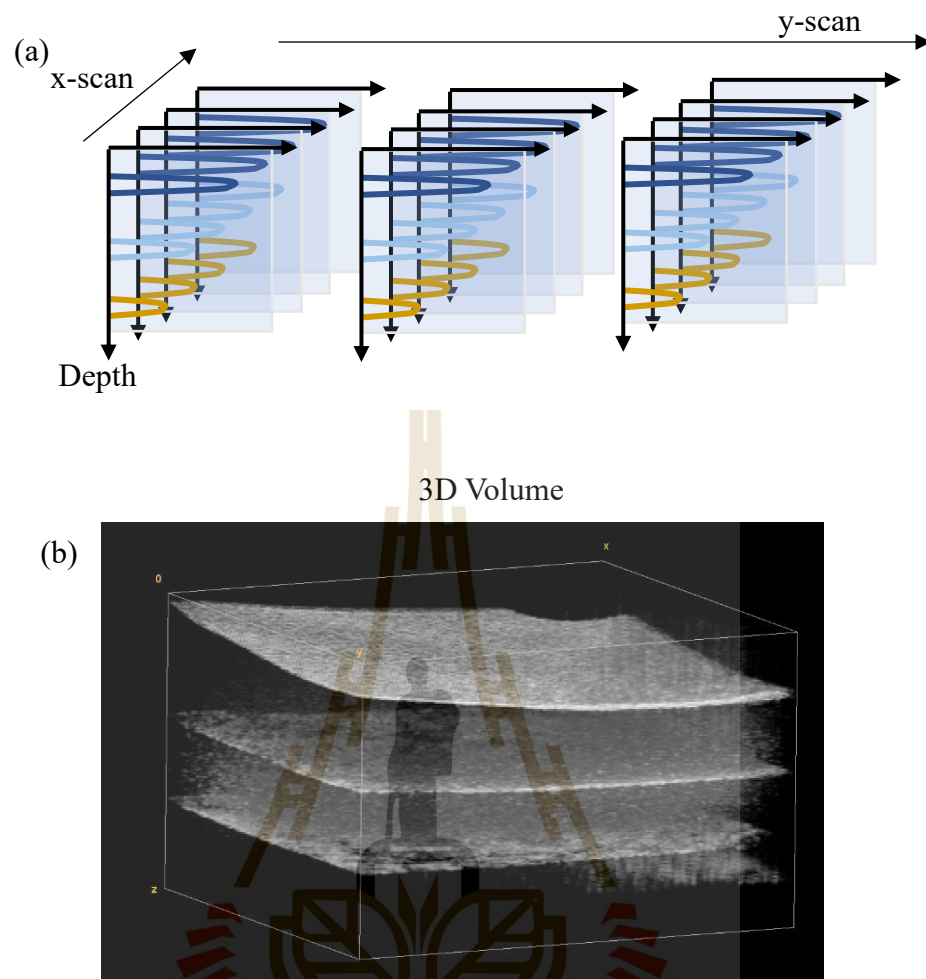


Figure 2.9 (a) Acquisition process to obtain the 3D depth profile by sorting PSF over x-axis and repeat the process for all y-axis. (b) a 3D volume of multilayers sample.

In image acquisition, the vision was obtained by collecting the reflected light from the object. If the object has high light absorbance, less of reflected light will be collected from our device. According to OCT widely used in medical field, i.e., imaging the biological tissue (Jiasong et al., 2013; Kennedy et al., 2009; Li et al., 2012; Manapuram et al., 2012; Manduca et al., 2001; Ophir et al., 1991; Song et al., 2015; F. Zvietcovich et al., 2019), which consists of water as a major component. Figure 2.10 shows the relative absorption of the biological components. To avoid absorption by water, the near-infrared (NIR) range provides a suitable window for imaging biological tissue (Fercher et al., 2003) and widely used in FD-OCT, and the light source that provides both coherence length and have wavelength in NIR range can be found in SLD. The example of spectra of SLD was shown in figure 2.11, many wavelengths provided, which caused the light source has small coherence gate.

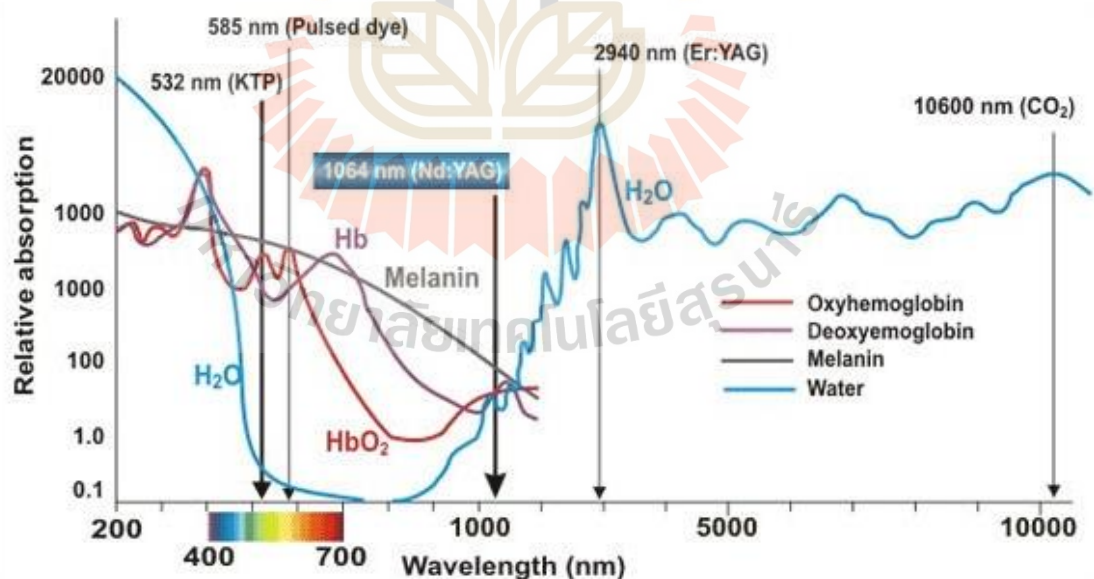


Figure 2.10 The relative absorption of biological component shows less absorption of water in NIR range (drop of blue curve).

(<http://westcoastlaser.com>)

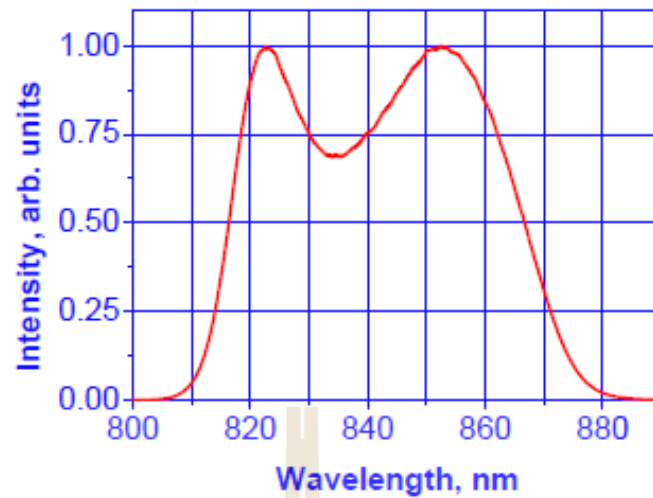


Figure 2.11 Example of spectra of SLD light source (S840-B-I-20, Superlum, Ireland).

Image resolution is an important factor for structural analysis of the tissue. There are two resolutions concerned in OCT imaging, i.e., the lateral and axial resolutions. The lateral resolution is the resolution from the diffraction limit of the objective lens (Davis, 2008; Fercher et al., 2003) in the sample arm, which is used for focusing the beam and collecting the backscattered light from the tissue. The diffraction limit of the objective lens is given by,

$$\Delta x = 1.22\lambda \frac{f}{D}, \quad (2.14)$$

where f , λ , and D are focal length of the objective lens, wavelength, and diameter of laser beam, respectively.

The axial resolution or depth resolution is defined by the coherent length as described by equation 2.1 (Fercher et al., 2003; Schmitt, 1999) and rewritten again as

$$\Delta z = \frac{2 \ln 2}{\pi} \frac{\bar{\lambda}^2}{\Delta \lambda}, \quad (2.15)$$

Considering equation 2.15, a larger bandwidth leads to a smaller axial resolution. Both lateral and axial resolution are independent of each other, so the OCT imaging resolution can be adjusted and optimized separately (Fercher et al., 2003). The penetration depth is commonly approximated at about 10 dB intensity dropped.

2.2.5 Signal-to-Noise Ratio (SNR)

Looking at the high-quality image, noise is the thing that no one wanted in the image but cannot be avoided. Noise is one of the indicators that is used to determine the quality of the image. The widely used indicator is the signal-to-noise ratio (*SNR*). *SNR* or *S/N* is the comparison between the power of an acquired signal to the power of background noise as follows,

$$SNR = \frac{P_{signal}}{P_{noise}}, \quad (2.16)$$

where P_{signal} , P_{noise} are the power of signal and noise, respectively. However, *SNR* is usually expressed in terms of decibels (Karimi and Navidbakhsh, 2014) as follows,

$$SNR_{(dB)} = 10 \log_{10}(SNR) = 10 \log_{10} \left(\frac{P_{signal}}{P_{noise}} \right) \quad (2.17)$$

For instance, if the ratio is 10:1, $SNR_{(dB)} = 10$ dB ("The Authoritative Dictionary of IEEE Standards Terms, Seventh Edition," 2000). A higher number of *SNR* means better useful data is obtained (signal) rather than unwanted data (noise).

One of the noises that affect the detection quality is shot noise. The expression of shot noise in optics is the fluctuations of incoming photons detected at the sensor or well-known by the term “counted”. Shot noise is usually found in imaging sensors, e.g., photomultiplier, Charge-coupled devices (CCDs), and Complementary Metal-Oxide-Silicon (CMOS).

CCDs sensors have low noise because of the structure of CCDs themselves, the charge from every pixel is converted to a voltage signal by only a single chip output amplifier. Although CCD has low noise, the existence of a single-chip output amplifier has limited by bottlenecked readout speed, and also consumed a lot of power, CMOS sensor can eliminate many problems that CCD have, such as faster readout, low power consumption, and lower price compared to CCD sensor. However, CMOS sensors can generate temporal noises that lead to poorer performance than CCD sensors (Tian, 2000).

Imaging sensors like CCDs and CMOS can be found in daily life, such as digital cameras, mobile phones, laptops, automotive, telecommunications, as well as OCT imaging. OCT is a sensitive technique based on the interferometer. In TD-OCT, the length for scanning of the reference arm corresponds to how much depth is obtained in the sample. On the other hand, there is no moving part on the scanning of the reference arm in FD-OCT. FD-OCT provides better SNR than TD-OCT because the shot noise generated by the power density of one specific wavelength is presented in the single detector, while FD-OCT has a line array detector that reduced the impact of shot noise (Boer et al., 2003). From higher SNR advantage in FD-OCT, retinal imaging (*in vivo*), 3D volumetric imaging, high-resolution imaging, and Doppler blood flow imaging can be obtained (Wang and Larin, 2015).

For high-quality imaging in OCT, noise should be minimized. Boer et al. showed that the shot noise can be reduced corresponds to the number of the detector in imaging configuration, and the noise was lower for each detector channel than the sum of all channels (Boer et al., 2003). Therefore, SNR will be increased when reduces the shot noise, is obtained by using the multi-element array detector. Bo *et al.* used a dual-balanced detector (DBD) in their FD-OCT to increase the SNR by combining two interference signals with π phase difference (Bo et al., 2016).

Elastography provides the elastic properties of the sample by measuring the mechanical response. Noise will reduce the data accuracy in elastography. If the imaging system has low SNR, the large noise compared to the data will lead to the inaccuracy of strain estimation (Bilgen and Insana, 1997; McGarry et al., 2011; Rehman et al., 2015).

2.3 Optical Coherence Elastography (OCE)

2.3.1 Concept of elastic measurements

There are many methods to obtain the elastic properties of materials, such as standard compression tests that rely on the relationship between input stress and output strain (Karimi and Navidbakhsh, 2014; Wang and Larin, 2015). However, this technique is destructive. And is not suitable for biomedical samples *in situ*. The non-destructive, non-invasive method like OCE is more applicable for biomedical applications. Three major groups have been used to obtain the tissue mechanical properties, i.e., measuring strain, measuring the natural frequency, and tracking elastic wave propagation. In this thesis, we focus on the analysis of elastic wave propagation. When the tissue is deformed, the wave propagation will exhibit mechanical properties.

Applying the wave propagation technique to our OCT system that is already existed in our facility is the most suitable choice compared to other techniques. This section will explain the principle of waves, and some mathematics about the elastic wave on the sample.

Wave propagation is the effect of disturbance in a medium that transmits to another part of the medium (Graff, 2012). This effect is familiar in daily life such as sound, water ripple, and radio waves. Figure 2.12 describes 2 types of waves: body waves and surface waves. The body waves can be further divided into 2 major types, i.e., primary waves (P-waves) and secondary waves (S-waves). P-waves occur when the source of vibration is applied to the medium, where the particle moves in the same direction of the wave propagation. The result of P-waves generates the local compression and expansion of the medium, known as a sound wave or pressure wave as shown in figure 2.13 (Onajite, 2014; K. J. Parker et al., 2010; Worden, 2001).

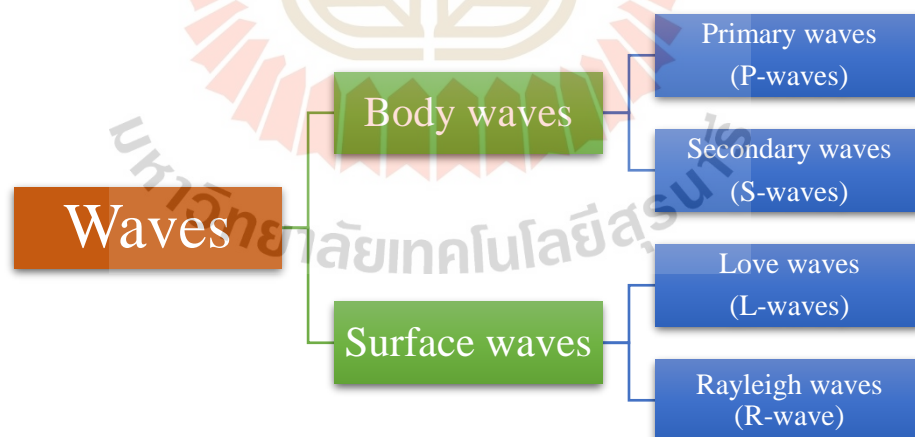


Figure 2.12 Type of waves.

S-waves or shear waves occur when the source of vibration is applied in a perpendicular direction to the surface of the medium. Shear waves move through the body of the medium, unlike surface waves as shown in figure 2.14 (Onajite, 2014).

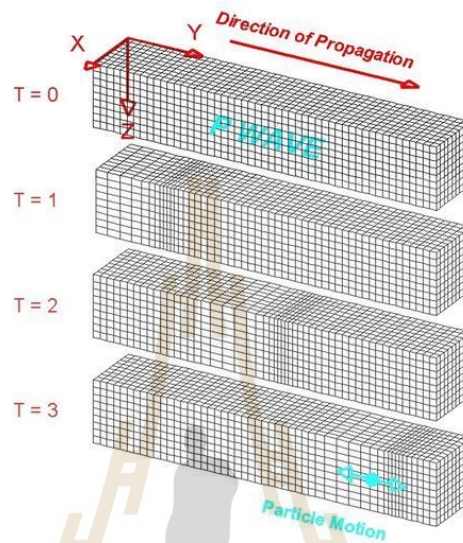


Figure 2.13 P-waves propagation.

(<http://www.geo.mtu.edu/UPSeis/waves.html>)

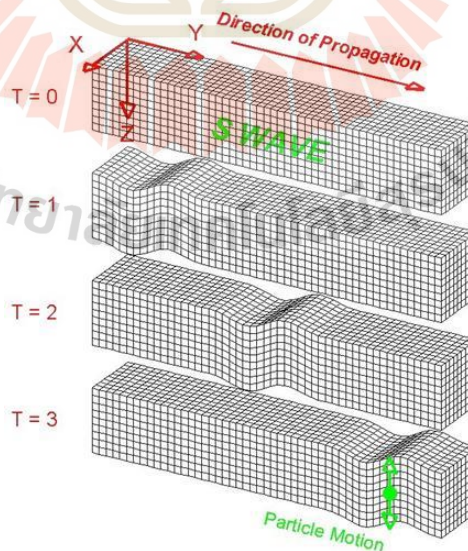


Figure 2.14 S-waves propagation.

(<http://www.geo.mtu.edu/UPSeis/waves.html>)

Surface waves propagate along the surface with a lower frequency than the body waves, the wave amplitude quickly dropped along with depth and can penetrate the medium approximately equal to the wavelength (Saavedra et al., 2017; Worden, 2001). Surface waves can further be divided into 2 types: Love waves and Rayleigh waves.

As shown in figure 2.15, Love waves (L-waves) occur when the particle moves in a horizontal plane (parallel to the medium surface) and perpendicular to the direction of propagation (transverse waves). Rayleigh waves (R-waves) occur in both transverse and longitudinal directions, the elliptical trajectory of a particle was generated in a plane that is normal to the surface and parallel to the direction of wave propagation as shown in figure 2.16.

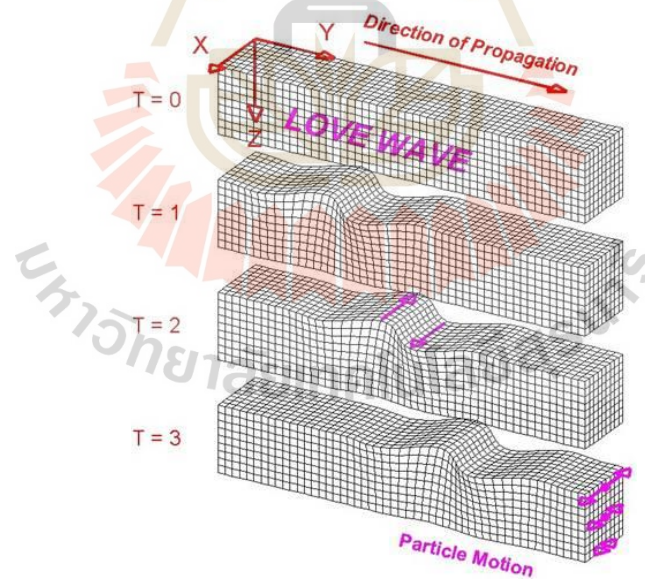


Figure 2.15 L-waves propagation.

(<http://www.geo.mtu.edu/UPSeis/waves.html>)

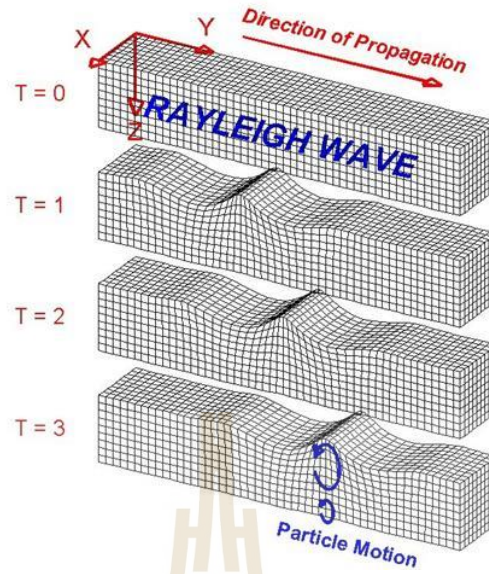


Figure 2.16 R-waves propagation.

(<http://www.geo.mtu.edu/UPSeis/waves.html>)

In the elastic wave on tissue, to reduce the mathematical complexity, the sample was assumed to be the incompressible isotropic linear elastic medium like soft tissue. Consider the wave equation follows (Hoyt et al., 2008; Lifshitz et al., 1986)

$$\frac{E}{2(1+\nu)} \nabla^2 \bar{u} + \frac{E}{2(1+\nu)(1-2\nu)} \nabla(\nabla \cdot \bar{u}) = \rho \frac{\partial^2 \bar{u}}{\partial t^2}, \quad (2.18)$$

where E, ν, \bar{u}, t, ρ are Young's modulus, Poisson's ratio, displacement vector, time variable, and density of the medium, respectively. This equation can separate into two equations, i.e., the longitudinal wave and shear wave equations. The shear wave component can be expressed as,

$$\nabla^2 \bar{u}_s - \frac{1}{v_s^2} \frac{\partial^2 \bar{u}_s}{\partial t^2} = 0, \quad (2.19)$$

where \bar{u}_s, v_s are the shear displacement vector, and shear wave speed, respectively.

From the equation above, v_s can be expressed as,

$$v_s = \sqrt{\frac{G}{\rho}}, \quad (2.20)$$

where the shear wave speed can be obtained from the relationship of shear modulus G and mass density of the medium ρ .

The second equation can be expressed by

$$\begin{aligned} \nabla(\nabla \cdot \bar{u}_p) - \frac{1}{v_p^2} \frac{\partial^2 \bar{u}_p}{\partial t^2} &= 0, \\ \nabla^2 \bar{u}_p + \nabla \times (\nabla \times \bar{u}_p) - \frac{1}{v_p^2} \frac{\partial^2 \bar{u}_p}{\partial t^2} &= 0. \end{aligned} \quad (2.21)$$

Since the pressure waves propagate in plane, which is no rotation. Therefore, $\nabla \times \bar{u}_p$ the term equal to zero (K. J. Parker et al., 2010), i.e.,

$$\nabla^2 \bar{u}_p - \frac{1}{v_p^2} \frac{\partial^2 \bar{u}_p}{\partial t^2} = 0, \quad (2.22)$$

The pressure waves speed c_p can be expressed by

$$v_p = \sqrt{\frac{\lambda + 2G}{\rho}}, \quad (2.23)$$

where λ is the Lamé parameter. From the results of the speed of the shear wave and pressure wave, the pressure wave speed is greater or equal to the square root of 2 as compared with shear velocity v_s as (Onajite, 2014; K. J. Parker et al., 2010),

$$\frac{v_p}{v_s} \geq \sqrt{2}, \quad (2.24)$$

and the expression of shear modulus G follows (Salencon and Bechtel, 2002),

$$G = \frac{E}{2(1 + \nu)}. \quad (2.25)$$

According to soft tissue (incompressible medium, high percentage of water in the sample), the Poisson's ratio ν was used at approximately about 0.5, and the shear modulus G becomes,

$$G = \frac{E}{3}. \quad (2.26)$$

Therefore, the stiffness informations of the medium can be obtained from the relationship of shear wave speed, density, and Young's modulus as follows,

$$v_s = \sqrt{\frac{G}{\rho}} = \sqrt{\frac{E}{3\rho}}. \quad (2.27)$$

Because the penetration depth of OCT imaging is approximately a few millimeters beneath the surface, the surface waves (Rayleigh waves) will more dominate than the body waves (shear waves) in nearly close to the surface region. Since the shear wave speed travels in biological tissue is ranging from 0.1 to 10 m/s , Rayleigh waves have speed v_R less than speed of shear waves v_s , which depends on the elastic constant of the medium as shown by the relationship follows (Saavedra et al., 2017; Zvietcovich, Rolland and Parker, 2017)

$$v_R = \frac{0.87 + 1.12\nu}{1 + \nu} * v_s. \quad (2.28)$$

Since the shear wave speed relates to elasticity, shear wave speed determination is important in elastography. However, there are multiple reflections of waves that propagate to structures and boundaries of real tissue. Parker et al. introduces shear wave reverberant fields concept to obtain the efficient estimators for shear wave speed calculation (K. J. Parker et al., 2017).

The complex pressure at position r : $\vec{P}(\vec{r})$, which can be determined from the superposition of plane wave from all directions (see figure 2.17), can be expressed as

$$\vec{P}(t, \vec{r}) = \sum_q \vec{P}_q \exp[j(k\hat{n}_q \cdot \vec{r} - \omega_0 t)], \quad (2.29)$$

where the index q represents the direction of wave propagation, \hat{n}_q represents unit vector in the randomly direction of propagation of q^{th} wave, k is wavenumber, ω is radial frequency of the plane waves, \vec{P}_q is random magnitude and phase of q^{th} wave. From the plane wave impedance relations (Kevin J. Parker and Maye, 1984), i.e.

$$\vec{v}_q = \frac{\hat{n}_q \vec{P}_q}{\rho c}, \quad (2.30)$$

where, ρ is density of the medium, c is speed of sound in medium. The corresponding velocity are given by equation 2.30 can be expressed as

$$\vec{v}(t, \vec{r}) = \sum_q \vec{v}_q \hat{n}_q \exp [j(k\hat{n}_q \cdot \vec{r} - \omega_0 t)], \quad (2.31)$$

where \vec{v}_q is the particle velocity. For simplicity of mathematics, let the detection axis be placed at the x -axis. Figure 2.17 shows the schematic and the axis definitions for the reverberant shear wave field concept. θ, ϕ is the angle between the vector of the reverberant field \vec{r} and z -axis, and x -axis, respectively, blue and yellow color represent the direction of random displacement of the surface after the wave traveling in the medium. Using a spherical coordinate system, i.e., $\hat{n}_q = \cos\alpha \hat{\phi} + \sin\alpha \hat{\theta}$, where $\hat{\theta} = \cos\theta \cos\phi \hat{x} + \cos\theta \sin\phi \hat{y} - \sin\theta \hat{z}$, and $\hat{\phi} = -\sin\phi \hat{x} + \cos\phi \hat{y}$.

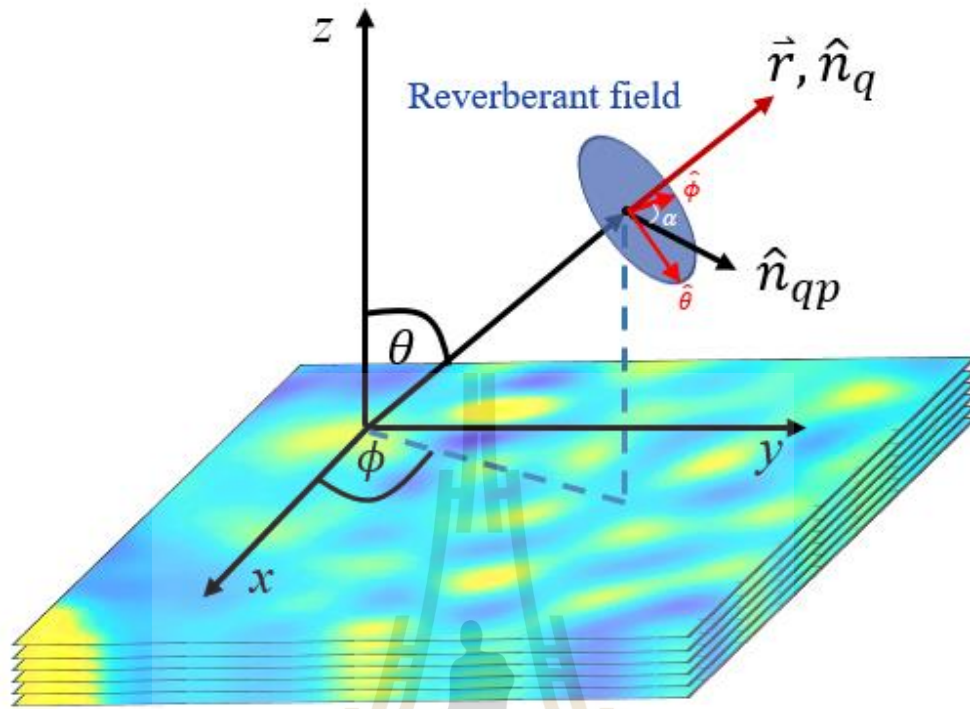


Figure 2.17 Schematic and axis definitions for the reverberant shear wave field concept (K. J. Parker et al., 2017).

For simplicity, let's consider the velocity in x component at some position \vec{r}

$$v_x(\vec{r}) = \hat{x} \cdot \vec{v}(t, \vec{r}) = \hat{x} \cdot \sum_q \vec{v}_q \hat{n}_q \exp[j(k\hat{n}_q \cdot \vec{r} - \omega_0 t)], \quad (2.32)$$

$$v_x(\vec{r}) = \sum_q \vec{v}_q \hat{n}_{qx} \exp[j(kn_q \cdot \vec{r} - \omega_0 t)], \quad (2.33)$$

where $\hat{n}_{qx} = \hat{n}_q \cdot \hat{x} = \sin\alpha \cos\theta \cos\phi - \cos\alpha \sin\phi$, and \hat{x} is the unit vector in the x direction. Summation is calculated over 4π solid angle. The autocorrelation function B_{xx} can be written as

$$B_{xx}(\Delta t, \Delta \vec{r}) = E\{v_x(t, \vec{r})v_x^*(t + \Delta t, \vec{r} + \Delta \vec{r})\} \quad (2.34)$$

Substitute \hat{v}_x , into correlation function,

$$\begin{aligned} &= E \left\{ \left(\sum_q \vec{v}_q \hat{n}_{qx} \exp[j(k\hat{n}_q \cdot \vec{r} - \omega_0 t)] \right) \right\} \\ &\quad \times \left\{ \sum_q \vec{v}_q^* \hat{n}_{qx}^* \exp[-j(k\hat{n}_q \cdot (\vec{r} + \Delta \vec{r}) - \omega_0(t + \Delta t))] \right\} \\ &= E \left\{ \sum_q \vec{v}_q \hat{n}_{qx} \vec{v}_q^* \hat{n}_{qx}^* \exp[j(k\hat{n}_q \cdot \vec{r} - k\hat{n}_q \cdot \vec{r} - k\hat{n}_q \cdot \Delta \vec{r} + \omega_0 \Delta t)] \right\}, \end{aligned} \quad (2.35)$$

where $E\{\}$ represents the ensemble average and the asterisk (*) is conjugation.

Since the \hat{n}_{qx} is independent, and \vec{v}_q uncorrelated,

$$B_{xx}(\Delta t, \Delta \vec{r}) = E \left\{ \sum_q \vec{v}_q^2 \hat{n}_{qx}^2 \exp[j(\omega_0 \Delta t - k\hat{n}_q \cdot \Delta \vec{r})] \right\}, \quad (2.36)$$

taking the real part, and since the \vec{v}_q is independent of \hat{n}_{qx} and cosine term, we obtain

$$B_{xx}(\Delta t, \Delta \vec{r}) = V_{avg}^2 E \left\{ \sum_q \hat{n}_{qx}^2 \cos(\omega_0 \Delta t - k\hat{n}_q \cdot \Delta \vec{r}) \right\}, \quad (2.37)$$

where V_{avg}^2 determined from the mean squared value of velocity \vec{v}_q^2 .

The average of discrete direction q becomes the average from all directions of incident waves over 4π solid angle, and weighting of particle velocity in 2π angle of the disk (blue disk in figure 2.17) (K. J. Parker et al., 2017).

$$B_{xx}(\Delta t, \Delta \vec{r}) = \frac{V_{avg}^2}{4\pi} \int_{sphere} \frac{1}{2\pi} \hat{n}_{qx}^2 \cos(\omega_0 \Delta t - k\hat{n}_q \cdot \Delta \vec{r}) d\Omega. \quad (2.38)$$

The correlation function solutions were considered into two cases: perpendicular and parallel cases respect to the detection axis. For the first case, we considered to align $\Delta\vec{r}$ in z -axis, which perpendicular to the detection axis (x -axis). The $\hat{n}_q \cdot \Delta\vec{r}$ in exponential term can be written as

$$\hat{n}_q \cdot \Delta\vec{r} = \Delta r_z \cos\theta, \quad (2.39)$$

and solid angle,

$$d\Omega = \sin\theta d\theta d\phi, \quad (2.40)$$

and

$$\hat{n}_{qx}^2 = (\hat{n}_q \cdot \hat{x})^2 = (\sin\alpha \cos\theta \cos\phi - \cos\alpha \sin\phi)^2, \quad (2.41)$$

so,

$$B_{xx}(\Delta t, \Delta r_z) = \frac{V_{avg}^2}{4\pi} \int_{\alpha=0}^{\alpha=2\pi} \int_{\phi=0}^{\phi=2\pi} \int_{\theta=0}^{\theta=\pi} \frac{1}{2\pi} (\sin\alpha \cos\theta \cos\phi - \cos\alpha \sin\phi)^2 \cos(\omega_0 \Delta t - k\Delta r_z \cos\theta) \sin\theta d\theta d\phi d\alpha, \quad (2.42)$$

$$= \frac{V_{avg}^2}{8\pi^2} \int_{\alpha=0}^{\alpha=2\pi} \int_{\phi=0}^{\phi=2\pi} \int_{\theta=0}^{\theta=\pi} (\sin\alpha \cos\theta \cos\phi - \cos\alpha \sin\phi)^2 \cos(\omega_0 \Delta t - k\Delta r_z \cos\theta) \sin\theta d\theta d\phi d\alpha. \quad (2.43)$$

Consider the first term of the integrant

$$\begin{aligned} & (\sin\alpha \cos\theta \cos\phi - \cos\alpha \sin\phi)^2 \\ &= \sin^2\alpha \cos^2\theta \cos^2\phi - 2 \sin\alpha \cos\theta \cos\phi \cos\alpha \sin\phi \\ &+ \cos^2\alpha \sin^2\phi. \end{aligned} \quad (2.44)$$

The second term of the integrant, $\cos(\omega_0 \Delta t - k\Delta r_z \cos\theta) \sin\theta$, using the trigonometric identity, i.e., $\cos(A + B) = \cos A \cos B - \sin A \sin B$.

$$= \cos(\omega_0 \Delta t) \cos(k \Delta r_z \cos \theta) \sin \theta + \sin(\omega_0 \Delta t) \sin(k \Delta r_z \cos \theta) \sin \theta, \quad (2.45)$$

where the integration of the second term of equation 2.45 is neglectable because the integrand is an odd function.

The integrand of equation 2.43 becomes the multiplication of equation 2.44 and the first term of equation 2.45

$$\begin{aligned} &= [\sin^2 \alpha \cos^2 \theta \cos^2 \phi - 2 \sin \alpha \cos \theta \cos \phi \cos \alpha \sin \phi + \cos^2 \alpha \sin^2 \phi] \\ &\quad \times (\cos(\omega_0 \Delta t) \cos(k \Delta r_z \cos \theta) \sin \theta), \\ &= (\sin^2 \alpha \cos^2 \theta \cos^2 \phi) (\cos(\omega_0 \Delta t) \cos(k \Delta r_z \cos \theta) \sin \theta) \\ &\quad - (2 \sin \alpha \cos \theta \cos \phi \cos \alpha \sin \phi) (\cos(\omega_0 \Delta t) \cos(k \Delta r_z \cos \theta) \sin \theta) \\ &\quad + (\cos^2 \alpha \sin^2 \phi) (\cos(\omega_0 \Delta t) \cos(k \Delta r_z \cos \theta) \sin \theta). \end{aligned} \quad (2.46)$$

Solving three integration for each term in equation 2.46, start with the first term

$$\begin{aligned} &= \int_{\alpha=0}^{\alpha=2\pi} \int_{\phi=0}^{\phi=2\pi} \int_{\theta=0}^{\theta=\pi} (\sin^2 \alpha \cos^2 \theta \cos^2 \phi) (\cos(\omega_0 \Delta t) \cos(k \Delta r_z \cos \theta) \sin \theta) d\theta d\phi d\alpha, \\ &= \left[\int_{\alpha=0}^{\alpha=2\pi} \sin^2 \alpha d\alpha \right] \left[\int_{\phi=0}^{\phi=2\pi} \cos^2 \phi d\phi \right] \\ &\quad \times \left[\int_{\theta=0}^{\theta=\pi} \cos^2 \theta (\cos(\omega_0 \Delta t) \cos(k \Delta r_z \cos \theta)) \sin \theta d\theta \right]. \end{aligned} \quad (2.47)$$

Considering the first integration term,

$$\int_{\alpha=0}^{\alpha=2\pi} \sin^2 \alpha d\alpha = \int_{\alpha=0}^{\alpha=2\pi} \frac{1}{2} d\alpha - \int_{\alpha=0}^{\alpha=2\pi} \frac{1}{2} \cos 2\phi d\alpha,$$

$$\begin{aligned}
&= \int_{\alpha=0}^{\alpha=2\pi} \frac{1}{2} d\alpha - \int_{\alpha=0}^{\alpha=2\pi} \frac{1}{2} \cos 2\alpha d\alpha, \\
&= \frac{\alpha}{2} \Big|_{\alpha=0}^{\alpha=2\pi} - \frac{1}{2} \frac{\sin 2\alpha}{2} \Big|_{\alpha=0}^{\alpha=2\pi} = \pi.
\end{aligned} \tag{2.48}$$

The integration result of the second term in equation 2.47 is the same with first term.

$$\int_{\phi=0}^{\phi=2\pi} \cos^2 \phi d\phi = \pi. \tag{2.49}$$

Now, consider the integration of the third term in equation 2.47

$$\begin{aligned}
&\int_{\theta=0}^{\theta=\pi} \cos^2 \theta (\cos(\omega_0 \Delta t) \cos(k\Delta r_z \cos \theta)) \sin \theta d\theta \\
&= \cos(\omega_0 \Delta t) \int_{\theta=0}^{\theta=\pi} \cos^2 \theta \cos(k\Delta r_z \cos \theta) \sin \theta d\theta, \\
&= \cos(\omega_0 \Delta t) \int_{\theta=0}^{\theta=\pi} (1 - \sin^2 \theta) \cos(k\Delta r_z \cos \theta) \sin \theta d\theta, \\
&= \cos(\omega_0 \Delta t) \left[\int_{\theta=0}^{\theta=\pi} \cos(k\Delta r_z \cos \theta) \sin \theta d\theta \right. \\
&\quad \left. - \int_{\theta=0}^{\theta=\pi} \sin^3 \theta \cos(k\Delta r_z \cos \theta) d\theta \right].
\end{aligned} \tag{2.50}$$

Consider only the first term in equation 2.50, by changing variable,

$$u = k\Delta r_z \cos \theta,$$

then

$$du = -k\Delta r_z \sin \theta d\theta.$$

Therefore,

$$\begin{aligned}
 \int_{\theta=0}^{\theta=\pi} \cos(k\Delta r_z \cos\theta) \sin\theta d\theta &= \int_{u=k\Delta r_z}^{u=-k\Delta r_z} \cos(u) \frac{du}{-k\Delta r_z}, \\
 &= \frac{1}{-k\Delta r_z} \int_{u=k\Delta r_z}^{u=-k\Delta r_z} \cos(u) du, \\
 &= \frac{1}{-k\Delta r_z} \frac{\sin(u)}{1} \Big|_{u=k\Delta r_z}^{u=-k\Delta r_z}, \\
 &= \frac{1}{-k\Delta r_z} [\sin(-k\Delta r_z) - \sin(k\Delta r_z)], \\
 &= \frac{2 \sin(k\Delta r_z)}{k\Delta r_z}. \tag{2.51}
 \end{aligned}$$

The second term in equation 2.50 can be written in term of spherical Bessel function in the form (Abramowitz and Stegun, 1965),

$$j_n(z) = \frac{z^n}{2^{n+1}n!} \int_{\theta=0}^{\theta=\pi} \sin^{2n+1}\theta \cos(z \cos\theta) d\theta, \tag{2.52}$$

in our case, $n = 1$ and $z = k\Delta r_z$.

$$j_1(k\Delta r_z) = \frac{k\Delta r_z}{4} \int_{\theta=0}^{\theta=\pi} \sin^3\theta \cos(k\Delta r_z \cos\theta) d\theta. \tag{2.53}$$

Therefore, substitute equation 2.48, 2.49, 2.51, 2.53 into equation 2.47, the first term of correlation function $B_{xx}(\Delta t, \Delta r_z)$ in equation 2.46 can be obtained as follows

$$\int_{\alpha=0}^{\alpha=2\pi} \int_{\phi=0}^{\phi=2\pi} \int_{\theta=0}^{\theta=\pi} (\sin^2\alpha \cos^2\theta \cos^2\phi) (\cos(\omega_0\Delta t) \cos(k\Delta r_z \cos\theta) \sin\theta) d\theta d\phi d\alpha,$$

$$= \pi \cdot \pi \cdot \cos(\omega_0 \Delta t) \left[\frac{2 \sin(k\Delta r_z)}{k\Delta r_z} - \frac{4 j_1(k\Delta r_z)}{k\Delta r_z} \right]. \quad (2.54)$$

Equation 2.54 is integration only the first term in equation 2.46. Next, consider the integration of the second term in equation 2.46

$$= \left[\int_{\alpha=0}^{\alpha=2\pi} 2 \sin \alpha \cos \alpha d\alpha \right] \left[\int_{\phi=0}^{\phi=2\pi} \cos \phi \sin \phi d\phi \right] \times \left[\int_{\theta=0}^{\theta=\pi} \cos \theta (\cos(\omega_0 \Delta t) \cos(k\Delta r_z \cos \theta) \sin \theta) d\theta \right]. \quad (2.55)$$

Consider the first term,

$$\int_{\alpha=0}^{\alpha=2\pi} 2 \sin \alpha \cos \alpha d\alpha = \int_{\alpha=0}^{\alpha=2\pi} \sin 2\alpha d\alpha = \frac{\cos 2\alpha}{2} \Big|_0^{2\pi} = 0. \quad (2.56)$$

Thus, the integration of the second term in equation 2.46 becomes zero.

Next, the integration of the third term in equation 2.46 can be expressed as

$$= \left[\int_{\alpha=0}^{\alpha=2\pi} \cos^2 \alpha d\alpha \right] \left[\int_{\phi=0}^{\phi=2\pi} \sin^2 \phi d\phi \right] \left[\int_{\theta=0}^{\theta=\pi} \cos(\omega_0 \Delta t) \cos(k\Delta r_z \cos \theta) \sin \theta d\theta \right].$$

The first and second terms above are the same result with equation 2.48 and 2.49, also third term is the same with equation 2.51. Thus, the integration becomes

$$\int_{\alpha=0}^{\alpha=2\pi} \int_{\phi=0}^{\phi=2\pi} \int_{\theta=0}^{\theta=\pi} (\cos^2 \alpha \sin^2 \phi) (\cos(\omega_0 \Delta t) \cos(k\Delta r_z \cos \theta) \sin \theta) d\theta d\phi d\alpha = \pi \cdot \pi \cdot \cos(\omega_0 \Delta t) \left[\frac{2 \sin(k\Delta r_z)}{k\Delta r_z} \right]. \quad (2.57)$$

Finally, the correlation function in case of perpendicular to detection axis (x -axis) (equation 2.43) is the integration of equation 2.46, which is summation of equation 2.54, 2.56, and 2.57 together.

$$\begin{aligned}
B_{xx}(\Delta t, \Delta r_z) &= \frac{V_{avg}^2}{8\pi^2} \int_{\alpha=0}^{\alpha=2\pi} \int_{\phi=0}^{\phi=2\pi} \int_{\theta=0}^{\theta=\pi} (\sin\alpha\cos\theta\cos\phi - \cos\alpha\sin\phi)^2 \cos(\omega_0\Delta t \\
&\quad - k\Delta r_z\cos\theta) \sin\theta d\theta d\phi d\alpha, \\
&= \frac{V_{avg}^2}{8\pi^2} \left[\pi^2 \left[\frac{2\sin(k\Delta r_z)}{k\Delta r_z} - \frac{4j_1(k\Delta r_z)}{k\Delta r_z} \right] - 0 + \pi^2 \left[\frac{2\sin(k\Delta r_z)}{k\Delta r_z} \right] \right], \\
&= \frac{V_{avg}^2}{8\pi^2} \left[\pi^2 \left[\frac{4\sin(k\Delta r_z)}{k\Delta r_z} - \frac{4j_1(k\Delta r_z)}{k\Delta r_z} \right] \right].
\end{aligned}$$

Hence, the correlation function (perpendicular to the detection axis (x -axis) case) becomes

$$B_{xx}(\Delta t, \Delta r_z) = \frac{V_{avg}^2}{2} \cos(\omega_0\Delta t) \left[\frac{\sin(k\Delta r_z)}{k\Delta r_z} - \frac{j_1(k\Delta r_z)}{k\Delta r_z} \right]. \quad (2.58)$$

According to the orthogonal of x -axis, y -axis, and z -axis, we can redefine the detection axis to be z -axis and the result still identical by change the subscript “ z ” to “ x ” as follows

$$B_{zz}(\Delta t, \Delta r_x) = \frac{V_{avg}^2}{2} \cos(\omega_0\Delta t) \left[\frac{\sin(k\Delta r_x)}{k\Delta r_x} - \frac{j_1(k\Delta r_x)}{k\Delta r_x} \right], \quad (2.59)$$

in ideal, we can change the subscript “ x ” with “ y ” if assumed to isotropic symmetry.

The second case of correlation function is parallel to the detection axis. In this case, let the detection axis is at z -axis. The correspond particle velocity can be expressed as

$$v_z(\vec{r}) = \hat{z} \cdot \vec{v}(t, \vec{r}) = \sum_q \vec{v}_q \hat{n}_{qz} \exp[j(k\hat{n}_q \cdot \vec{r} - \omega_0 t)], \quad (2.60)$$

where $\hat{n}_{qz} = \hat{n}_q \cdot \hat{z} = -\sin\alpha \sin\theta$ (see figure 2.17), and \hat{z} is unit vector in the z direction. For the parallel case, we considered to align $\Delta\vec{r}$ in z -axis, which parallel to the detection axis (z -axis). The $\hat{n}_q \cdot \Delta\vec{r}$ in exponential term can be written as

$$\hat{n}_q \cdot \Delta \vec{r} = \Delta r_z \cos \theta, \quad (2.61)$$

and solid angle,

$$d\Omega = \sin \theta d\theta d\phi, \quad (2.62)$$

and

$$\hat{n}_{qz}^2 = (\hat{n}_q \cdot \hat{z})^2 = (-\sin \alpha \sin \theta)^2, \quad (2.63)$$

so,

$$\begin{aligned} B_{zz}(\Delta t, \Delta r_z) &= \frac{V_{avg}^2}{4\pi} \int_{\alpha=0}^{\alpha=2\pi} \int_{\phi=0}^{\phi=2\pi} \int_{\theta=0}^{\theta=\pi} \frac{1}{2\pi} (-\sin \alpha \sin \theta)^2 \cos(\omega_0 \Delta t \\ &\quad - k \Delta r_z \cos \theta) \sin \theta d\theta d\phi d\alpha, \\ &= \frac{V_{avg}^2}{8\pi^2} \left[\int_{\alpha=0}^{\alpha=2\pi} \sin^2 \alpha d\alpha \right] \left[\int_{\phi=0}^{\phi=2\pi} d\phi \right] \left[\int_{\theta=0}^{\theta=\pi} \sin^3 \theta \cos(\omega_0 \Delta t - k \Delta r_z \cos \theta) d\theta \right]. \end{aligned} \quad (2.64)$$

where the result of the term in first parentheses is the same with equation 2.48, and the result of second parentheses is 2π . The correlation function $B_{zz}(\Delta t, \Delta r_z)$ becomes

$$\begin{aligned} B_{zz}(\Delta t, \Delta r_z) &= \frac{V_{avg}^2}{8\pi^2} [\pi][2\pi] \left[\int_{\theta=0}^{\theta=\pi} \sin^3 \theta \cos(\omega_0 \Delta t - k \Delta r_z \cos \theta) d\theta \right], \\ B_{zz}(\Delta t, \Delta r_z) &= \frac{V_{avg}^2}{4} \left[\int_{\theta=0}^{\theta=\pi} \sin^3 \theta \cos(\omega_0 \Delta t - k \Delta r_z \cos \theta) d\theta \right]. \end{aligned} \quad (2.65)$$

The term in parentheses is the same with the second term in equation 2.50, which can be expressed in term of spherical Bessel function of the first kind of first order like equation 2.53. So, the correlation function in parallel case becomes

$$B_{zz}(\Delta t, \Delta r_z) = V_{avg}^2 \cos(\omega_0 \Delta t) \left[\frac{j_1(k \Delta r_z)}{k \Delta r_z} \right]. \quad (2.66)$$

Figure 2.18 shows the thin line and thick line represent the equation 2.59 and equation 2.66, respectively, in which the wavenumber k is set to equal for these two equations and there are spatial sinc functions. According to the multiple sources of excitations, many shear waves propagate and the surface displacement occurred within a region of interest (ROI). The correlation function is calculated to estimate the local wavenumber k . Notice that, the autocorrelation function in both x -axis and y -axis are the same result because of the radial symmetry, i.e., there are both perpendicular to the detection axis (z -axis). The correlation functions from the experiment were calculated and fit with either equation 2.59 or 2.66 to determine the perpendicular and parallel directions, respectively. The method to obtain the unknown local wavenumber k is by using the Fourier transform of the correlation function (K. J. Parker et al., 2017).

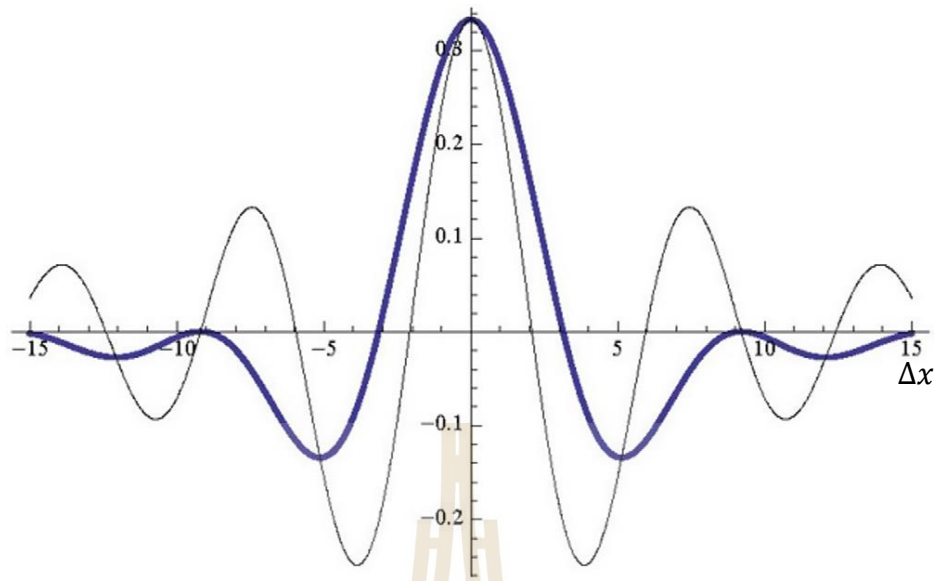


Figure 2.18 The autocorrelation results depend on the direction of the displacement Δr with the axis of detection. The correlation function with respect to the x -direction is shown in thin line (equation 2.59), and thick blue line is the correlation in z -direction (equation 2.66). These spatial sinc functions will be used for estimating local wavenumber k (K. J. Parker et al., 2017).

After the wavenumber is acquired, substitute the wavenumber into the phase velocity relationship as follows (Zvietcovich et al., 2017)

$$v_s = \frac{\omega}{k}, \quad (2.67)$$

where ω is the angular frequency and $\omega = 2\pi f$, which f is the piezoelectric input frequency from the function generator. Hence, the wavenumber is the key to the mapping of tissue characteristics through the phase velocity relation.

2.3.2 Excitation and detection schemes

Every tissue has mechanical properties. If the known input force is applied to the tissue, the response result will relate to the input value. OCE mainly uses the response of the tissue to differentiate the abnormal tissue from healthy tissues. It is impossible to use the typical elastic testing that measures stress and strain with human tissue and internal organs (*in situ*). Therefore, other techniques to produce mechanical loading into tissue are demanded. Various stimulation techniques used in OCE are summarized in table 2.3. The acoustic radiation force (ARF) excitation method uses short bursts of ultrasound waves to create tissue displacement in the focal region (Itoh et al., 2006; Song et al., 2015). The mechanical actuator method uses the property of the piezoelectric actuator to convert an electric signal into the mechanical movement and needs to contact the surface to create the tissue displacement (Kennedy et al., 2009; Li et al., 2012; F. Zvietcovich et al., 2019). However, both the ARF and actuator methods are contact methods. Other techniques, laser-induced surface acoustic wave (SAW) (Li et al., 2012), magnetic nanoparticles (MNPs) (Ahmad et al., 2014; Crecea et al., 2009; Manduca et al., 2001), and air-puff (Jiasong et al., 2013) are non-contact methods. MNPs technique needs to mix the magnetic particles into the tissue (Crecea et al., 2009), which means tissue preparation is required. Hence, MNPs technique is still an invasive method (Ahmad et al., 2014). For the laser-induced SAW method, the tissue might absorb heat from using a short pulse laser and will damage the tissue if the power of the laser source is too high (Li et al., 2011). The air-puff method uses low pressure of air focused on the surface of the tissue to create the surface displacement, which is a non-contact, non-invasive, non-destructive method also suitable for soft tissue such as skin,

and cornea. However, the air-puff method needs to be careful about the air pressure when used with soft tissue and quickly decrease the moisture of the tissue.

Table 2.3 OCE with various excitation methods.

Excitation techniques	Authors	Contact/ Non-contact method	Invasive/ Noninvasive method	Frequency of excitation
ARF	(Itoh et al., 2006)	Contact	Noninvasive	Not found
	(Song et al., 2015)			120 Hz
MNPs	(Crecea et al., 2009)	Non-contact	Invasive	10 Hz
	(Ahmad et al., 2014)			500 Hz
	(Manduca et al., 2001)			50-1,000 Hz
SAW	(Li et al., 2011)	Non-contact	Noninvasive	0.5 Hz
Air-puff	(Jiasong et al., 2013)	Non-contact	Noninvasive	125 Hz
Mechanical actuator	(Kennedy et al., 2009)	Contact	Noninvasive	820 Hz
	(Li et al., 2012)			20 Hz
	(Zvietcovich, Yao, Rolland, et al., 2016)			400 Hz
	(F. Zvietcovich et al., 2019)			1,000 Hz

Since the OCE imaging technique required external excitation, the mechanical actuator was used to convert a motion to another motion. OCE technique requires excitation at a sub-millimeter level. Thus, the useful choice for our system is the “piezoelectric actuator”, the material response to the voltage that causes it to expand. High voltages will produce only tiny expansions. When the piezoelectric actuator was activated, it will create tissue displacement perpendicular to the direction of shear wave propagation, which provides the mechanical properties of the sample through the speed of propagation. The tissue displacement affects the OPL in the interference signal,

which we can use phase to track back for tissue displacement determination. The relationship between axial displacement and phase difference can be expressed as follows (Li et al., 2012; Li et al., 2011; Wang and Larin, 2015)

$$u_z = \Delta\phi \frac{\lambda_0}{4\pi n}. \quad (2.68)$$

where u_z , $\Delta\phi$, λ_0 , n are the axial displacement, the phase difference from two consecutive A-scan of OCT imaging, the center wavelength of the broadband light source, and the refractive index of the medium (Zvietcovich et al., 2017), respectively.

2.4 Gelatin phantoms

For the initial development of OCE, the sample with elastic controllable is suitable for measurement rather than biological tissue, which is typically inhomogeneous (solid and liquid combination). Gelatin is used for representing the biological soft tissue because of its consistency, controllable size, and concentration-based properties, and is widely used in science, medical, and engineering research. Gelatin has ability to maintain its shape due to the irreversibly hydrolyzed form of collagen. Originally, gelatin dissolved with hot water is transparent gels. To use the gelatin phantom as a sample in OCT and OCE, the scattering material was added to the gelatin to create the light scattering from inside of the gelatin. For instance, fluorescent dye, Titanium dioxide (TiO_2), milk, coffee cream, etc. (Ahmad et al., 2014; Li et al., 2011; Manduca et al., 2001; Meemon et al., 2016; Wang and Larin, 2015)

In preparation of the gelatin phantom, the stiffness of the phantom was controlled by how much the gelatin powder is mixed in the solution: the higher gelatin, the higher stiffness. Mixed the gelatin powder with hot water and stir until all gelatin

dissolved, added scattering material, and then poured the solution into the mold, waited for the gelatin to form by cooling in the refrigerator or left on the table.

2.5 Standard mechanical testing

Standard mechanical testing is widely used in material science and engineering fields to obtain the mechanical properties of the sample. For elastic information of the sample, the standard compression test was used. The principle behind the compression test is Hook's law in one-dimension (Wang and Larin, 2015), by input the stress σ , which determined by the ratio of total loading force F to the surface area A . The result strain ε is recorded, which is the ratio of changes of length ΔL to the original length L . According to Hook's law, the slope of the relationship between stress and strain called Young's modulus E , which can be written as

$$E = \frac{\sigma}{\varepsilon} = \frac{F/A}{\Delta L/L} = \frac{FL}{A\Delta L} \quad (2.69)$$

A higher value of Young's modulus means the sample has higher stiffness. Figure 2.19 shows an example of the standard compression test machine: MTS Q-test5 universal testing machine (MTS, Eden Prairie, Minnesota, United States). The compression test was conducted by inputting the dimension of the sample such as diameter and height, putting the sample between two plates (see figure 2.19(b)), then applying the loading force by moving the top plate downward. The sensitive sensor that contacts the top plate recorded the information about the applied load, together with the distance that the top plate moved. Young's modulus can be obtained by determining the slope from the stress-strain graph.

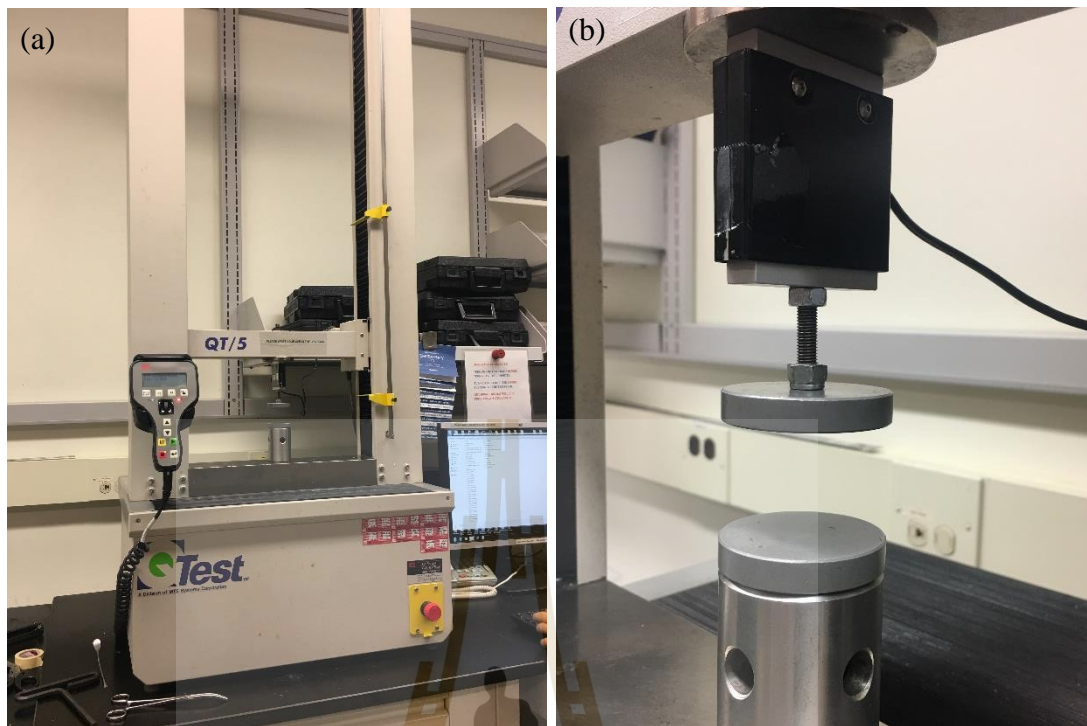


Figure 2.19 (a) The standard compression testing (MTS, Eden Prairie, Minnesota, United States). (b) Compression area of the compression test, the top plate moves downward and compressed the sample, sensor will record loading information together with the distance that the top plate moved.

CHAPTER III

RESEARCH METHODOLOGY

Our goal is to combine reverberant shear wave field concept and OCT imaging technique to determine the shear wave speed (SWS) on the sample. In the previous chapters, the details of elastography, OCE imaging system, and gelatin phantom were explained. This chapter describes the gelatin phantom preparations, OCE experimental setup, and data analysis process to obtain the SWS map of the sample from the OCT imaging data. The detection was operated by LabView software (National Instruments, Austin, TX, United States), which provides the interface to communicate with hardware as well as display data and other indicators to monitor the experiments. The data were analyzed by MATLAB™ (MathWorks, Massachusetts, United States).

3.1 Gelatin phantom preparations

Gelatin phantom is concentration-based material. Its stiffness can be controlled by the concentration of gelatin powder that is mixed in the solution. It is widely used in elastography as a tissue-mimicking phantom (Ahmad et al., 2014; Doyley and Parker, 2014; Li et al., 2012; F. Zvietcovich et al., 2019).

In this study, 3 % and 4% concentrations of weight by volume (wt%) of the gelatin phantom were prepared to represent soft and stiff tissues, which mimic healthy liver and septal fibrosis (Wang and Larin, 2015), respectively. Each concentration solution was mixed with 200 mL of DI-water (Deionize water) (assumed water density

is 1 g/mL), 6.20 g and 8.35 g of gelatin powders were mixed with water to produce 3 wt% and 4 wt% gelatin phantoms, respectively. 0.25 wt% coffee cream was added to the gelatin solution to introduce the optical scattering on the phantom. The refractive index of the gelatin phantom was approximately 1.35. In addition, a food color agent was added to identify each concentration. The mixed solution was put in the microwave oven for about 90 seconds for heating. After that, the solution was stirred with a magnetic stirrer until gelatin and coffee cream were completely dissolved. The air bubble was taken out from the solution for the perfect homogeneous sample as shown in figure 3.1. Then, the solution was gently poured into the food-grade silicone mold or glass Petri disk and left in the refrigerator for gelatinization. Figures 3.2(a) and 3.2(b) show the gelatin phantom with and without optical scatterer (coffee cream), respectively. Figure 3.2(d) shows a small portion of each gelatin concentration extracted in a cylindrical-shaped, i.e., 20 mm a diameter and 10 mm in height, for performing standard mechanical testing (MTS Q-Test5, MTS, Eden Prairie, MN, USA).

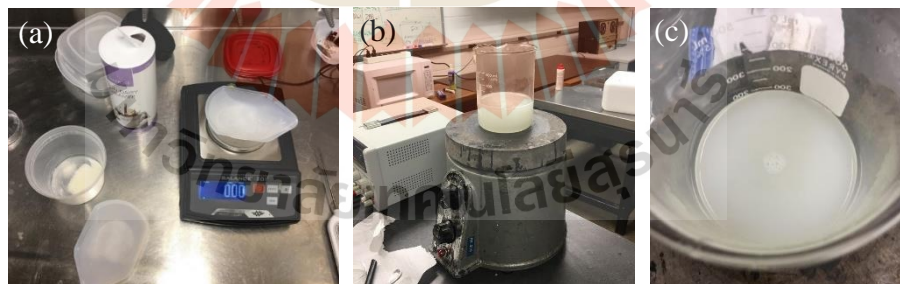


Figure 3.1 (a) Weight gelatin powder and coffee cream for specific concentrations.

(b) Gelatin solution with a magnetic stirrer.

(c) Air bubble in the liquid gelatin solution (in the middle).

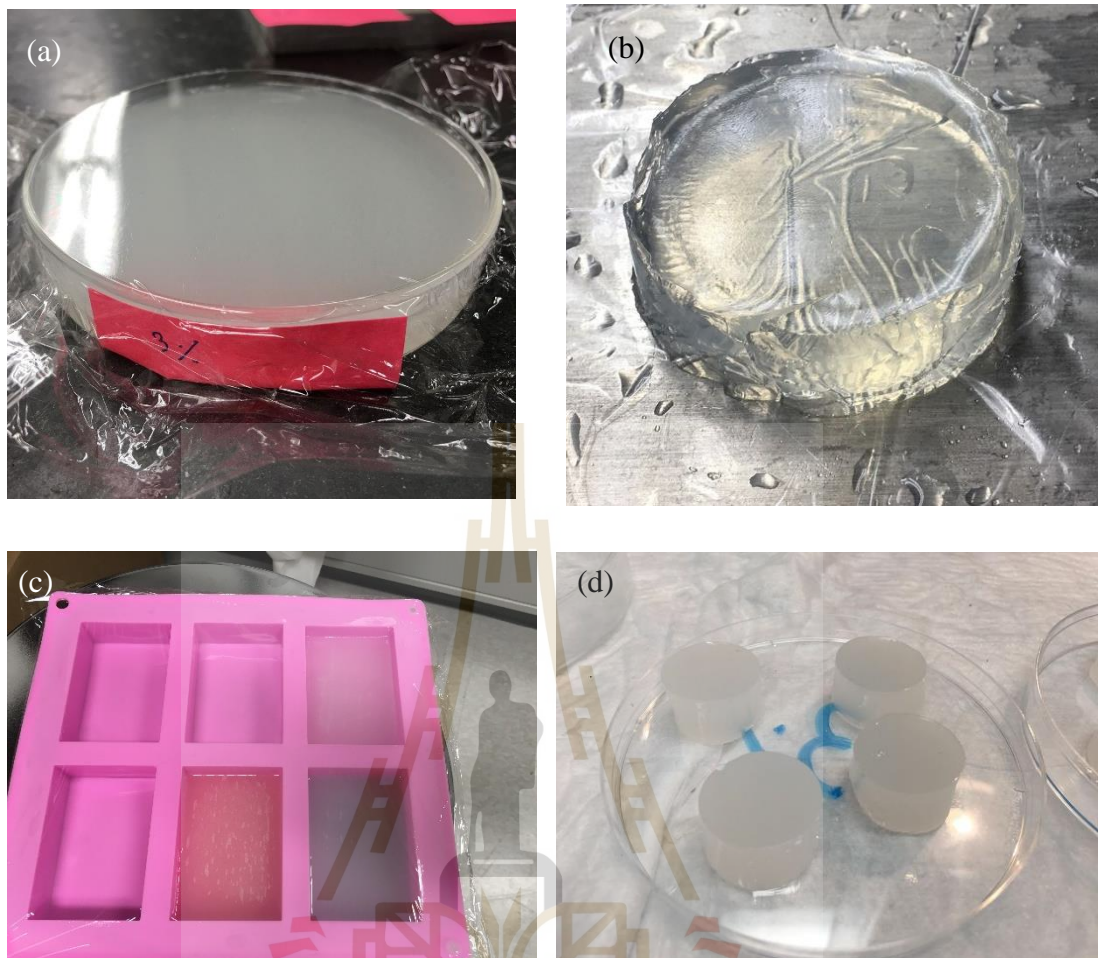


Figure 3.2 (a) Gelatin phantom with coffee cream, and (b) without coffee cream.
 (c) Gelatin solution on the silicone mold covered with plastic wrap.
 (d) Cylindrical shapes of gelatin phantom for standard measurements.

Two gelatin configurations were prepared, i.e., homogeneous and left-right representing different types of structures that might be found in real applications. For the left-right configuration, two concentrations of gelatin were separately prepared. Then, the hot wire cutter was used to create a sharp edge on each gelatin and attached them as shown in figure 3.3

Homogeneous

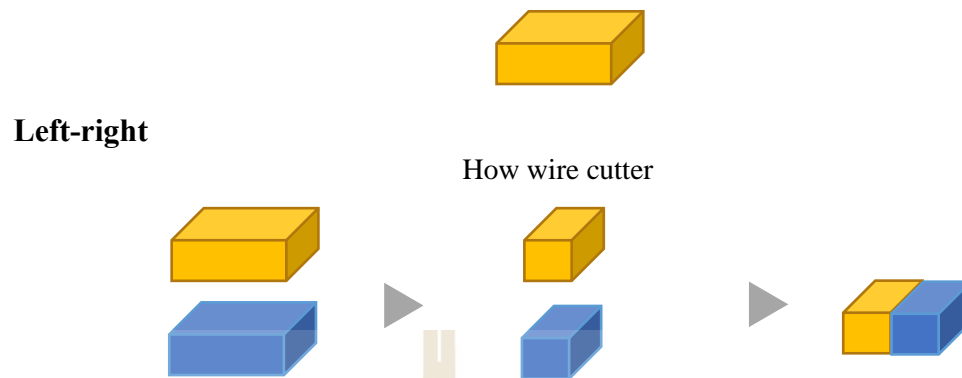


Figure 3.3 The process of gelatin preparation of homogeneous and left-right configurations.

3.2 Experimental setup

The experimental setup consists of two main parts. The first part is a custom-developed frequency-domain phase-sensitive OCT (PhS-OCT) to detect the occurred motion on the sample through Doppler phase shift. The second part is an external excitation to introduce a shear vibrational wave on the sample. The schematic of our developed PhS-OCT is shown in figure 3.4. The light source is a broadband frequency swept laser (HSL-2100-WR, Santec, Aichi, Japan) with 1,318 nm center wavelength and 125 nm spectral bandwidth. The light source (yellow arrow) was split into two paths (50:50 power ratio) by a 2×2 fiber coupler. In the first path, i.e., the sample arm, the 2-axis galvanometer mirrors, and the objective lens were used for lateral scanning on the sample. Back-scattered light from the sample was collected with the same objective lens and coupled back into a fiber coupler (green arrow). Another path of light propagated along the reference arm, incident on a plane mirror (blue arrow), and then reflected back to the fiber coupler (red arrow). The optical path difference (OPD) between two paths

caused the interference that was captured by the photodetector at a 20 kHz sampling rate. The lateral resolution of our system was approximately $20\ \mu\text{m}$ as quantified by using a resolution target. The axial resolution was approximately $10\ \mu\text{m}$ as measured from the full width at half maximum (FWHM) of the axial profile of a perfect plane mirror. The data acquisitions were collected and controlled by LabView software (National Instruments, Austin, TX, United States).

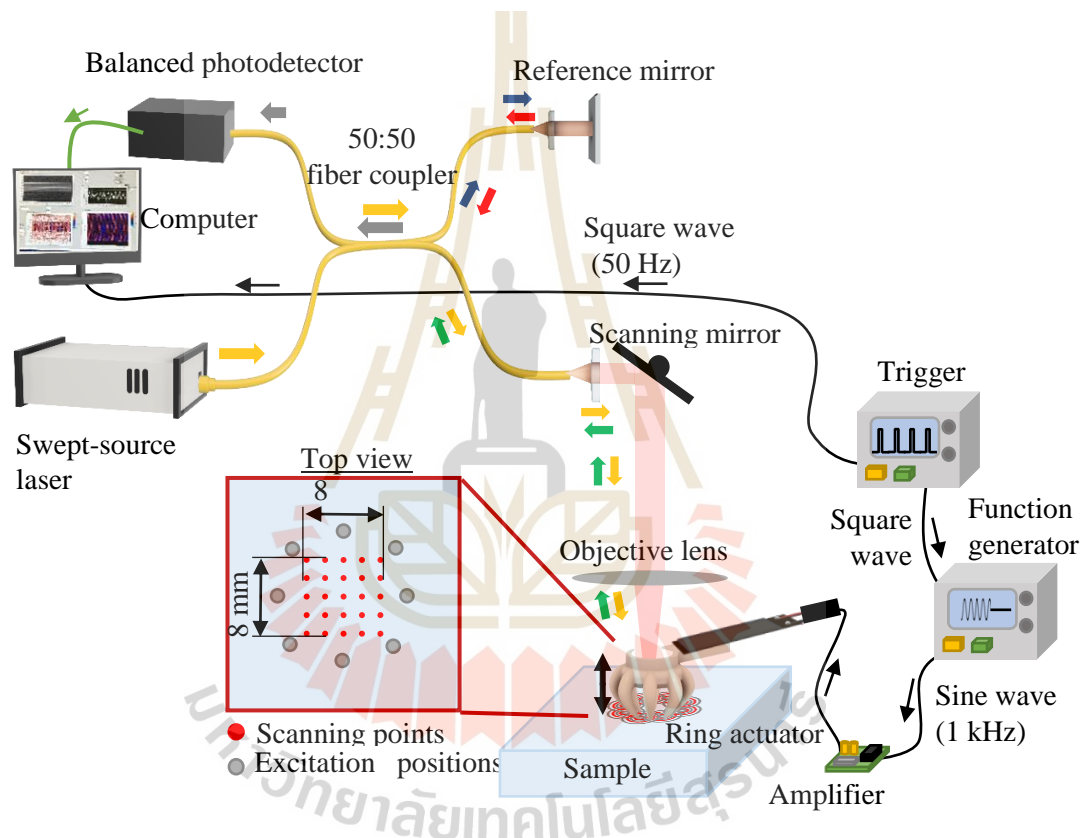
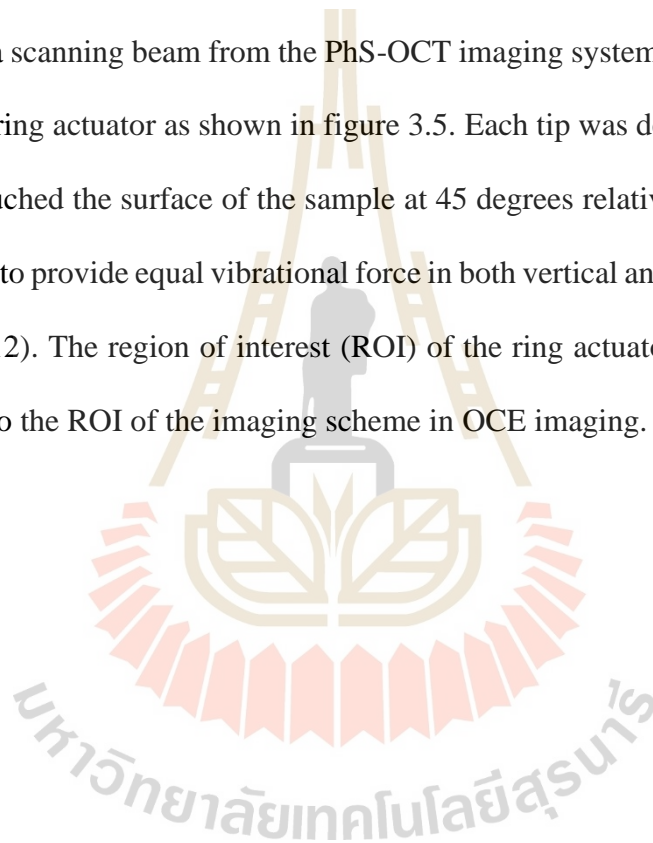


Figure 3.4 Schematic diagram of an experimental setup of the PhS-OCT, external synchronization (trigger), and external excitation using a 3D printed ring actuator attached to single piezoelectric actuator.

The excitation scheme consists of a function generator (AFG320, Textronix, Beaverton, OR, United States), a piezoelectric bimorph actuator (BA450, PiezoDrive,

Callaghan, NSW, Australia), and a signal amplifier (PDU150, PiezoDrive, Callaghan, NSW, Australia). According to the reverberant shear wave field concept, multiple sources of vibrations are required. The 3D-printed of ring-shaped ABS plastic with eight tips, called the “ring actuator” was designed in Fusion360 (Autodesk, San Rafael, California, United States). The ring actuator was fabricated and attached to the piezoelectric actuator to simulate eight vibration sources on the sample’s surface while allowing for a scanning beam from the PhS-OCT imaging system to pass through at the center of the ring actuator as shown in figure 3.5. Each tip was designed to be a curved shape that touched the surface of the sample at 45 degrees relative to the surface plane of the sample to provide equal vibrational force in both vertical and horizontal directions (Li et al., 2012). The region of interest (ROI) of the ring actuator is $8 \times 8 \text{ mm}^2$, which corresponds to the ROI of the imaging scheme in OCE imaging.



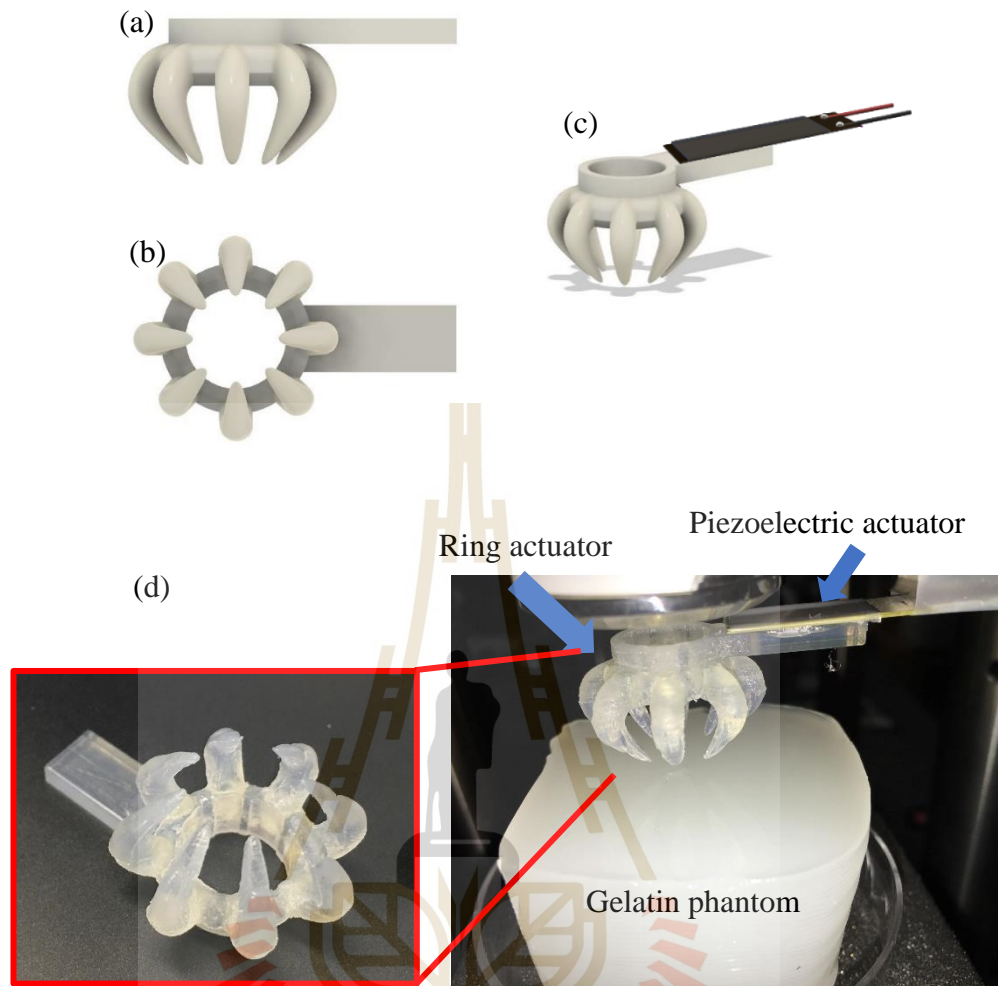


Figure 3.5 Ring actuator model, (a) side view, (b) bottom view (c) 3D view with piezoelectric actuator. (d) Ring actuator was used in the experiment.

In our experiments, both imaging and excitation systems were synchronized via another function generator with 50 Hz and 50% duty cycle of pulse square wave. Thus, the data acquisition time per lateral position was 20 milliseconds. The excitation frequency of 1 kHz was used in our experiment over the ROI of $8 \times 8 \text{ mm}^2$, which is suitable for entire wave observation. Higher frequency, i.e., 2 kHz can operate as well, but the faster the shear wave, the more attenuation on the magnitude of the wave. During 20 ms, the function generator sent a burst mode (19 cycles) of 1 kHz of the sinusoidal

wave into the piezoelectric actuator through the amplifier. The time interval of 1 cycle of 1 kHz sine wave is 1 ms, 19 cycles of 1 kHz of sine wave corresponded with 19 ms. 1 ms was left for data transfer time. At each lateral position in the detection scheme, the M-mode data acquisition, i.e., acquiring multiple axial profiles over time for 100 depth profile (A-scan), was performed while the surface was disturbed in that 20 ms interval by the ring actuator. The process was repeated for all lateral positions over the ROI of the sample as shown in the timing diagram in figure 3.6(a) and scanning positions (figure 3.7).



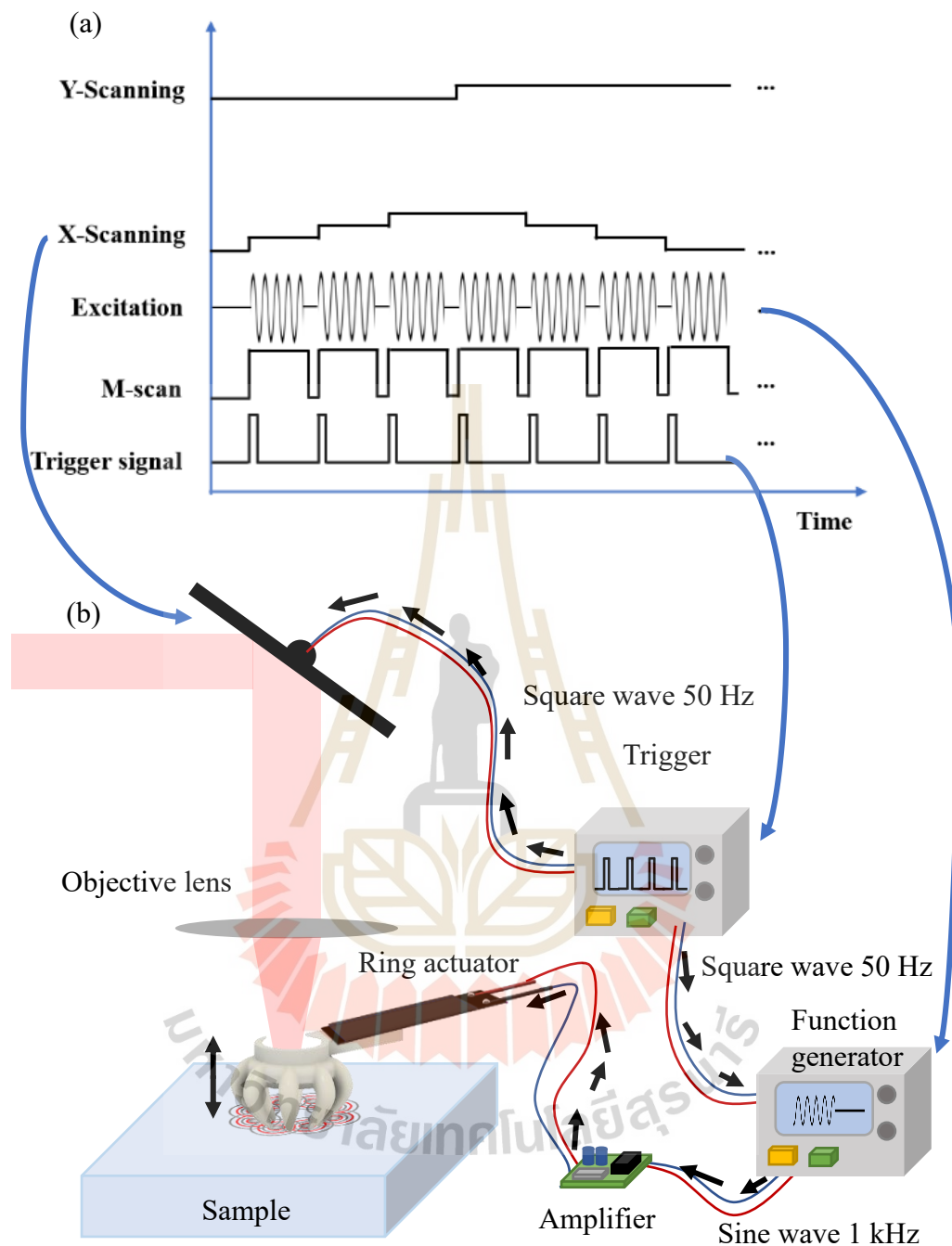


Figure 3.6 (a) Time axis of all devices to synchronization. (b) Excitation scheme and scanning mirror synchronization by a single trigger.

The vertical displacement was captured over 100×100 lateral positions in xy -plane and saved all raw data in .tif file format. According to 10,000 positions of lateral scanning (100 on x -axis, 100 on y -axis), the zig-zag scanning pattern was operated on

OCE imaging as shown in figure 3.7, to reduce the time for repositioning the scanning mirror, as well as to prevent the quick response from an input voltage of the scanning mirror that might damage the hardware. The zig-zag correction was done by sorting data backward in an even row of 100 lateral scans (x -axis).

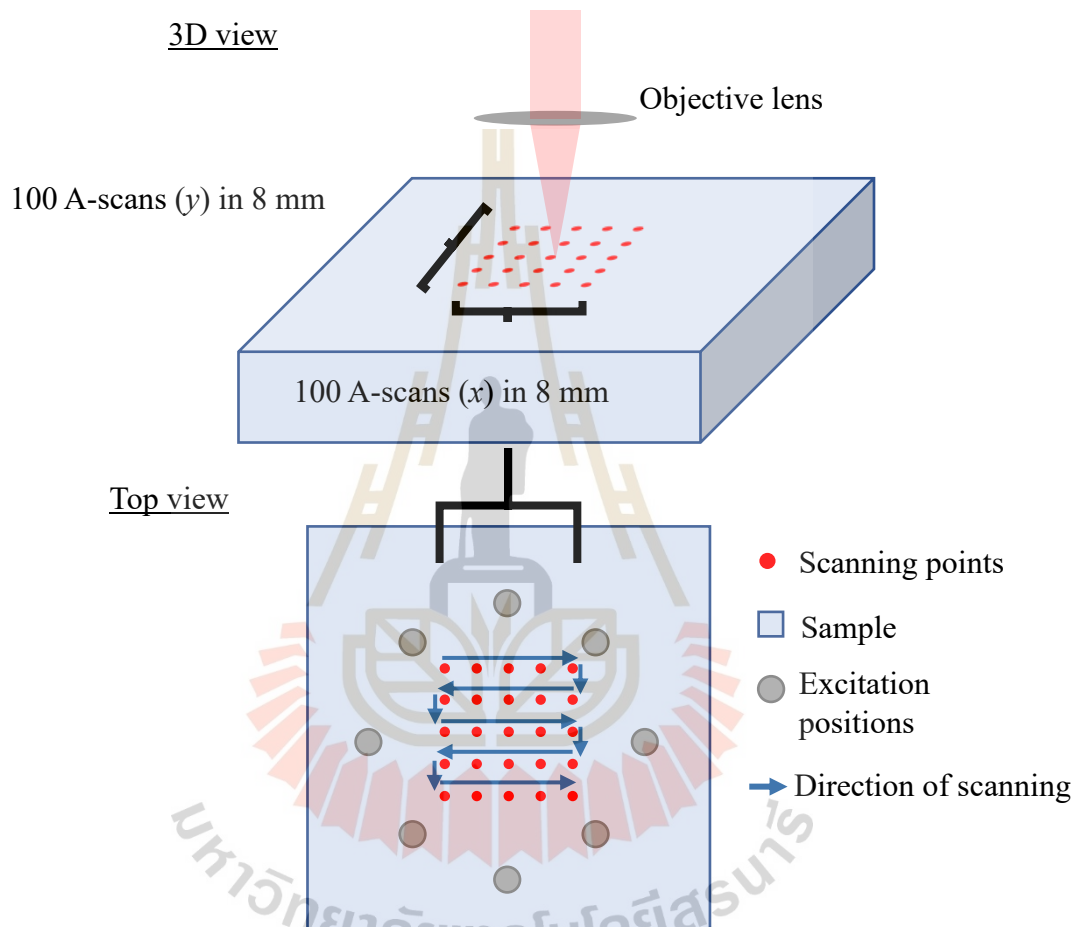


Figure 3.7 The zig-zag scanning pattern was operated on OCE imaging to reduce the acquisition time.

The data from the detection scheme were sorted as a graphic explanation in figure 3.8. At each position, 100 M-mode scans were performed and stored as one .tif file. Different color of M-mode with numbering order represents the time frame of each detection (0.2 ms step). Each M-mode consisted of $1 \times 2,000$ pixels, which is the

spectral interference signal recorded in 8-bit (0-255 grayscale). After repeating the process for 100×100 spatial positions across the xy -plane, the total raw data called “the pool” was obtained, which is the 3D data over time. From this aspect, the cross-section (both vertical and horizontal) or even 3D images at any time frame can be obtained from the pool depending on the desired plane to display and the desired time frame. One gelatin sample took about 4-5 minutes. All the files were named and saved in a hard drive disk, which consumes about 16 Gigabytes (Gb) per sample.

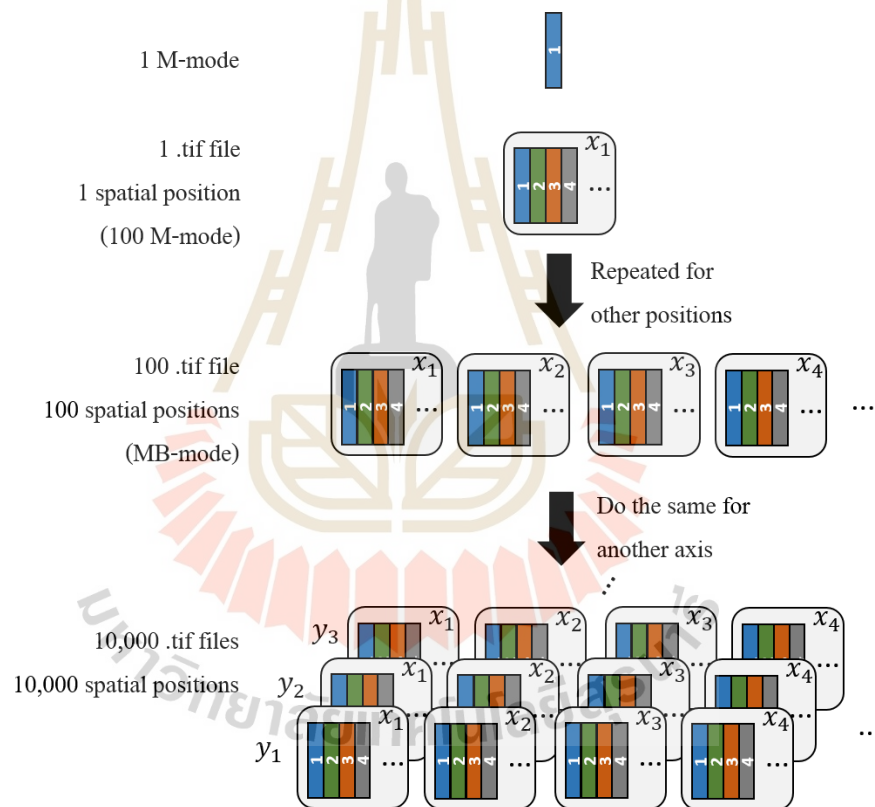
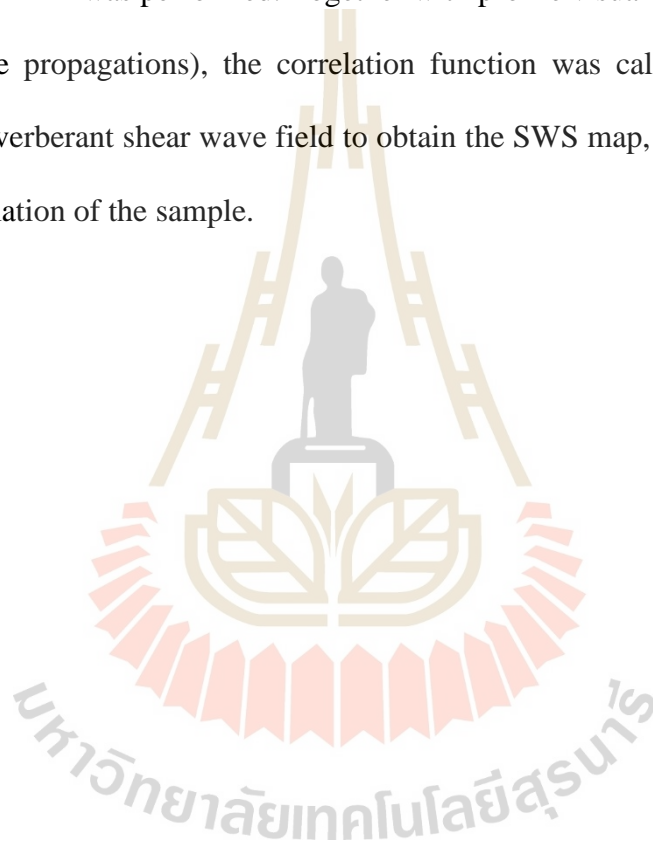


Figure 3.8 Graphical explanation of raw data in the detection scheme. Single detection creates 1 M-mode ($1 \times 2,000$ pixels), continuing to collect until 100 M-mode, then become one spatial position (one .tif file). Repeat the process to gather a hundred spatial positions (one MB-mode), and do the same process for another axis. Total raw data is called “the pool”, which is capable to retrieve any plane and time frame.

3.3 Data analysis

All data were imported into MATLAB™ (MathWorks, Massachusetts, United States) for further analysis. Figure 3.9 shows the flowchart of data analysis to obtain the SWS map. Starting with importing the raw data, the axis definition must be the same as the ROI in OCE imaging. Further analysis by calculating the phase shift by using Loupas's algorithm was performed. Together with profile visualizations (e.g., B-mode, *en-face*, wave propagations), the correlation function was calculated following the concept of reverberant shear wave field to obtain the SWS map, which is linked to the elastic information of the sample.



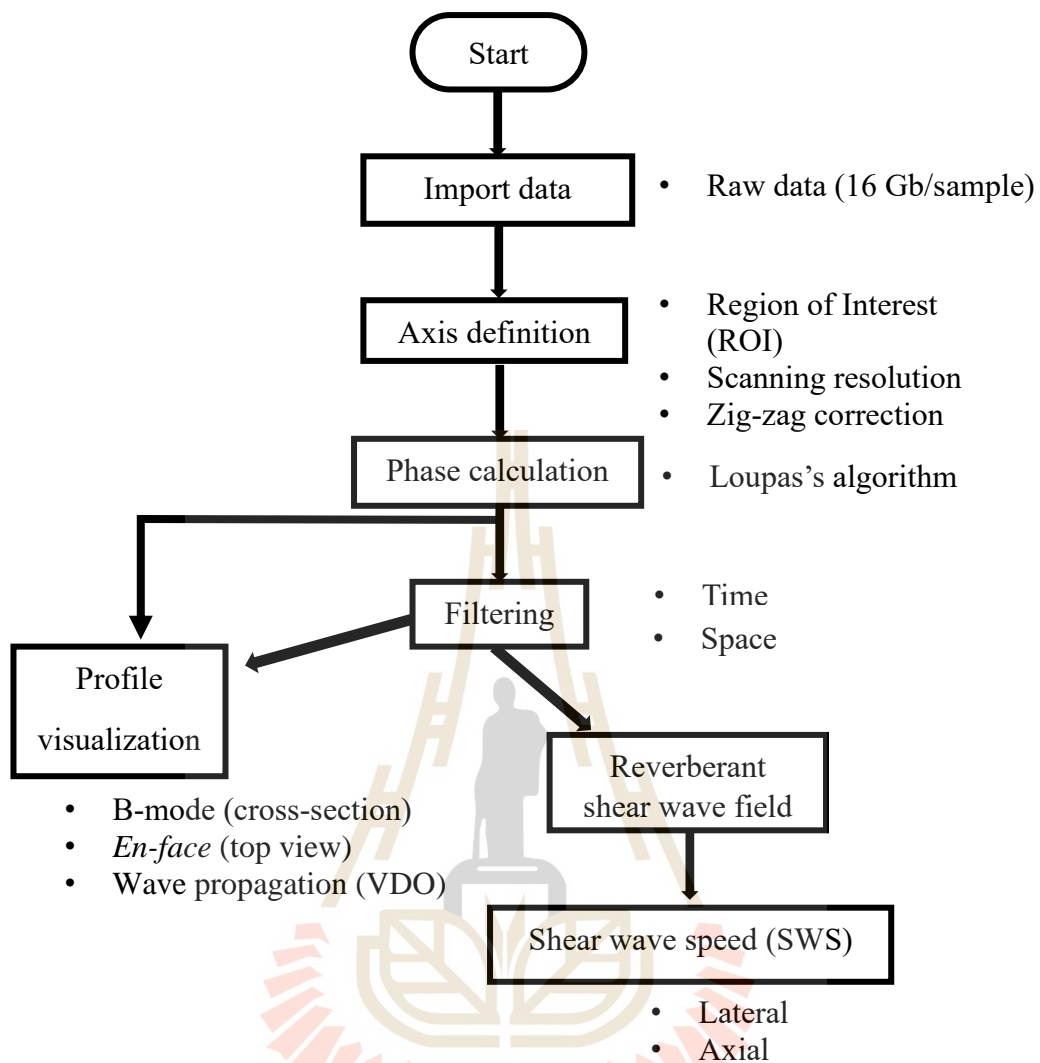


Figure 3.9 Flowchart of data analysis to obtain the shear wave speed (SWS) map, all processes were done in MATLAB™ software.

The data processing began with axis definition according to the ROI of OCE as $8 \times 8 \text{ mm}^2$ with 100×100 spatial scanning points, The axial resolution was $10 \text{ }\mu\text{m}$ as determined by the bandwidth and the center wavelength of the light source.

To obtain the surface displacement, the phase shift related to the displacement was determined by using the equation 2.68. The typical method to determine the phase

shift is by computing the amount of Doppler phase shift. By considering two consecutive signals as equation 2.9 with the time involved as

$$I(z, t_0) = |I(z, t_0)| \exp(j\phi(z, t_0)), \quad (3.1)$$

$$I(z, t_1) = |I(z, t_1)| \exp(j\phi(z, t_1)), \quad (3.2)$$

where $|I|$ is the magnitude of the signal, ϕ is the phase of the signal at the time t_0 and t_1 . The amount of phase shift can be computed by

$$\Delta\phi(z) = \arctan \left\{ \frac{\text{Im}[I(z, t_1)I(z, t_0)^*]}{\text{Re}[I(z, t_1)I(z, t_0)^*]} \right\}, \quad (3.3)$$

where I^* is the complex conjugate of the signal, and $\text{Re}[]$ and $\text{Im}[]$ are the real part and imaginary part respectively.

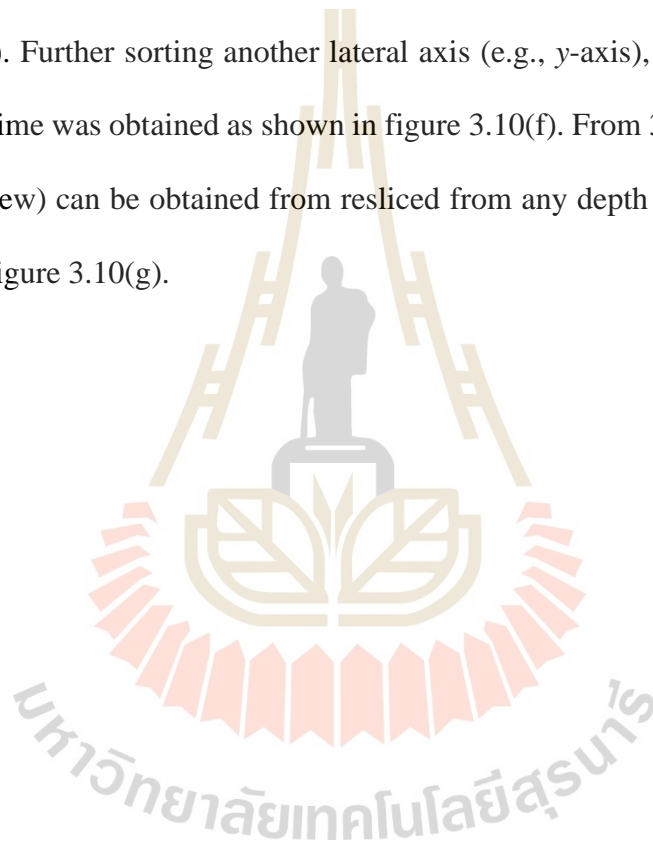
However, this method is sensitive to noise. An alternative method to reduce noise is demanded. We chose Loupas's algorithm to estimate the displacement as follows (Zvietcovich et al., 2017),

$$\Delta\phi(z) = \frac{\arctan \left\{ \frac{\sum_{m=0}^{M-1} [\text{Im}(z_m, t_0) \text{Re}(z_m, t_1) - \text{Re}(z_m, t_0) \text{Im}(z_m, t_1)]}{\sum_{m=0}^{M-1} [\text{Re}(z_m, t_0) \text{Re}(z_m, t_1) - \text{Im}(z_m, t_0) \text{Im}(z_m, t_1)]} \right\}}{1 + \frac{\arctan \left\{ \frac{\sum_{m=0}^{M-2} \sum_{n=0}^1 [\text{Im}(z_m, t_n) \text{Re}(z_{m+1}, t_n) - \text{Re}(z_m, t_n) \text{Im}(z_{m+1}, t_n)]}{\sum_{m=0}^{M-2} \sum_{n=0}^1 [\text{Re}(z_m, t_n) \text{Re}(z_{m+1}, t_n) - \text{Im}(z_m, t_n) \text{Im}(z_{m+1}, t_n)]} \right\}}{2\pi}}, \quad (3.4)$$

where M is window size for calculation.

For the profile visualization, Figure 3.10(a) shows the frame of spectra of a spatial location (one .tif file), which consists of 100 M-mode (vertical red frame) by 2,000 pixels. Each line spectrum (figure 3.10(b)) will be processed following the OCT

imaging as described in section 2.2.4. In OCE imaging, the image of M-mode i.e., displays the depth profile of one position over time (motion-captured over 100 times of acquisition) is obtained instead of B-mode (cross-section of the sample) as shown in figures 3.10(c). The M-mode of many lateral positions (e.g., x -axis) were sorted as shown in figure 3.10(d) called MB-mode, the B-mode or cross-section image of the sample can be obtained by resliced the MB-mode in the lateral direction as shown in figure 3.10(e). Further sorting another lateral axis (e.g., y -axis), the 3D volume of the sample over time was obtained as shown in figure 3.10(f). From 3D volume, an *en-face* image (top view) can be obtained from resliced from any depth position and any time as shown in figure 3.10(g).



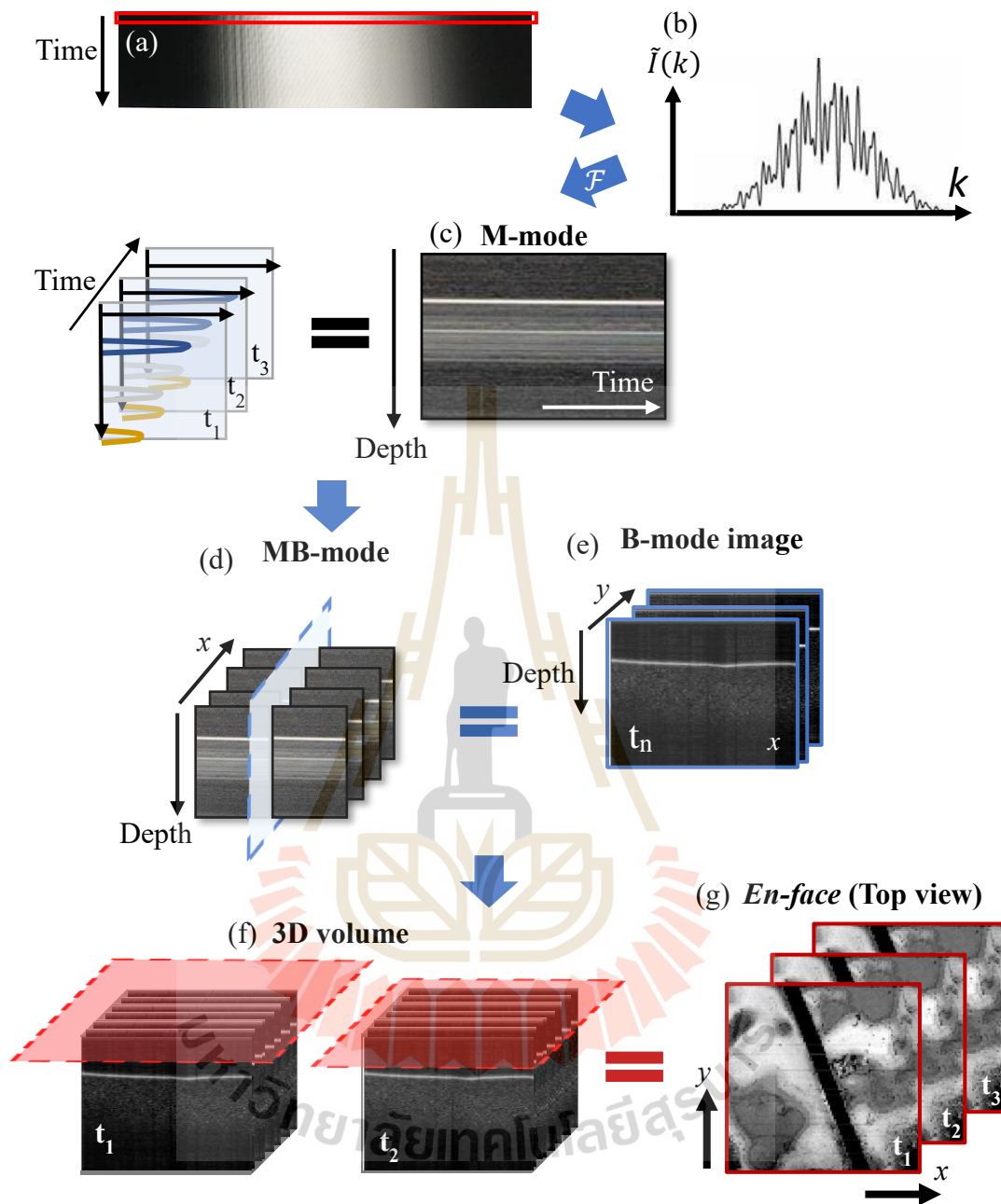


Figure 3.10 The flowchart shows the image processing. (a) Spectra frame (2048 pixel by 100 M-mode). (b) Example of an interference signal from a line spectrum in (a). (c) M-mode image from all lines in (a). (d) MB-mode from 1D lateral scanning. (e) B-mode image obtained by resliced MB-mode. (f) Scanning another lateral axis to obtain the 3D volume. (g) The *en-face* (top view) can be obtained from resliced any depth position.

Figure 3.11 describes the process to obtain the local SWS map via the concept of the reverberant shear wave field. The phase shift map was computed by using Loupas's algorithm. The phase shift data was divided into small windows and then calculated the local 2D-autocorrelation (figure 3.11(b)). The autocorrelation map was radial averaged (figure 3.11(c)) over 180 degrees. The averaged data was fit with equation 2.66 to approximate the wavenumber, k as shown in figure 3.11(d). The relationship of phase velocity (equation 2.67) was used to map the local speed of the shear wave, which represents the local elastic information of the sample as shown in figure 3.11(e).

A small window in the phase shift map means a few phase data were used to calculate in the autocorrelation process, and all the data in that window will become a single local SWS result. In addition, a larger window causes less elasticity resolution and increases the processing time. Therefore, we studied how the size of data used in the calculation affects the local SWS result via the concept of the reverberant shear wave field to obtain the minimum size of the correlation window and high elastic resolution in the SWS map. The results were then compared with the standard mechanical testing for each gelatin concentration.

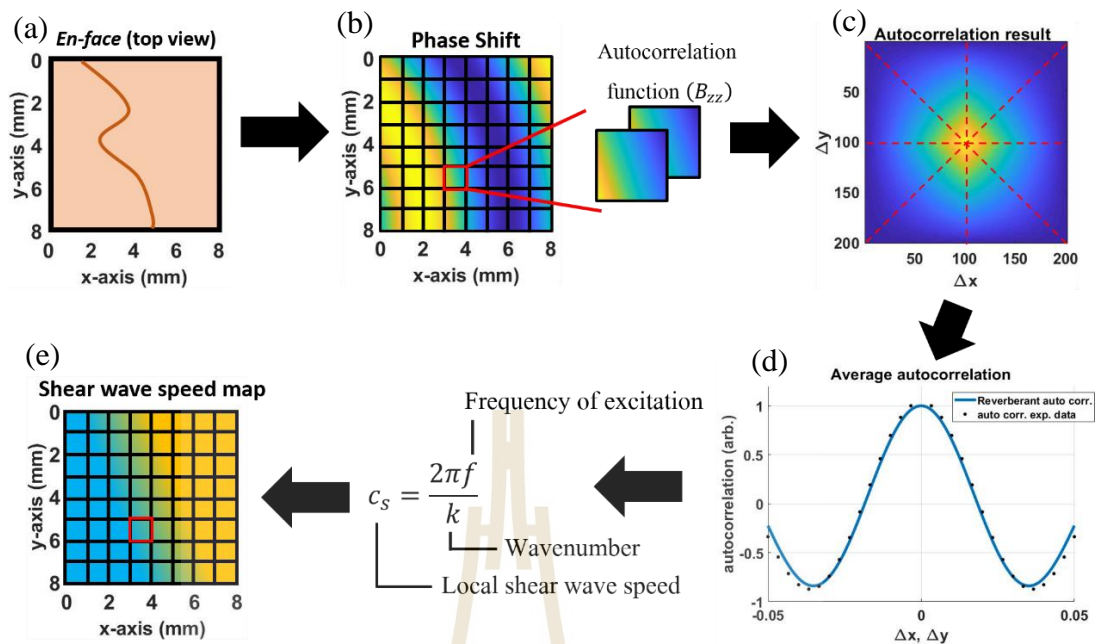


Figure 3.11 Analysis process for the local shear wave speed (SWS) map. (a) Example of *En-face* (Top view) image of the gelatin phantom. (b) the phase shift data collected from Loupas's algorithm and divided into small windows for the 2D-autocorrelation following the concept of reverberant shear wave field. (c) Autocorrelation result and radial averaging (red dash line) for curve fitting. (d) The radial average the autocorrelation (black dot) and the wavenumber was obtained by determining k from curve fitting (blue line). (e) Local shear wave speed (SWS) map is determined from the phase velocity relation (equation 2.67).

CHAPTER IV

RESULTS AND DISCUSSIONS

In this chapter, we described the experimental results of the combinations of our PhS-OCT and the concept of the reverberant shear wave field for imaging and differentiating the tissue-mimicking gelatin phantoms. To verify the performance, the 3 wt% and 4 wt% concentrations were prepared following the process in chapter III with various configurations (homogeneous, left-right) for the experiment. In the analysis process, the propagated shear wave was observed and processed to obtain the elasticity of the sample, which is expressed by the shear wave speed (SWS) map as described in section 2.3.1.

4.1 Phantom preparation issues

In the gelatin phantom preparations, the gelatin phantoms were prepared by using the silicone mold (figure 4.1(a)) and covered by plastic wrap to avoid some dust falling in. We have encountered the steam condensation at the inner side of the plastic wrap that causes the top surface of the phantom to have more roughness and be covered by water, the bottom side (contact with the silicone mold) was used instead in the experiments. The 3 wt% concentration phantom was damaged after trying to remove out from the silicone mold as shown in figure 4.1(b). Then, we used the lubricant (WD-40, San Diego, California, United States) sprayed over the silicone mold before pouring the gelatin solution to prevent the gelatin stuck with the mold. However, many small holes

were found on the surface (bottom side) of the phantom as shown in figure 4.2. It might be caused by a small silicone particle in the lubricant oil. To solve these issues, the gelatin preparations were fabricated with the glass Petri dishes (figure 4.3), food containers were used instead of silicone mold, the gelatin solutions were not covered by plastic wrap anymore, also left the solution on the table instead of in the refrigerator (the room temperature is about 22 degrees Celsius) for reducing the small air bubble stuck in the gelatin solution caused by rapid gelatinization.

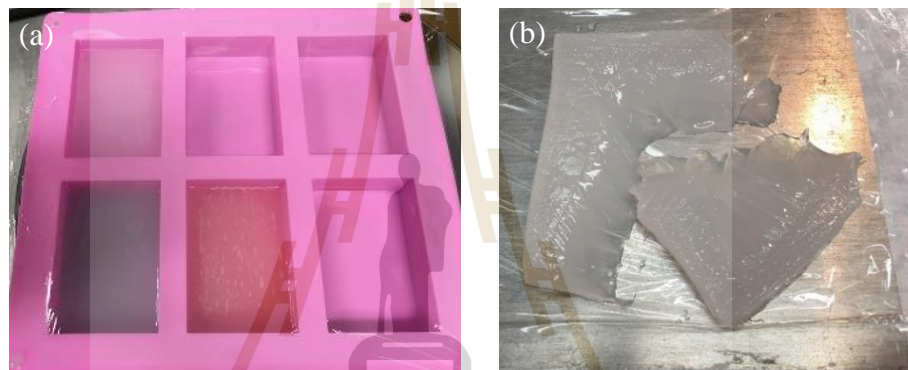


Figure 4.1 (a) The silicon mold with gelatin solutions and plastic wrap.

(b) Damaged gelatin phantom when trying to remove from the mold.



Figure 4.2 Small holes were found on the bottom surface of the gelatin phantom when taken out from the silicone mold with lubricant oil.



Figure 4.3 Gelatin phantom of 3 wt% and 4 wt% with plastic wrap inside at the bottom of the Petri dish for easy removal (top surface was used for experiment).

For the left-right configuration, the two different concentrations of gelatin were placed side by side (L4R3) as shown in figure 4.4. Both 3 wt% and 4 wt% were separately prepared, then attached together. Figure 4.4(c) shows the merged color at the

interface of the phantom caused by the concentration diffusion that might affect the SWS results.

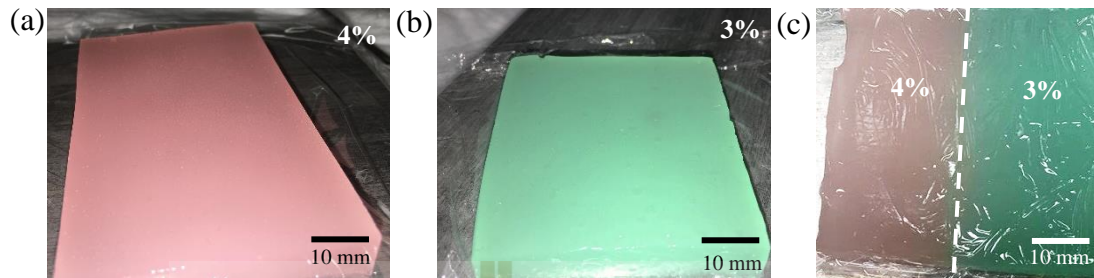


Figure 4.4 Photograph of the gelatin phantom of (a) homogeneous 4 wt% concentration, (b) homogeneous 3 wt% concentration, and (c) the left-right configuration.

4.2 Image processing and filtering

According to the flowchart in figure 3.9, the B-mode and *en-face* images can be obtained from the real part of OCT signal, by re-slicing the M-mode (movement of a certain position over time) image along with a lateral position (x -axis) and top view (xy plane), respectively. Figure 4.5 shows the B-mode and *en-face* images of 3 wt% and 4 wt% gelatin phantoms. The B-mode image shows the cross-section of the air (0-0.5 mm) and gelatin (below 0.5 mm), the bright line (approximately at 0.5 mm) represents the top surface of the gelatin phantom caused by strong reflection when the incident light propagates through the different medium (air-gelatin interface) and reflection from the gelatin medium caused by the coffee cream that mixed in the gelatin solution. The *en-face* image shows the top view of the gelatin phantom over $8 \times 8 \text{ mm}^2$. The dark region is the instability of smoothness that occurred on the surface, and darker regions at all corners of the *en-face* images are caused by the end of the ring actuator that is placed on the surface of the gelatin phantom.

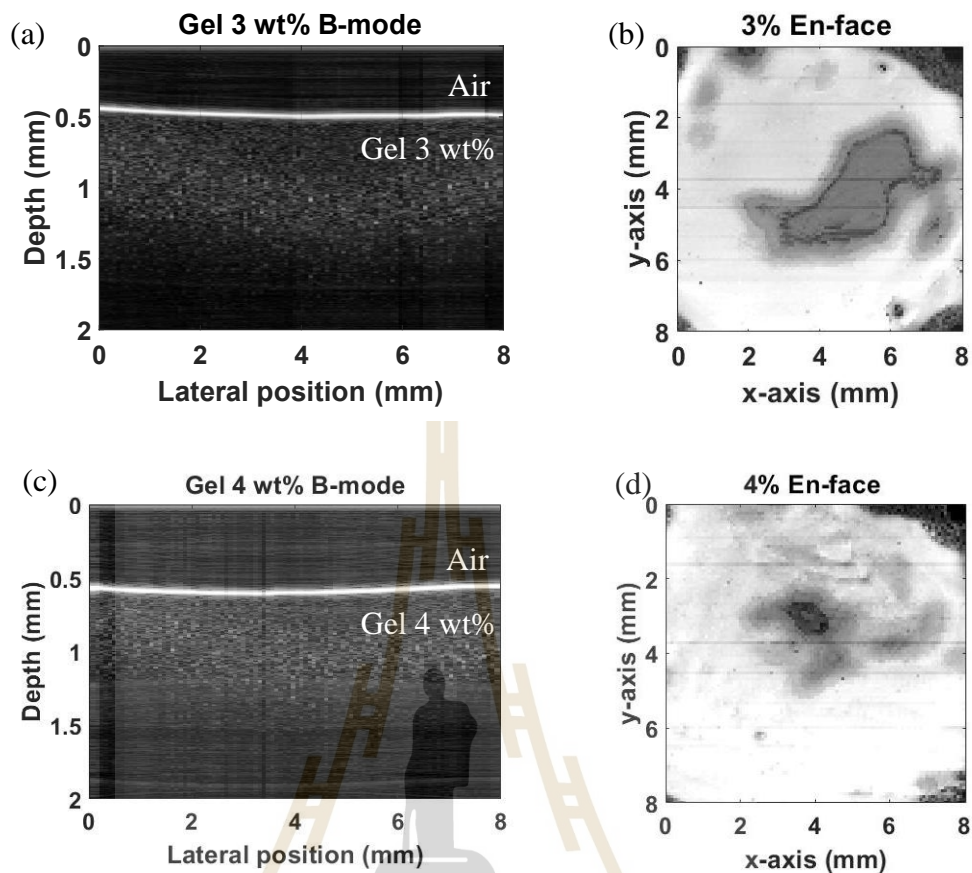


Figure 4.5 (a), (c) B-mode images of 3 wt% and 4 wt% gelatin phantoms, respectively.

Bright-line describes the cross-section structure of the air-gelatin interface.

(b), (d) *En-face* images of 3 wt% and 4 wt% gelatin phantoms, respectively.

Dark regions represent the instability of the surface's smoothness, darker regions are caused by the end of the ring actuator.

There are indistinguishable B-mode images in figure 4.5(a) and figure 4.5(c). However, B-mode images still have not expressed the shear wave propagation yet. To obtain the wave propagation information, Loupas's algorithm (Loupas et al., 1995; Zvietcovich et al., 2017) was used as follows equation 3.4, and the results were shown in figure 4.6. The local phase shift was displayed as yellow (positive phase shift) and

blue (negative phase shift) colormap corresponded to longer and shorter OPL in the sample arm of the imaging system, respectively.

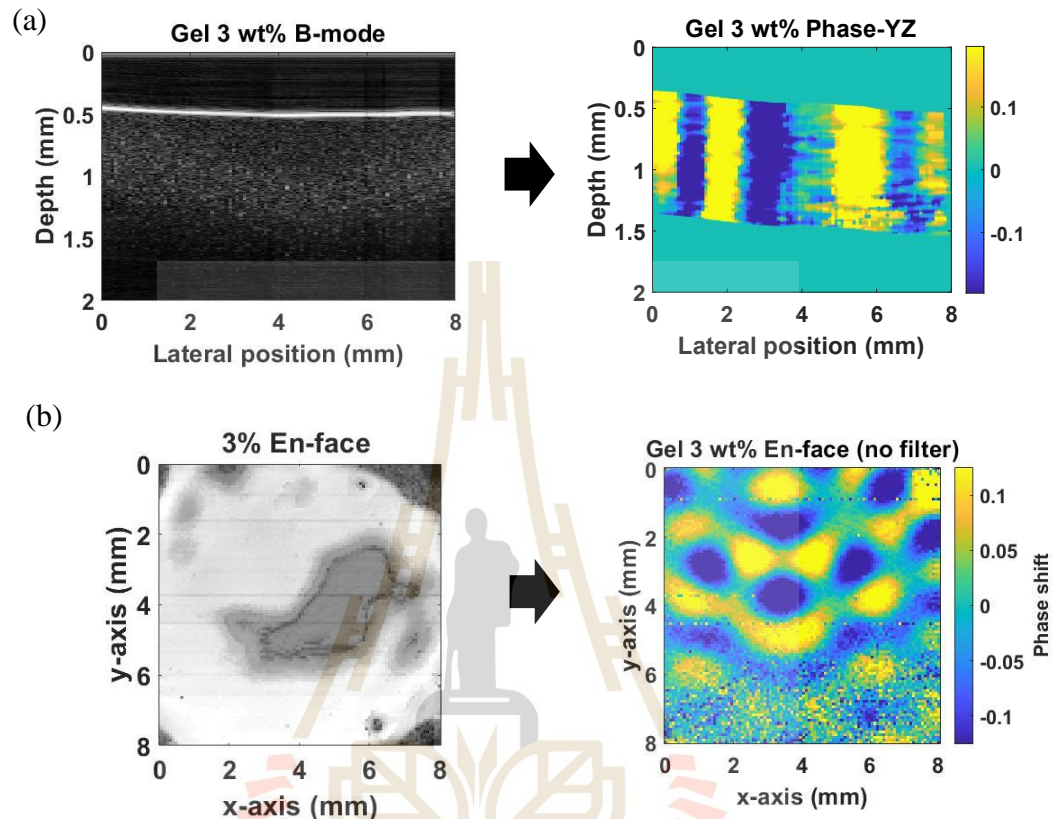


Figure 4.6 The local phase shift information using Loupas's algorithm of (a) B-mode and (b) *en-face* images of 3 wt% gelatin phantom.

After noise reduction via Loupas's algorithm, other kinds of noises still existed.

Two types of data filtering were conducted to reduce the noise, i.e., temporal and spatial filtering. The process of temporal filtering is shown in figure 4.7, by looking at some lateral positions in the phase shift data over time (figure 4.7(a)), taking the Fourier transformation to see the data in the frequency domain, then using the band-pass filter to keep the desired frequency that applied on the sample (1 kHz), i.e., 950 Hz to 1050 Hz of frequency range and subtract unwanted frequency out as shown in figure 4.7(b).

The result of the temporal filter after the inverted Fourier Transform is shown in figure 4.7(c). The spatial filter was processed after the temporal filter. By looking at all lateral positions at a certain time frame as shown in figure 4.8(a). The two-dimensional Fourier transform (2D-FT) was processed to the phase shift data, then doing band-pass filter in the frequency domain (donut shape in figure 4.8(b)). The size of the band-pass filter was fixed but still obtain a good result as shown in figure 4.8(c). Using these two filtering together with Loupas's algorithm will be more effective for noise reductions.

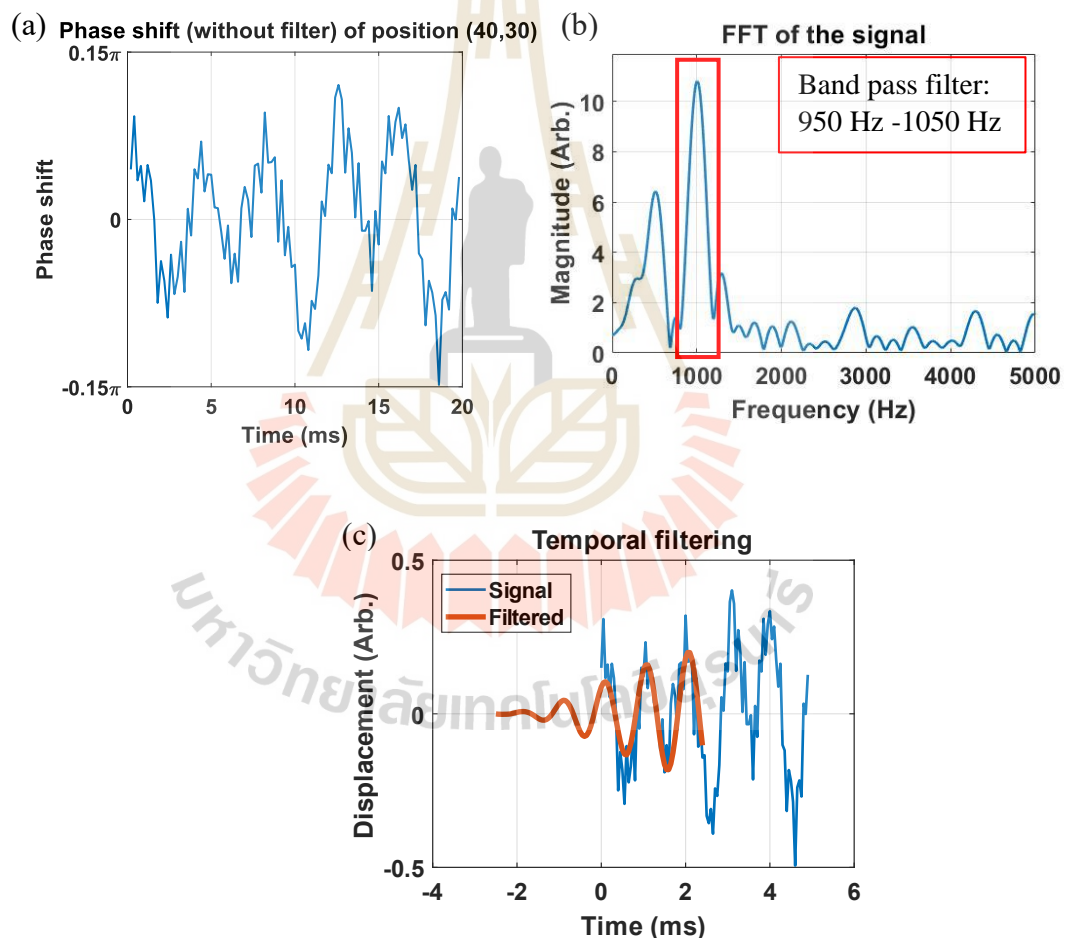


Figure 4.7 The process of temporal filtering of the phase shift data. (a) The phase data without temporal filtering. (b) Fourier Transform of (a). (c) Comparison of the filtered data (orange) and unfiltered data (blue).

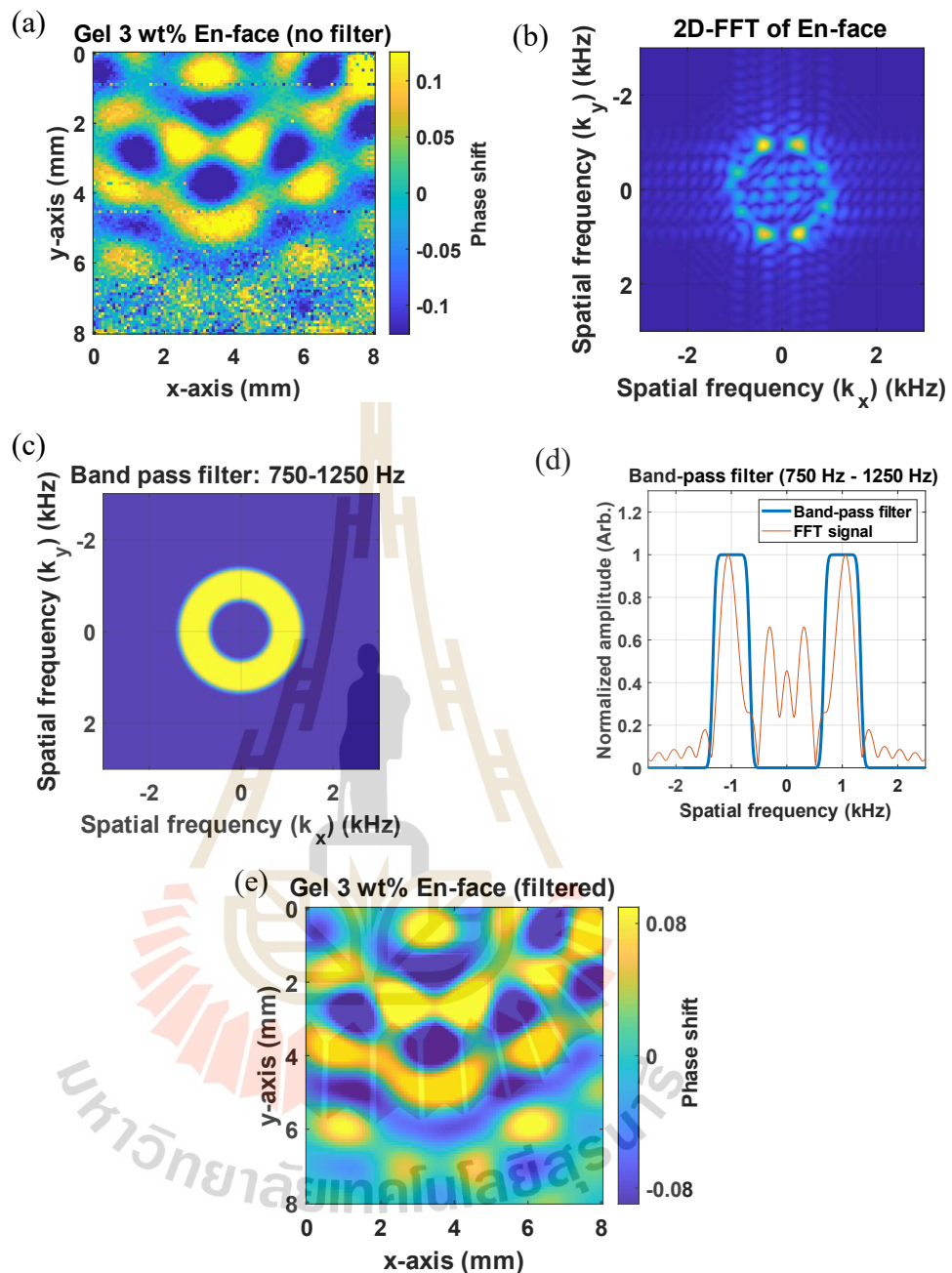


Figure 4.8 (a) *En-face* (top view) image of the phase shift data before spatial filtering. (b) Two-dimensional Fourier Transformation of (a). (c) Band-pass filter (750-1250 Hz bandwidth). (d) cross-section of (b) (orange) and band-pass filter (blue). (e) *En-face* image of the phase shift data after spatial filtering.

The VDO of the wave propagation will be available after the filtering process by sorting each phase shift data over time and displayed on the monitor. From the VDO wave propagations, the wavefront from all tips of excitation legs will approach the middle over time. The total frame of the phase shift data will be minus 1 from the total 100 M-mode acquisitions. Thus, the 99 phase shift frames were obtained in that interval of 20 ms. The shear wave propagation result on 3 wt% gelatin phantom was shown as a time sequence in figure 4.9, which slowly propagates toward the center. According to the speed of the shear wave is approximately about 1-10 m/s (Zvietcovich et al., 2017), the wavelength of the wave propagation observed in the ROI ($8 \times 8 \text{ mm}^2$) will become 1-10 mm for 1 kHz of excitation that sent to the ring actuator. Furthermore, the wavelength of shear wave on 4 wt% phantoms is larger than the wavelength on 3 wt% phantoms as shown in figure 4.10.

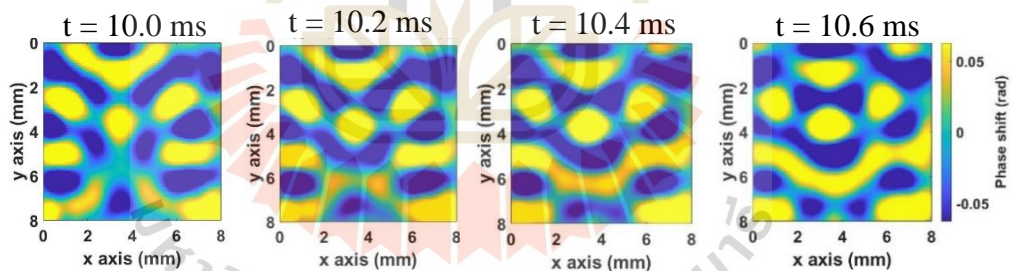


Figure 4.9 *En-face* images at different time frames show the motion of the shear wave propagating on 3 wt% gelatin phantom.

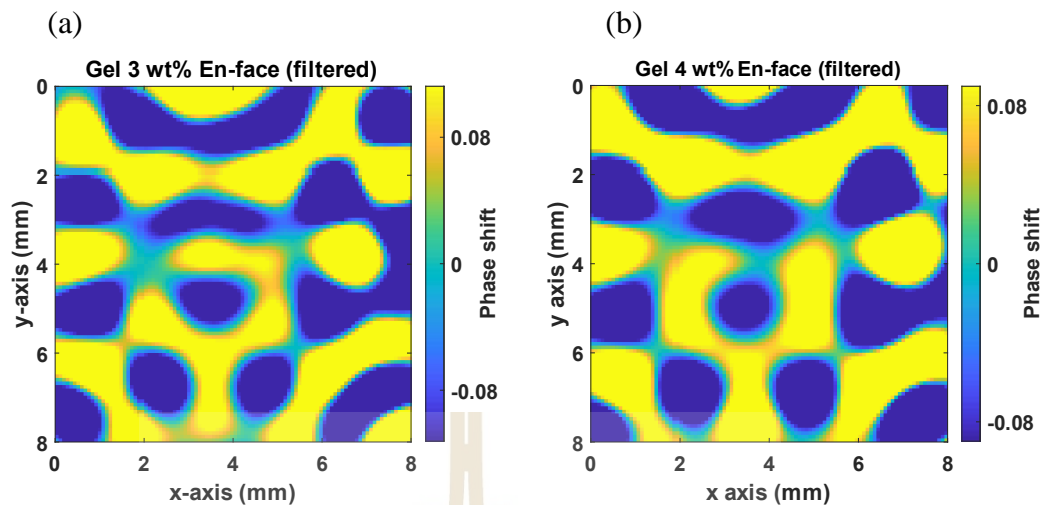


Figure 4.10 *En-face* images show the different wavelengths of shear wave propagation of (a) 3 wt% and (b) 4 wt% gelatin phantoms, in which the wavelength on the 4 wt% phantom is larger than on the 3 wt% phantom.

4.3 Window size variations

The local shear wave speed (SWS) can be obtained from the 2D-autocorrelation of the phase shift data, the resolution of the SWS map depends on the amount of phase shift data used for the calculation. i.e., only a single SWS value was obtained if all correlation windows (100×100 phase shift data) were used for the 2D-autocorrelation calculation. Thus, the SWS map will have a higher resolution with a smaller correlation window. To verify this, we varied the window size as 10×10 pixels ($0.8 \times 0.8 \text{ mm}^2$), 20×20 pixels ($1.6 \times 1.6 \text{ mm}^2$), 30×30 pixels ($2.4 \times 2.4 \text{ mm}^2$), 40×40 pixels ($3.2 \times 3.2 \text{ mm}^2$), 50×50 pixels ($4.0 \times 4.0 \text{ mm}^2$), 60×60 pixels ($4.8 \times 4.8 \text{ mm}^2$), 70×70 pixels ($5.6 \times 5.6 \text{ mm}^2$), 80×80 pixels ($6.4 \times 6.4 \text{ mm}^2$), 90×90 pixels ($7.2 \times 7.2 \text{ mm}^2$) and quantified the SWS map as shown in figure 4.11.

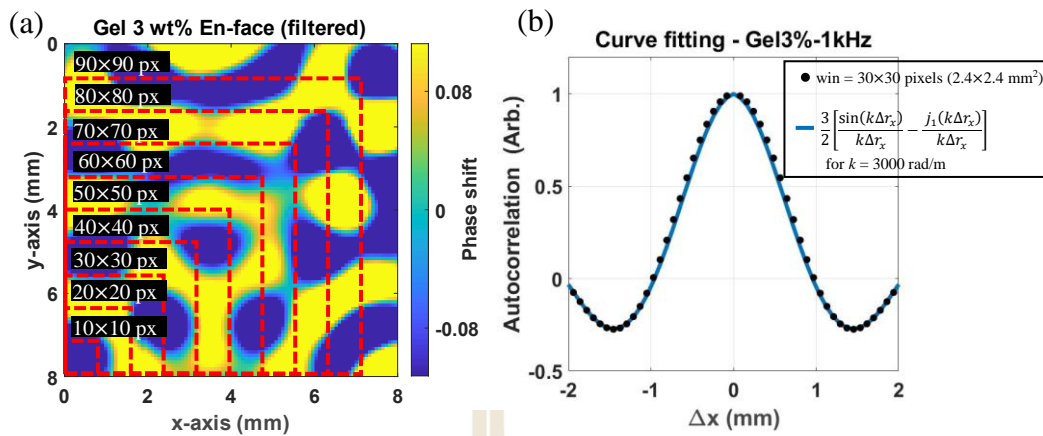


Figure 4.11 (a) The reverberant shear wave field on 3 wt% gelatin phantom with the illustration of different correlation window sizes. (b) The example of the radial average of the autocorrelation curves of 3 wt% gelatin phantom with 30×30 pixels of window size.

A local wavenumber k was determined followed equation 2.67 after doing radial average and curve fitting of the 2D-autocorrelation from data in the correlation window with tracking the first valley of the autocorrelation peak. The SWS results on 3 wt% and 4 wt% gelatin phantoms were shown in figure 4.12 and figure 4.13 respectively, the color map represents high (red) and low (blue) rates of the SWS, which is corresponded to high and low stiffness respectively followed the equation 2.27. We noticed that the resolution of the SWS map related to the correlation window size, i.e., the lower resolution obtained from a larger window size. However, some regions cannot find the valley in the curve fitting process because there is no value of the autocorrelation curve that is less than zero. Then, the fitting process shows “not a number” instead which is found in 10×10 pixels and 20×20 pixels of correlation windows. We also noticed that the SWS map with a larger correlation window size looks almost identical as shown in

figure 4.12(e) to figure 4.12(i) and figure 4.13(e) to figure 4.13(i) for 3 wt% and 4 wt% gelatin phantoms, respectively.

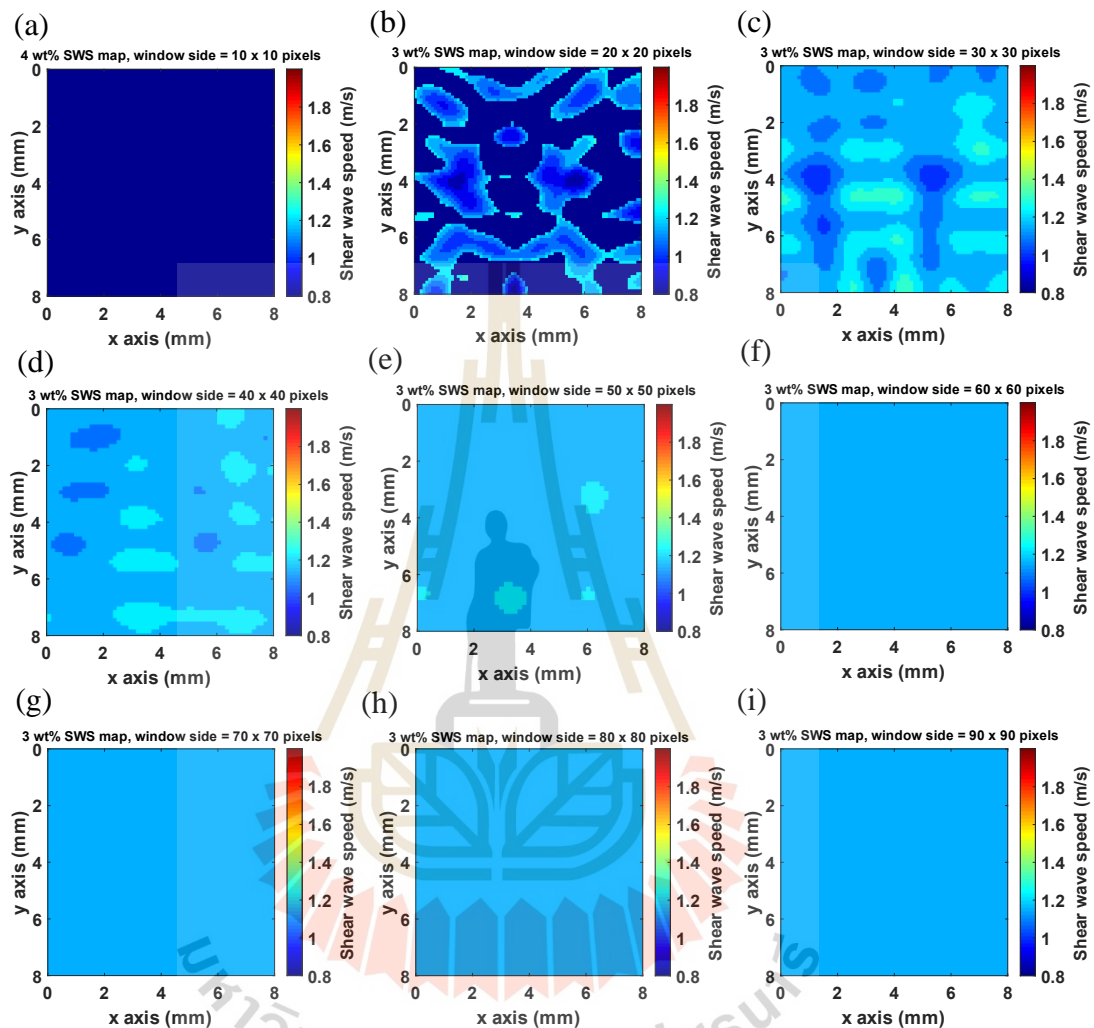


Figure 4.12 The shear wave speed (SWS) map of the 3 wt% gelatin phantom with the 1 kHz of excitation, by varying the correlation window sizes of (a) 10×10 pixels, (b) 20×20 pixels, (c) 30×30 pixels, (d) 40×40 pixels, (e) 50×50 pixels, (f) 60×60 pixels, (g) 70×70 pixels, (h) 80×80 pixels, and (i) 90×90 pixels. There are look almost identical for larger window (from (d) to (i)), but less data in curve fitting process causes discrete value of SWS in (a) and (b) as display in dark blue color.

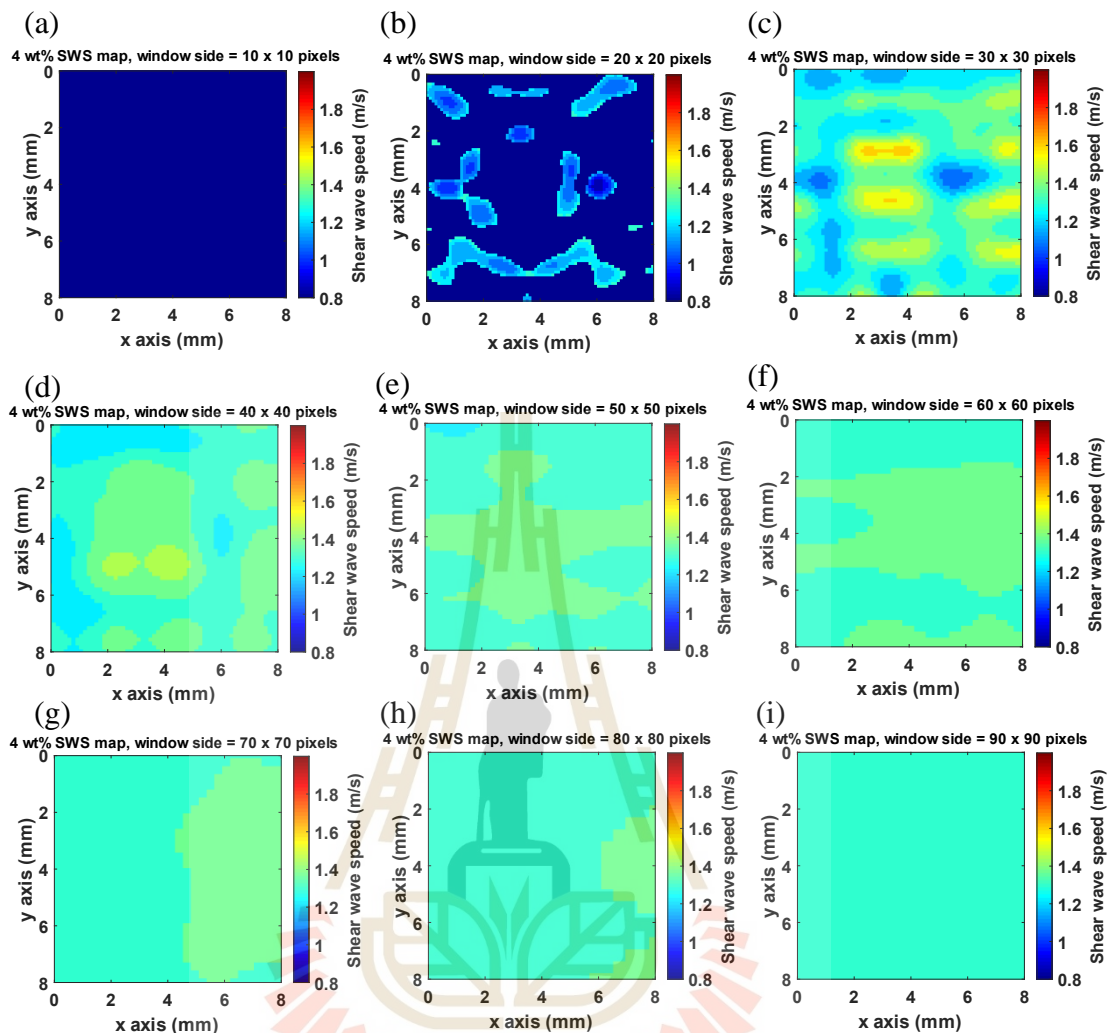


Figure 4.13 The shear wave speed (SWS) map of 4 wt% gelatin phantom with 1 kHz of excitation, by varying the correlation window sizes of (a) 10×10 pixels, (b) 20×20 pixels, (c) 30×30 pixels, (d) 40×40 pixels, (e) 50×50 pixels, (f) 60×60 pixels, (g) 70×70 pixels, (h) 80×80 pixels, and (i) 90×90 pixels.

Figure 4.14 shows the average SWS from all given correlation windows. According to the limitations in the curve fitting process, the measured SWS is not reliable when the correlation window is less than 30×30 pixels. The measured speed approaches a constant value at around 30×30 pixels of the correlation window. Thus,

the average SWS results were calculated from the part of data at 30×30 pixels to 90×90 pixels. Thus, the average SWS of 3 wt% ($v_{s,3\%}$) and 4 wt% ($v_{s,4\%}$) in the homogeneous case is $v_{s,3\%} = 1.3 \pm 0.1$ m/s and $v_{s,4\%} = 1.5 \pm 0.2$ m/s, respectively.

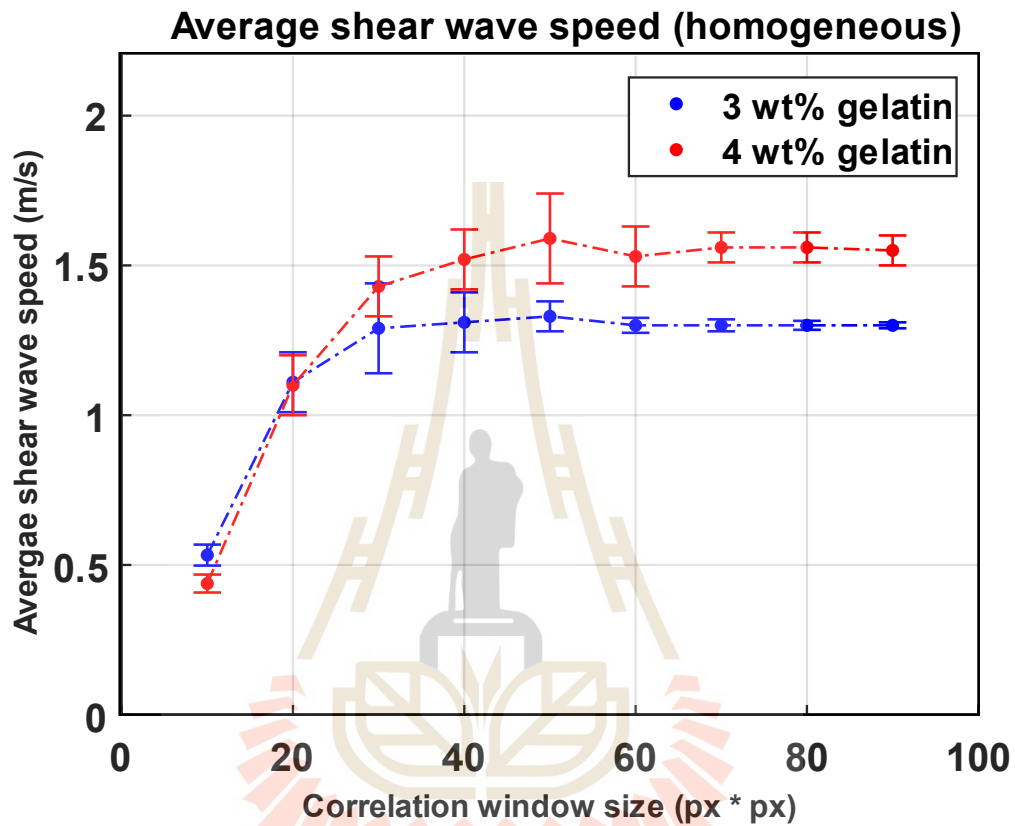


Figure 4.14 The average shear wave speed (SWS) of all given correlation windows of 3 wt% (blue) and 4 wt% gelatin phantoms.

For the verification of the elastic contrast, the 3 wt% and 4 wt% were placed side by side (L4R3) to perform on our reverberant OCE. The phantom was placed slightly oblique (figure 4.15(a)) to prevent a large gap at the interface, but the gap still existed as shown in the B-mode image in figure 4.15(b). Figure 4.15(c) shows the wavelength of shear wave propagation on 4wt% (left) is larger than the wavelength on 3 wt% (right). Figure 4.15(d) shows the SWS map of the L4R3 phantom, retrieved by using the correlation window of 40×40 pixels. Two different regions of 4 wt% and

3 wt% concentration is easily identified. The small wave reflection at the interface is observed in wave propagation VDO causes a slight curve interface.

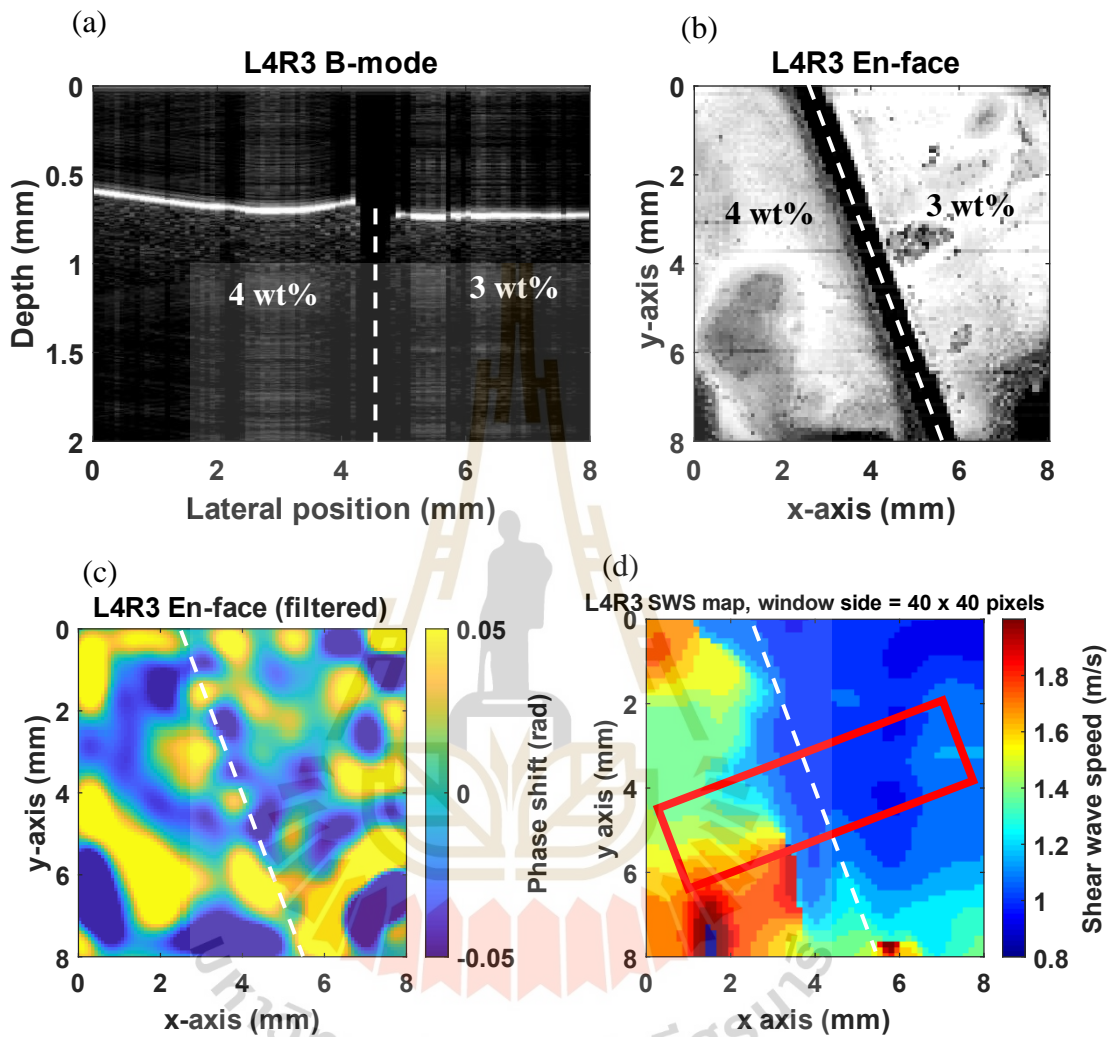


Figure 4.15 (a) B-mode and (b) *en-face* images of the left-right configuration of gelatin phantom. (c) *En-face* image of phase shift of the left-right configuration shows the different wavelengths between 4 wt% (left) and 3 wt% (right). (d) The shear wave speed (SWS) map of the L4R3 gelatin phantom shows the shear wave propagates faster on the 4 wt% gelatin phantom.

To determine the elastic contrast, the local SWS in the red frame in figure 4.15(d) was used to calculate the average shear wave profile across the interface and is shown in figure 4.16. From the shear wave profile plot, the average shear wave speed of 3 wt% and 4 wt% in the L4R3 phantom are approximately $v_{s,L4\%} = 1.5 \pm 0.3$ m/s and $v_{s,R3\%} = 1.1 \pm 0.2$ m/s, respectively, and exhibited as slant transition. The sigmoid function $sig(x)$ was used to determine the average speed profile (F. Zvietcovich et al., 2019) and shown as a blue line in figure 4.13, which can be expressed as

$$sig(x) = \frac{(v_{s,L4\%} - v_{s,R3\%})}{1 + e^{-\frac{(x_0 - x)}{\tau}}} + v_{s,R3\%}, \quad (4.1)$$

where x_0 and τ is the location of the interface and its width, respectively.

The elastic resolution of this L4R3 gelatin phantom can be obtained by determining the full width at half maximum (FWHM) of the derivative of the sigmoid function, which is also displayed as a red line in figure 4.16, and the elastic resolution is approximately 0.3 mm.

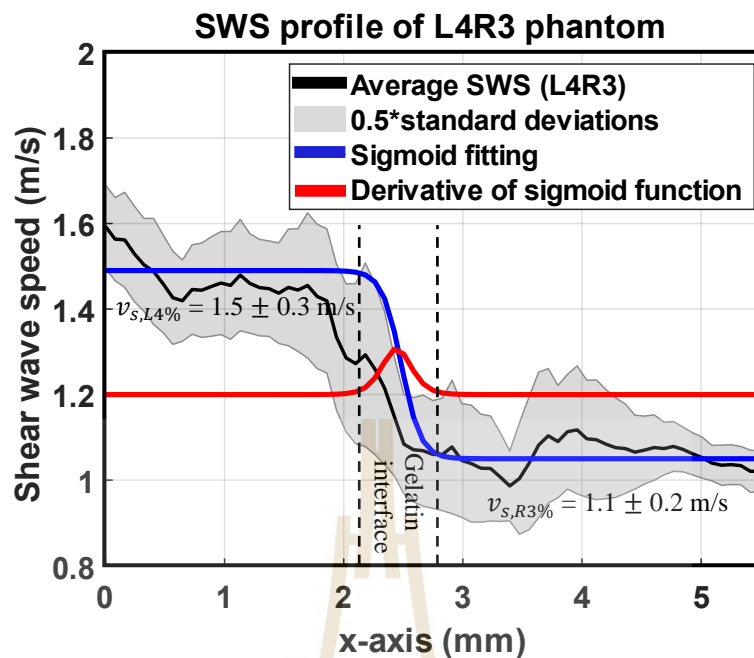


Figure 4.16 The average speed profile across the gelatin interface was computed from the SWS data in the red frame of figure 4.15(d).

The results of average SWS from both the homogeneous and left-right configurations and the results from standard measurement were shown in figure 4.17. The SWS results of homogeneous configuration are $v_{s,3\%} = 1.3 \pm 0.1$ m/s and $v_{s,4\%} = 1.5 \pm 0.2$ m/s, results of left-right configuration are $v_{s,R3\%} = 1.1 \pm 0.2$ m/s and $v_{s,L4\%} = 1.5 \pm 0.3$ m/s, and the results from the standard measurements are $v_{s,3\%}^{SM} = 1.2 \pm 0.4$ m/s and $v_{s,4\%}^{SM} = 1.7 \pm 0.5$ m/s obtained from the relationship of Young's modulus and shear wave speed followed by equation 2.27.

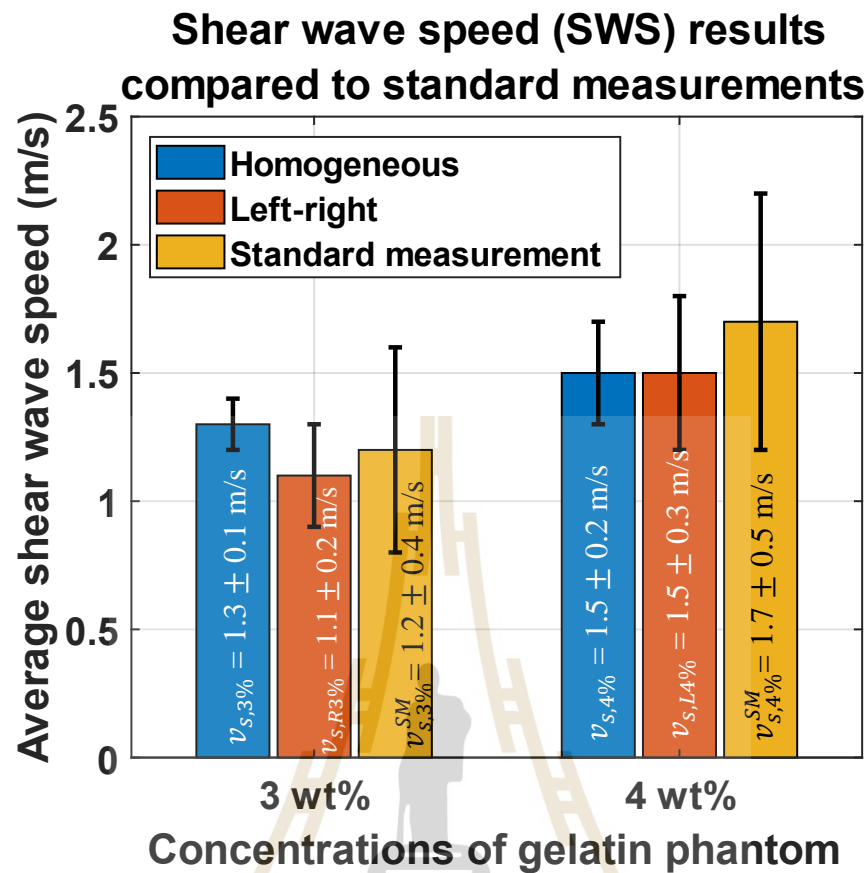


Figure 4.17 The experimental shear wave speed (SWS) results: Homogeneous (blue), left-right (orange), and the results from standard measurement (yellow) of the 3 wt% and 4 wt% gelatin phantoms.

4.4 Discussions

From all results, the study of the shear wave speed by performing our custom build reverberant optical coherence elastography with varying the size of the correlation window can determine the average shear wave speed on 3 wt% and 4 wt% gelatin phantoms with impressive results. We notice that the small correlation window provides high accuracy of the SWS results as shown in figure 4.14. However, there is a trade-off condition with the elastic resolution in the SWS map. The better choice of the

correlation window size is 40×40 pixels ($3.2 \times 3.2 \text{ mm}^2$) over the ROI of $8 \times 8 \text{ mm}^2$ or about 16% of the ROI's size, which provides the highest elastic resolution, and has the same result compared to a larger window.

However, our current setup is still under development and can be further improved to obtain better results. For example, the imaging setup has no universal setup for all phantoms yet, i.e., the position of the scanning beam, ring actuator, gelatin's surface level, and the individual force applied to the gelatin phantom was adjusted one by one to obtain a better performance. The gelatin preparation is also needed to carefully control, i.e., non-flat surface, the duration for letting the liquid mixture form gelatin structure, and the phantom orientation. The concentration diffusion of the 3 wt% and 4 wt% phantoms in the left-right configuration (figure 4.4(c)) causes the blurred SWS result at the interface as seen in figure 4.15(d). As a part of future work, we plan to study using the multiple excitations, varying the number of the excitation, together with freely controlling the initial vibration phase with the reverberant shear wave field concept. We expect better SWS map results as well as interesting ideas to enhance our instrument in nearly future.

CHAPTER V

SUMMARY

Nowadays, medical imaging has a high potential for tissue diagnostics and treatments. In this study, we focused on one kind of medical imaging called “elastography”, which is the map that contains elastic information about the tissue (Ahmad et al., 2014). The elastography technique can be determined by the advantage of the elastic property that responds differently to external distortions/vibrations between healthy and unhealthy tissues (Ophir et al., 1991). Since the late 1980s, this technique has been proven with the ultrasound imaging (UI) (Doyley and Parker, 2014), and later with magnetic resonance imaging (MRI) (Manduca et al., 2001) and atomic force microscopy imaging (AFM) (Wang and Larin, 2015). In addition, the UI, MRI provides large fields of view (FOV) and resolution in centimeters scale, and AFM provides small limited FOV and nanometers scale of resolution, whereas the study in tissue characterization e.g., ophthalmology, cardiology, dermatology requires millimeters scale of resolution. Another imaging techniques called “optical coherence elastography (OCE)” that was proposed in 1998, which based on optical coherence tomography (OCT) technique (Manapuram et al., 2012) provided suitable resolution (millimeters to micrometers scale).

To express the mechanical property of the sample, this study focused to apply the concept of “reverberant shear wave field”, which was introduced by Kelvin J. Parker and his colleagues (K. J. Parker et al., 2017) to investigate the speed of the shear wave

on the gelatin phantom by stimulating the multiple excitation sources and captured via our custom-developed OCT imaging. The concept of the reverberant shear wave field shows that the shear wave speed (SWS) results can be constructed from the local wavenumber, which is estimated from the curve fitting process of the autocorrelation function. The mathematical explanations are described in chapter II.

In this study, two gelatin phantom configurations were prepared to mimic the human tissue, which are homogeneous and left-right. Then our designed ring actuator was applied to the phantom's surface. The wave propagation on the surface will be captured by our phase-sensitive OCT (PhS-OCT), which used the near-infrared light source at 1,318 nm of center wavelength and 125 nm of spectral bandwidth. The penetration depth is approximately about 2 mm, lateral and axial resolutions are 20 μm and 10 μm , respectively, and the region of interest (ROI) is $8 \times 8 \text{ mm}^2$. PhS-OCT can provide B-mode (cross-section) and *en-face* (top view) images.

The surface (figure 4.5(a), figure 4.5(c), figure 4.6(a), and figure 4.15(a)) of the gelatin phantoms, and the gap between two gelatin concentrations, and the instabilities of the surface (figure 4.5(b), figure 4.5(d), figure 4.6(b), and figure 4.15(b)) were observed by our PhS-OCT through the bright line in B-mode images and the dark regions in *en-face* images, respectively.

In the analysis part, the relationship that the shear wave moves faster in a higher concentration of the gelatin phantom was noticed in the experiment, i.e., the wavelength of the propagated shear wave is bigger in a higher concentration phantom. Extracting the phase shift data by using Loupas's algorithm, which provides noise reduction effectively (Zvietcovich et al., 2017). Then the concept of reverberant shear wave field

was applied to determine the local SWS results, by estimating the radial average of the autocorrelation functions.

To study the effect of the correlation window on SWS results and the elastic resolution, the correlation window sizes varied from 10×10 pixels up to 90×90 pixels. The result of the experiment tells that the higher elastic resolution will be obtained by using a small correlation window but losing the SWS accuracies. In addition, the correlation windows that are larger than 40×40 pixels tend to provide the constant value as shown in figure 4.14. And the 40×40 pixels of the correlation window is a suitable choice to obtain the accurate SWS result because that provides the highest elastic resolution of our current setup.

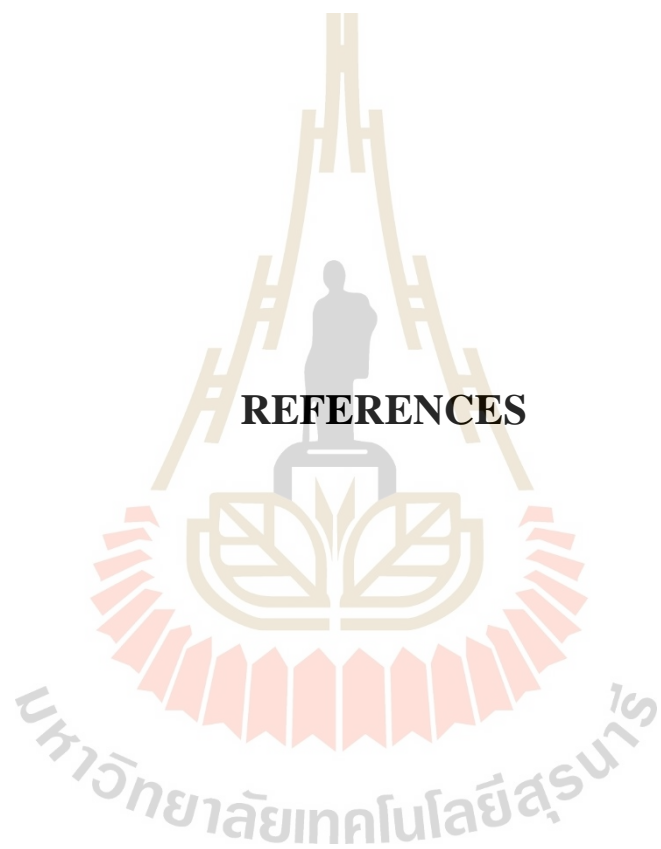
The SWS map of 3 wt% and 4 wt% phantoms were obtained with clearly observed the difference in shear wave speed propagated on the phantom. In addition, there is a merged color of the L4R3 phantom due to different concentrations of diffusion causing blurred results in the SWS map.

In the case of homogeneous phantom, the SWS results of 3 wt% and 4 wt% are $v_{s,3\%} = 1.3 \pm 0.1$ m/s and $v_{s,4\%} = 1.5 \pm 0.2$ m/s, respectively, and the results of left-right phantom are $v_{s,R3\%} = 1.1 \pm 0.2$ m/s and $v_{s,L4\%} = 1.5 \pm 0.3$ m/s. The results of standard measurements were obtained from Young's modulus measurements and then convert into wave speed by using the relationship between Young's modulus and shear wave speed. The SWS from the standard measurement of 3 wt% and 4 wt% gelatin phantoms are $v_{s,3\%}^{SM} = 1.2 \pm 0.4$ m/s and $v_{s,4\%}^{SM} = 1.7 \pm 0.5$ m/s, respectively. Thus, our Rev3D-OCE has an accuracy error of 8% and 12% for 3 wt% and 4 wt% gelatin phantoms in both configurations. Furthermore, we can clearly see the interface of the L4R3 gelatin phantom in SWS map. The sigmoid function was used to determine the

slant transition between the phantom interfaces. The elastic resolution result was obtained from the derivative of the sigmoid function, which is 0.3 mm.

The concept of the reverberant shear wave fields can apply to our imaging technique to reveal the elastic property of the sample by characterizing the speed of the shear wave that propagates on the sample. The advantage of the concept of the reverberant shear wave is that the direction of the wave propagation can be ignored because of the autocorrelation principle. However, there are still have some points to improve our system, such as the imaging setup has to proceed one by one for each phantom, the concentration diffusions of the gelatin, increasing or decreasing the number of excitation sources, and freely controlling the initial phase of excitations, which might introduce some new interesting wave patterns, and improve our setup to obtain better results.

Finally, we strongly expect that this study will be a good starting point to study or experiment with more complex samples. We look forward to further development to use in medical diagnostic applications.



REFERENCES

REFERENCES

- Abramowitz, M., and Stegun, I. A. (1965). *Handbook of Mathematical Functions: With Formulas, Graphs, and Mathematical Tables*: Dover Publications.
- Ahmad, A., Kim, J., Sobh, N. A., Shemonski, N. D., and Boppart, S. A. (2014). Magnetomotive optical coherence elastography using magnetic particles to induce mechanical waves. **Biomedical Optics Express**. 5(7): 2349-2361. doi:10.1364/BOE.5.002349.
- Aumann, S., Donner, S., Fischer, J., and Müller, F. (2019). Optical Coherence Tomography (OCT): Principle and Technical Realization. In J. F. Bille (Ed.), *High Resolution Imaging in Microscopy and Ophthalmology: New Frontiers in Biomedical Optics* (pp. 59-85). Cham: Springer International Publishing.
- The Authoritative Dictionary of IEEE Standards Terms, Seventh Edition. (2000). **IEEE Std 100-2000**: 1-1362. doi:10.1109/IEEESTD.2000.322230.
- Bailey, D. H., and Swartztrauber, P. N. (1994). A Fast Method for the Numerical Evaluation of Continuous Fourier and Laplace Transforms. **SIAM Journal on Scientific Computing**. 15(5): 1105-1110. doi:10.1137/0915067.
- Bilgen, M., and Insana, M. F. (1997). Error analysis in acoustic elastography. II. Strain estimation and SNR analysis. **The Journal of the Acoustical Society of America**. 101(2): 1147-1154. doi:10.1121/1.418019.

- Bo, E., Liu, X., and Liu, L. (2016). Signal-to-Noise Ratio Enhanced Spectral Domain Optical Coherence Tomography with Dual-balanced Detection. **Procedia Engineering**. 140: 140-143. doi:10.1016/j.proeng.2015.07.358.
- Boer, J., Cense, B., Park, B., Pierce, M., Tearney, G., and Bouma, B. (2003). Improved signal-to-noise ratio in spectral-domain compared with time-domain optical coherence tomography. **Optics Letters**. 28: 2067-2069. doi:10.1364/OL.28.002067.
- Cartigliani, C., Bonfigli, A., Brancato, S., and Rigano, L. (2014). The Age Factor in the Cosmetic Management of Biophysical Skin Parameters. **Cosmetics**. 1(2): 117-127. doi:10.3390/cosmetics1020117.
- Crecea, V., Oldenburg, A. L., Liang, X., Ralston, T. S., and Boppart, S. A. (2009). Magnetomotive nanoparticle transducers for optical rheology of viscoelastic materials. **Optics Express**. 17(25): 23114-23122. doi:10.1364/OE.17.023114.
- Davis, A. M. (2008). Development of Fourier domain optical coherence tomography for application in developmental biology. Retrieved from https://dukespace.lib.duke.edu/dspace/bitstream/handle/10161/702/D_Davis_A_njul_a_200808.pdf
- Doyley, M., and Parker, K. (2014). Elastography: General Principles and Clinical Applications. **Ultrasound clinics**. 9: 1-11. doi:10.1016/j.cult.2013.09.006.
- Fercher, A. F., Drexler, W., Hitzenberger, C. K., and Lasser, T. (2003). Optical coherence tomography - principles and applications. **Reports on Progress in Physics**. 66(2): 239-303. doi:10.1088/0034-4885/66/2/204.
- Graff, K. F. (2012). Wave Motion in Elastic Solids: Dover Publications.

- Hoyt, K., Castaneda, B., and Parker, K. J. (2008). Two-dimensional sonoelastographic shear velocity imaging. **Ultrasound Med Biol.** 34(2): 276-288. doi:10.1016/j.ultrasmedbio.2007.07.011.
- Huang, D., Swanson, E. A., Lin, C. P., Schuman, J. S., Stinson, W. G., Chang, W., Hee, M. R., Flotte, T., Gregory, K., and Puliafito, C. A. (1991). Optical coherence tomography. **Science (New York, N.Y.)**. 254(5035): 1178-1181. doi:10.1126/science.1957169.
- Itoh, A., Ueno, E., Tohno, E., Kamma, H., Takahashi, H., Shiina, T., Yamakawa, M., and Matsumura, T. (2006). Breast Disease: Clinical Application of US Elastography for Diagnosis 1. **Radiology**. 239: 341-350. doi:10.1148/radiol.2391041676.
- Jiasong, L., Shang, W., Ravi Kiran, M., Manmohan, S., Floredes, M. M., Salavat, A., Stanislav, Y. E., Michael, D. T., and Kirill, V. L. (2013). Dynamic optical coherence tomography measurements of elastic wave propagation in tissue-mimicking phantoms and mouse cornea *in vivo*. **Journal of Biomedical Optics**. 18(12): 1-7. doi:10.1117/1.JBO.18.12.121503.
- Karimi, A., and Navidbakhsh, M. (2014). Material properties in unconfined compression of gelatin hydrogel for skin tissue engineering applications. **Biomed Tech (Berl)**. 59(6): 479-486. doi:10.1515/bmt-2014-0028.
- Kennedy, B. F., Hillman, T. R., McLaughlin, R. A., Quirk, B. C., and Sampson, D. D. (2009). In vivo dynamic optical coherence elastography using a ring actuator. **Optics Express**. 17(24): 21762-21772. doi:10.1364/OE.17.021762.

- Klauser, A. S., Miyamoto, H., Bellmann-Weiler, R., Feuchtner, G. M., Wick, M. C., and Jaschke, W. R. (2014). Sonoelastography: Musculoskeletal Applications. **Radiology**. 272(3): 622-633. doi:10.1148/radiol.14121765.
- Li, C., Guan, G., Reif, R., Huang, Z., and Wang, R. K. (2012). Determining elastic properties of skin by measuring surface waves from an impulse mechanical stimulus using phase-sensitive optical coherence tomography. **Journal of the Royal Society, Interface**. 9(70): 831-841. doi:10.1098/rsif.2011.0583.
- Li, C., Huang, Z., and Wang, R. (2011). Elastic properties of soft tissue-mimicking phantoms assessed by combined use of laser ultrasonics and low coherence interferometry. **Optics Express**. 19: 10153-10163. doi:10.1364/OE.19.010153.
- Lifshitz, E. M., Kosevich, A. M., and Pitaevskii, L. P. (1986). CHAPTER III - ELASTIC WAVES. In E. M. Lifshitz, A. M. Kosevich, & L. P. Pitaevskii (Eds.), *Theory of Elasticity (Third Edition)* (pp. 87-107). Oxford: Butterworth-Heinemann.
- Loupas, T., Peterson, R. B., and Gill, R. W. (1995). Experimental evaluation of velocity and power estimation for ultrasound blood flow imaging, by means of a two-dimensional autocorrelation approach. **IEEE Transactions on Ultrasonics, Ferroelectrics, and Frequency Control**. 42(4): 689-699. doi:10.1109/58.393111.
- Manapuram, R. K., Aglyamov, S., Monediado, F., Mashiatulla, M., Li, J., Emelianov, S., and Larin, K. (2012). In vivo estimation of elastic wave parameters using phase-stabilized swept source optical coherence elastography. **Journal of Biomedical Optics**. 17: 100501-100501. doi:10.1117/1.JBO.17.10.100501.

- Manapuram, R. K., Manne, V. G. R., and Larin, K. V. (2009). Phase-sensitive swept source optical coherence tomography for imaging and quantifying of microbubbles in clear and scattering media. **Journal of Applied Physics**. 105(10): 102040. doi:10.1063/1.3116614.
- Manduca, A., Oliphant, T. E., Dresner, M. A., Mahowald, J. L., Kruse, S. A., Amromin, E., Felmlee, J. P., Greenleaf, J. F., and Ehman, R. L. (2001). Magnetic resonance elastography: Non-invasive mapping of tissue elasticity. **Medical Image Analysis**. 5(4): 237-254. doi:10.1016/S1361-8415(00)00039-6.
- McGarry, M. D. J., Van Houten, E. E. W., Perrañez, P. R., Pattison, A. J., Weaver, J. B., and Paulsen, K. D. (2011). An octahedral shear strain-based measure of SNR for 3D MR elastography. **Physics in Medicine and Biology**. 56(13): N153-N164. doi:10.1088/0031-9155/56/13/N02.
- Meemon, P., Yao, J., Chu, Y. J., Zvietcovich, F., Parker, K. J., and Rolland, J. P. (2016). Crawling wave optical coherence elastography. **Optics Letters**. 41(5): 847-850. doi:10.1364/OL.41.000847.
- Mulligan, J. A., Untracht, G. R., Chandrasekaran, S. N., Brown, C. N., and Adie, S. G. (2016). Emerging Approaches for High-Resolution Imaging of Tissue Biomechanics With Optical Coherence Elastography. **IEEE Journal of Selected Topics in Quantum Electronics**. 22(3): 246-265. doi:10.1109/JSTQE.2015.2481705.
- Muscolino, J. E. (2008). *The Muscle and Bone Palpation Manual with Trigger Points, Referral Patterns and Stretching*: Mosby/Elsevier.

- Onajite, E. (2014). Chapter 2 - Understanding Seismic Wave Propagation. In E. Onajite (Ed.), *Seismic Data Analysis Techniques in Hydrocarbon Exploration* (pp. 17-32). Oxford: Elsevier.
- Ophir, J., Céspedes, I., Ponnekanti, H., Yazdi, Y., and Li, X. (1991). Elastography: A Quantitative Method for Imaging the Elasticity of Biological Tissues. **Ultrasonic Imaging**. 13(2): 111-134. doi:10.1177/016173469101300201.
- Parker, K. J., Doyley, M. M., and Rubens, D. J. (2010). Imaging the elastic properties of tissue: the 20 year perspective. **Physics in Medicine and Biology**. 56(1): R1-R29. doi:10.1088/0031-9155/56/1/r01.
- Parker, K. J., and Maye, B. A. (1984). Partially coherent radiation from reverberant chambers. **The Journal of the Acoustical Society of America**. 76(1): 309-313. doi:10.1121/1.391063.
- Parker, K. J., Ormachea, J., Zvietcovich, F., and Castaneda, B. (2017). Reverberant shear wave fields and estimation of tissue properties. **Physics in Medicine and Biology**. 62(3): 1046-1061. doi:10.1088/1361-6560/aa5201.
- Rehman, S. E., Khang, T. H., David, S. L., and Armando, M. (2015). A Laplacian-based SNR measure: shear stiffness estimation in MR elastography. Paper presented at the Proc.SPIE.
- Rogowska, J., Patel, N. A., Fujimoto, J. G., and Brezinski, M. E. (2004). Optical coherence tomographic elastography technique for measuring deformation and strain of atherosclerotic tissues. **Heart**. 90(5): 556-562. doi:10.1136/hrt.2003.016956.

- Saavedra, A. C., Zvietcovich, F., Lavarello, R. J., and Castaneda, B. (2017). Measurement of surface acoustic waves in high-frequency ultrasound: Preliminary results. Paper presented at the 39th Annual International Conference of the IEEE Engineering in Medicine and Biology Society, EMBC 2017.
- Salencon, J. A., and Bechtel, S. R. (2002). Handbook of Continuum Mechanics: General Concepts, Thermoelasticity. **Applied Mechanics Reviews**. 55(3): B43-B44. doi:10.1115/1.1470668.
- Schmitt, J. M. (1999). Optical coherence tomography (OCT): a review. **IEEE Journal of Selected Topics in Quantum Electronics**. 5(4): 1205-1215. doi:10.1109/2944.796348.
- Song, S., Le, N. M., Huang, Z., Shen, T., and Wang, R. K. (2015). Quantitative shear-wave optical coherence elastography with a programmable phased array ultrasound as the wave source. **Optical Letters**. 40(21): 5007-5010. doi:10.1364/OL.40.005007.
- Tian, H. (2000). Noise Analysis in CMOS Image Sensors: Stanford University.
- Wang, S., and Larin, K. V. (2015). Optical coherence elastography for tissue characterization: a review. **Journal of Biophotonics**. 8(4): 279-302. doi:10.1002/jbio.201400108.
- Wells, P. N. T., and Liang, H.-D. (2011). Medical ultrasound: imaging of soft tissue strain and elasticity. **Journal of the Royal Society, Interface**. 8(64): 1521-1549. doi:10.1098/rsif.2011.0054.

- Worden, K. (2001). Rayleigh and Lamb Waves - Basic Principles. **Strain**. 37(4): 167-172. doi:10.1111/j.1475-1305.2001.tb01254.x.
- Zvietcovich, F., Ge, G. R., Mestre, H., Giannetto, M., Nedergaard, M., Rolland, J. P., and Parker, K. J. (2019). Longitudinal shear waves for elastic characterization of tissues in optical coherence elastography. **Biomedical Optics Express**. 10(7): 3699-3718. doi:10.1364/boe.10.003699.
- Zvietcovich, F., Pongchalee, P., Meemon, P., Rolland, J. P., and Parker, K. J. (2019). Reverberant 3D optical coherence elastography maps the elasticity of individual corneal layers. **Nature Communications**. 10(1): 4895. doi:10.1038/s41467-019-12803-4.
- Zvietcovich, F., Rolland, J. P., Grygotis, E., Wayson, S., Helguera, M., Dalecki, D., and Parker, K. J. (2018). Viscoelastic characterization of dispersive media by inversion of a general wave propagation model in optical coherence elastography. Paper presented at the Optical Elastography and Tissue Biomechanics V 2018.
- Zvietcovich, F., Rolland, J. P., and Parker, K. J. (2017). An approach to viscoelastic characterization of dispersive media by inversion of a general wave propagation model. **Journal of Innovative Optical Health Sciences**. 10(6). doi:10.1142/S1793545817420081.
- Zvietcovich, F., Rolland, J. P., Yao, J., Meemon, P., and Parker, K. J. (2017). Comparative study of shear wave-based elastography techniques in optical coherence tomography. **Journal of Biomedical Optics**. 22(3). doi:10.1117/1.JBO.22.3.035010.

Zvietcovich, F., Yao, J., Chu, Y. J., Meemon, P., Rolland, J. P., and Parker, K. J. (2016).

A comparative study of shear wave speed estimation techniques in optical coherence elastography applications. Paper presented at the Optical Elastography and Tissue Biomechanics III.

Zvietcovich, F., Yao, J., Rolland, J. P., and Parker, K. J. (2016). Experimental classification of surface waves in optical coherence elastography. Paper presented at the Optical Elastography and Tissue Biomechanics III.



CURRICULUM VITAE

Name Mr. Nirawit Kunanta

Date of Birth February 7, 1995

Place of Birth Nong Khai, Thailand

Education 2013-2016: Bachelor of Science in Physics, School of Physics, Institute of Science, Suranaree University of Technology, Nakhon Ratchasima, Thailand
2017 – present: Master of Science in Applied Physics, School of Physics, Institute of Science, Suranaree University of Technology, Nakhon Ratchasima, Thailand

Scholarship Development and Promotion of Science and Technology Talents Project (DPST)

Publication “Performance of Shear Wave Speed Measurements by Using Reverberant Optical Coherence Elastography”
Nirawit Kunanta, Fernando Zvietcovich, Kevin J. Parker, Jannick P. Rolland, and Panomsak Meemon, Chiang Mai journal of Science. (2022), 49(1): 81-92.